

VOL.107 NO.ST10. OCT. 1981

JOURNAL OF THE STRUCTURAL DIVISION

PROCEEDINGS OF
THE AMERICAN SOCIETY
OF CIVIL ENGINEERS



VOL.107 NO.ST10. OCT. 1981

JOURNAL OF THE STRUCTURAL DIVISION

PROCEEDINGS OF
THE AMERICAN SOCIETY
OF CIVIL ENGINEERS



Copyright© 1981 by
American Society
of Civil Engineers
All Rights Reserved
ISSN 0044-8001

John E. Bower, Editor
U.S. Steel Corporation

AMERICAN SOCIETY OF CIVIL ENGINEERS

BOARD OF DIRECTION

President

Irvan F. Mendenhall

Past President

Joseph S. Ward

President Elect

James R. Sims

Vice Presidents

Robert D. Bay
Francis J. Connell

Lyman R. Gillis
Albert A. Grant

Directors

Martin G. Abegg	Paul R. Munger
Floyd A. Bishop	William R. Neuman
L. Gary Byrd	Leonard S. Oberman
Larry J. Feeser	John D. Parkhurst
John A. Focht, Jr.	Celestino R. Pennoni
Sergio Gonzalez-Karg	Robert B. Rhode
James E. Humphrey, Jr.	S. Russell Stearns
Richard W. Karn	William H. Taylor
Leon D. Luck	Stafford E. Thornton
Arthur R. McDaniel	Robert E. Whiteside
Richard S. Woodruff	

EXECUTIVE OFFICERS

Eugene Zwayer, *Executive Director*
Julie E. Gibouleau, *Assistant to the Executive Director*
Louis L. Meier, *Washington Counsel/Assistant Secretary*
William H. Wisely, *Executive Director Emeritus*
Michael N. Salgo, *Treasurer*
Elmer B. Isaak, *Assistant Treasurer*

STAFF DIRECTORS

Donald A. Buzzell, *Managing Director for Education and Professional Affairs*
Robert A. Crist, Jr., *Managing Director for Publications and Technical Affairs*
Alexandra Bellow, *Director, Human Resources*
David Dresia, *Director, Publications Production and Marketing*
Barker D. Herr, *Director, Membership*
Richard A. Jeffers, *Controller*
Carl E. Nelson, *Director, Field Services*
Don F. Reynolds, *Director, Policy, Planning and Public Affairs*
Bruce Rickerson, *Director, Legislative Services*

Albert W. Turchick, *Director, Technical Services*

George K. Wadlin, *Director, Education Services*

R. Lawrence Whipple, *Director, Engineering Management Services*

COMMITTEE ON PUBLICATIONS

Stafford E. Thornton, *Chairman*
Martin G. Abegg
John A. Focht, Jr.
Richard W. Karn
Paul R. Munger
William R. Neuman

STRUCTURAL DIVISION

Executive Committee

John E. Bower, *Chairman*
Ronald G. Dornier, *Vice Chairman*
Peter B. Cooper
Roland L. Sharpe
Donald McDonald, *Secretary*
Frederick H. Sterbenz, *Management Group B Contact Member*
Joseph H. Appleton, *Management Group B Contact Member*

Publications Committee

John E. Bower, *Chairman, Editor and Exec. Comm. Contact Member*
Mihran S. Agbabian
Bruce E. Lyons
Marvin E. Criswell
Walter Podolny
John T. DeWolf
Emil Simiu
Douglas Foutch
John F. Stolz
Ovadia E. Lev
C. K. Wang
Le-Wu Lu
James T. P. Yao

PUBLICATIONS SERVICES DEPARTMENT

David Dresia, *Director, Publications Production and Marketing*

Technical and Professional Publications

Richard R. Torrens, *Manager*
Chuck Wahrhaftig, *Chief Copy Editor*
Corinne Bernstein, *Copy Editor*
Linda Ellington, *Copy Editor*
Walter Friedman, *Copy Editor*
Shiela Menaker, *Production Co-ordinator*
Richard C. Scheblein, *Draftsman*

Information Services

Melanie G. Edwards, *Editor*

PERMISSION TO PHOTOCOPY JOURNAL PAPERS

Permission to photocopy for personal or internal reference beyond the limits in Sections 107 and 108 of the U.S. Copyright Law is granted by the American Society of Civil Engineers for libraries and other users registered with the Copyright Clearance Center, 21 Congress Street, Salem, Mass. 01970, provided the appropriate fee is paid to the CCC for all articles bearing the CCC code. Requests for special permission or bulk copying should be addressed to the Manager of Technical and Professional Publications, American Society of Civil Engineers.

CONTENTS

Transmission Line Dynamic/Static Structural Testing <i>by Leon Kempner Jr., Richard C. Stroud, and Strether Smith</i>	1895
Shear Stresses in Circularly Curved Bars <i>by Chirasak Thasanatorn and Walter D. Pilkey</i>	1907
Wind Loads on Eaves of Low Buildings <i>by Theodore Stathopoulos</i>	1921
Sequential Geometric Optimization <i>by Ovidia E. Lev</i>	1935
Cyclic Shear Transfer and Type of Interface <i>by Alan H. Mattock</i>	1945
Ultimate Capacity of Circular Tubular Joints <i>by Joseph A. Yura, Nicholas Zettlemoyer, and Ian F. Edwards</i>	1965
Vibrations of Cable-Reinforced Inflatable Structures <i>by O. G. Vinogradov, D. J. Malcolm, and P. G. Glockner</i>	1985

The Journal of the Structural Division (ISSN 0044-8001) is published monthly by the American Society of Civil Engineers. Publications office is at 345 East 47th Street, New York, N.Y. 10017. Address all ASCE correspondence to the Editorial and General Offices at 345 East 47th Street, New York, N.Y. 10017. Allow six weeks for change of address to become effective. Subscription price to members is \$22.50. Nonmember subscriptions available; prices obtainable on request. Second-class postage paid at New York, N.Y. and at additional mailing offices. ST.

POSTMASTER: Send address changes to American Society of Civil Engineers, 345 East 47th Street, New York, NY 10017.

The Society is not responsible for any statement made or opinion expressed in its publications.

Parameter Study of Outrigger-Braced Tall Building Structures <i>by B. Stafford Smith and Irawan Salim</i>	2001
Shape Optimization: Finite Element Example <i>by William R. Spillers and Sohan Singh</i>	2015

TECHNICAL NOTES

Proc. Paper 16532

Determinate Tensegric Shells <i>by Oren Vilnay</i>	2029
--	------

DISCUSSION

Proc. Paper 16527

Vertical Vibration Analysis of Suspension Bridges,* by Ahmed M. Abdel-Ghaffar (Oct., 1980). <i>by Hassan I. A. Hegab</i>	2037
--	------

Effects of Fire on Reinforced Concrete Members,* by Bruce Ellingwood and James R. Shaver (Nov., 1980). <i>by I.D. Bennetts and I. R. Thomas</i>	2038
---	------

Space Truss Studies with Force Limiting Devices,* by Ariel Hanaor and Lewis C. Schmidt (Nov., 1980). <i>by E. A. Smith</i>	2043
--	------

Column Base Plates with Axial Loads and Moments,* by John T. DeWolf and Edward F. Sarisley (Nov., 1980). <i>by Grover H. Bays</i>	2045
---	------

Effect of Openings on Lateral Buckling of Beams,* by Alexander Coull and Maria C. Alvarez (Dec., 1980). <i>by Narayanan Subramanian</i>	2046
---	------

Wind-Induced Lock-In Excitation of Tall Structures,* by Kenny C. S. Kwok and William H. Melbourne (Jan., 1981). <i>by A. Kareem</i>	2047
---	------

*Discussion period closed for this paper. Any other discussion received during this discussion period will be published in subsequent Journals.

Load Distribution and Double Skin Wall,* by Raymond M. L. Ting (Feb., 1981). by Theodore Stathopoulos	2048
Response of RC Shear Wall under Ground Motions,* by Awadh B. Agrawal, Leslie G. Jaeger, and Aftab A. Mufti (Feb., 1981). by Mehdi Saiidi	2050
Wind Speed Distributions and Reliability Estimates, by Emil Simiu, James J. Shaver, and James J. Filliben (May, 1981). errata	2052

INFORMATION RETRIEVAL

The key words, abstract, and reference "cards" for each article in this Journal represent part of the ASCE participation in the EJC information retrieval plan. The retrieval data are placed herein so that each can be cut out, placed on a 3 × 5 card and given an accession number for the user's file. The accession number is then entered on key word cards so that the user can subsequently match key words to choose the articles he wishes. Details of this program were given in an August, 1962 article in CIVIL ENGINEERING, reprints of which are available on request to ASCE headquarters.

*Discussion period closed for this paper. Any other discussion received during this discussion period will be published in subsequent Journals.

1. The first of these is the fact that the
the first of these is the fact that the
the first of these is the fact that the

2. The second of these is the fact that the
the second of these is the fact that the
the second of these is the fact that the

3. The third of these is the fact that the
the third of these is the fact that the
the third of these is the fact that the

4. The fourth of these is the fact that the
the fourth of these is the fact that the
the fourth of these is the fact that the

5. The fifth of these is the fact that the
the fifth of these is the fact that the
the fifth of these is the fact that the

6. The sixth of these is the fact that the
the sixth of these is the fact that the
the sixth of these is the fact that the

7. The seventh of these is the fact that the
the seventh of these is the fact that the
the seventh of these is the fact that the

8. The eighth of these is the fact that the
the eighth of these is the fact that the
the eighth of these is the fact that the

9. The ninth of these is the fact that the
the ninth of these is the fact that the
the ninth of these is the fact that the

10. The tenth of these is the fact that the
the tenth of these is the fact that the
the tenth of these is the fact that the

11. The eleventh of these is the fact that the
the eleventh of these is the fact that the
the eleventh of these is the fact that the

12. The twelfth of these is the fact that the
the twelfth of these is the fact that the
the twelfth of these is the fact that the

13. The thirteenth of these is the fact that the
the thirteenth of these is the fact that the
the thirteenth of these is the fact that the

16547 TRANSMISSION LINE TESTING

KEY WORDS: Computer analysis; Dynamic characteristics; Dynamic structural analysis; Field tests; Photogrammetry; Static tests; Structural dynamics; **Testing; Towers; Transmission lines**

ABSTRACT: A series of full-scale structural static and dynamic tests were performed to characterize selected properties of a 1200-kV mechanical test line. Prior to the experiment tests, a finite-element analysis of the test tower was conducted. The analytical techniques used to determine the static and dynamic behavior of a transmission tower will provide satisfactory results. Full-scale dynamic testing using the twang excitation technique proved adequate for characterizing the dynamic properties of a transmission line tower and conductor-bundle system. The importance of a pretest computer analysis to aid in experiment design is demonstrated.

REFERENCE: Kempner, Leon, Jr. (Struct. Engr., Bonneville Power Administration, P.O. Box 3621, Portland, Oreg. 97208), Stroud, Richard C., and Smith, Strether, "Transmission Line Dynamic/Static Structural Testing," *Journal of the Structural Division, ASCE*, Vol. 107, No. ST10, **Proc. Paper 16547**, October, 1981, pp. 1895-1906

16542 SHEAR STRESSES IN CIRCULARLY CURVED BARS

KEY WORDS: Curvature; Elasticity; Finite elements; **Formulas (mathematics);** Numerical analysis; Shear stress; **Stress analysis; Stress (mechanics);** Structural dynamics; **Structural members; Warpage**

ABSTRACT: Mathematical formulations and solution techniques are presented for the stress analysis of circularly curved bars subjected to transverse forces in the plane of curvature. The formulation follows the semi-inverse method of Saint Venant, using a stress function. Numerical results are obtained with a finite element method, which accepts curved bars with complicated cross-sectional geometries.

REFERENCE: Thasanatorn, Chirasak (Research Scientist, Hydronautics, Inc., Laurel, Md. 20810), and Pilkey, Walter B., "Shear Stresses in Circularly Curved Bars," *Journal of the Structural Division, ASCE*, Vol. 107, No. ST10, **Proc. Paper 16542**, October, 1981, pp. 1907-1919

16543 WIND LOADS ON EAVES OF LOW BUILDINGS

KEY WORDS: Aerodynamics; **Buildings;** Canopies; Codes; Coefficients; Models; **Pressure; Roofs; Standards; Wind; Wind pressure**

ABSTRACT: Wind pressure loads acting on 1:12 sloped perimeter eave sections of low-rise building models have been measured in turbulent boundary layer flow, simulating wind over open country and suburban terrains. Both local and area load measurements have been carried out for two eave widths (5 ft and 10 ft in full scale) and three eave heights (16 ft, 24 ft, and 32 ft in full scale). Data show the overestimation of peak loads which may be made if the effective uplift forces on the eaves are derived from simple local pressure measurements on upper and lower eave surfaces, and full correlation of the worst cases is assumed. A simplified chart with pressure coefficients appropriate for design is also suggested.

REFERENCE: Stathopoulos, Theodore (Asst. Prof. of Engrg., Centre for Building Studies, Concordia Univ., Quebec, Canada H2G 1M8), "Wind Loads on Eaves of Low Buildings," *Journal of the Structural Division, ASCE*, Vol. 107, No. ST10, **Proc. Paper 16543**, October, 1981, pp. 1921-1934

16592 SEQUENTIAL GEOMETRIC OPTIMIZATION

KEY WORDS: Configuration; Geometry; Iteration; **Minimum weight design; Optimization;** Stress ratio; Structural analysis; **Structural design; Topology;** Trusses

ABSTRACT: A two-phase sequence of weight minimization is proposed as an approximate method for optimizing truss geometry and topology in preliminary design. In the first phase, the initial geometry is held fixed while member sizes are optimized. In the second phase, the nodal coordinates are optimized. The advantages of the heuristic method lie in reducing the number of structural analyses and in the control it offers the designer. Through the proposed technique, a reasonable initial geometry may be obtained which allows optimization of the topology of the structure.

REFERENCE: Lev, Ovadia E. (Mrg., Dept. of Advanced Design and Development, Merritt CASES, Inc., Redlands, Calif.), "Sequential Geometric Optimization," *Journal of the Structural Division*, ASCE, Vol. 107, No. ST10, **Proc. Paper 16592**, October, 1981, pp. 1935-1943

16563 Alan

KEY WORDS: Buildings (codes); **Composite structures; Concrete (precast); Concrete (reinforced);** Cracks; Interfaces; **Loads (forces); Reinforcement (structures); Shear strength (concrete); Shear tests**

ABSTRACT: Cyclically reversing and monotonic shear transfer tests are reviewed for companion initially cracked specimens of normal weight and lightweight reinforced concrete. Both composite and monolithic specimens were tested. The interfaces of all composite specimens were roughened as required by sec. 11.7.9 of the ACI Building Code, ACI 318-77. In some cases the bond at the interface was deliberately broken. In the case of monolithic specimens and composite specimens in which good bond is obtained at a roughened interface, the strength under cyclically reversing shear is about 80 percent of the shear transfer strength under monotonic loading.

REFERENCE: Mattock, H. (Prof. of Civ. Engrg., Univ. of Washington, Seattle, Wash.), "Cyclic Shear Transfer and Type of Interface," *Journal of the Structural Division*, ASCE, Vol. 107, No. ST10, **Proc. Paper 16563**, October, 1981, pp. 1945-1964

16600 CAPACITY OF CIRCULAR TUBULAR JOINTS

KEY WORDS: Connections (joints); **Equations; Formulas (mathematics); Offshore structures; Specifications; Tube joints; Ultimate strength; Ultimate strength design; Welding**

ABSTRACT: A total of 137 ultimate strength tests on simple T, Y, DT, and K tubular joints is used as a basis for development of new ultimate capacity formulas. The data are taken from a variety of sources, and only relatively large geometries are considered. Axial tension, axial compression, in-plane bending, and out-of-plane bending loads are represented. The failure condition is taken as the minimum of either maximum load, first crack load, or load at an excessive deformation limit. Several formulas are recommended to predict the capacity of the different joint and load types. The accuracy of these formulas is then studied in a statistical manner. Predictions of past and present API RP 2A formulas are compared to the same data base. The new relatively simple equations are more consistent in their level of prediction and result in less scatter.

REFERENCE: Yura, Joseph A. (Prof. of Civ. Engrg., The Univ. of Texas at Austin, Austin, Tex.), Zettlemoyer, Nicholas, and Edwards, Ian F., "Ultimate Capacity of Circular Tubular Joints," *Journal of the Structural Division*, ASCE, Vol. 107, No. ST10, **Proc. Paper 16600**, October, 1981, pp. 1965-1984

16594 CABLE REINFORCED INFLATABLE STRUCTURES

KEY WORDS: Cables; Computation; Deflection; Dynamic response; Finite elements; Inflatable structures; Loads (forces); Models; Snow; Structural dynamics; Vibration; Wind loads

ABSTRACT: The influence of internal pressure and static loads on the dynamic characteristics of cable-reinforced inflatable caps is studied numerically. The structure is modelled as a three-dimensional cable-reinforced network with the action of the membrane neglected except for transmitting pressure load to the cables. For relatively small static loads, including snow and dead weight, the natural frequencies are approximately proportional to the square root of the internal pressure. The dynamic response of the structure under the action of static wind load differs considerably from that without such loading. The static wind-type load causes the natural frequencies to vary, particularly to decrease the fundamental frequency.

REFERENCE: Vinogradov, O. G. (Asst. Prof., Dept. of Mech. Engrg., Univ. of Calgary, Calgary, Alberta, Canada), Malcolm, D. J., and Glockner, P. G., "Vibrations of Cable Reinforced Inflatable Structures," *Journal of the Structural Division, ASCE*, Vol. 107, No. ST10, **Proc. Paper 16594**, October, 1981, pp. 1985-1999

16566 OUTRIGGER-BRACED TALL BUILDINGS

KEY WORDS: Buildings; Cores; Deflection; Drift; Flexibility; Outriggers; Skyscrapers; Structural analysis; Structural design; Tall buildings; Wind loads

ABSTRACT: The behavior of outrigger-braced tall building structures is studied taking into account the flexibility of the outriggers. Expressions are developed for the core moment distribution, the top drift and the optimum location of the outriggers for minimum top drift. A characteristic non-dimensional parameter is developed that takes into account the core-to-column and core-to-outrigger flexural rigidity ratios. Graphs are plotted as functions of the characteristic parameter which allow the determination of the optimum outrigger levels for minimum drift and the corresponding core base moment for structures with up to four outriggers. The study is based on the assumption of a uniform structure and uniform horizontal distributed loading.

REFERENCE: Smith, B. Stafford (Prof., Dept. of Civ. Engrg. and Applied Mechanics, McGill Univ., Montreal, Canada), and Salim, Irawan, "Parameter Study of Outrigger-Braced Tall Building Structures," *Journal of the Structural Division, ASCE*, Vol. 107, No. ST10, **Proc. Paper 16566**, October, 1981, pp. 2001-2014

16598 SHAPE OPTIMIZATION: FINITE ELEMENT EXAMPLE

KEY WORDS: Finite elements; Optimization; Plasticity; Shape; Stress; Stress (mechanics); Structural analysis; Structural design

ABSTRACT: The study of shape optimization for skeletal structures is extended to a simple case of the finite element method using plane stress, constant strain triangular elements. Following earlier work, the method developed neglects the constitutive equations and is formulated using only node equilibrium and a "stress-type" objective function from plasticity theory. A form of constitutive equation subsequently appears through the Kuhn-Tucker conditions. As a result, the optimization algorithm used takes on the appearance of an analysis-redesign procedure. Two plane stress, beam-type examples are included.

REFERENCE: Spillers, William R. (Prof., Dept. of Civ. Engrg., Rensselaer Polytechnic Inst., Troy, N.Y.), "Shape Optimization: Finite Element Example," *Journal of the Structural Division, ASCE*, Vol. 107, No. ST10, **Proc. Paper 16598**, October, 1981, pp. 2015-2025

U.S. CUSTOMARY-SI CONVERSION FACTORS

In accordance with the October, 1970 action of the ASCE Board of Direction, which stated that all publications of the Society should list all measurements in both U.S. Customary and SI (International System) units, the following list contains conversion factors to enable readers to compute the SI unit values of measurements. A complete guide to the SI system and its use has been published by the American Society for Testing and Materials. Copies of this publication (ASTM E-380) can be purchased from ASCE at a price of \$3.00 each; orders must be prepaid.

All authors of *Journal* papers are being asked to prepare their papers in this dual-unit format. To provide preliminary assistance to authors, the following list of conversion factors and guides are recommended by the ASCE Committee on Metrication.

To convert	To	Multiply by
inches (in.)	millimeters (mm)	25.4
feet (ft)	meters (m)	0.305
yards (yd)	meters (m)	0.914
miles (miles)	kilometers (km)	1.61
square inches (sq in.)	square millimeters (mm ²)	645
square feet (sq ft)	square meters (m ²)	0.093
square yards (sq yd)	square meters (m ²)	0.836
square miles (sq miles)	square kilometers (km ²)	2.59
acres (acre)	hectares (ha)	0.405
cubic inches (cu in.)	cubic millimeters (mm ³)	16,400
cubic feet (cu ft)	cubic meters (m ³)	0.028
cubic yards (cu yd)	cubic meters (m ³)	0.765
pounds (lb) mass	kilograms (kg)	0.453
tons (ton) mass	kilograms (kg)	907
pound force (lbf)	newtons (N)	4.45
kilogram force (kgf)	newtons (N)	9.81
pounds per square foot (psf)	pascals (Pa)	47.9
pounds per square inch (psi)	kilopascals (kPa)	6.89
U.S. gallons (gal)	liters (L)	3.79
acre-foot (acre-ft)	cubic meters (m ³)	1,233

TRANSMISSION LINE DYNAMIC/STATIC STRUCTURAL TESTING

By Leon Kempner Jr.,¹ A. M. ASCE, Richard C. Stroud,²
and Strether Smith³

INTRODUCTION

During 1978, full-scale structural-dynamic and static tests were performed on the Bonneville Power Administration (BPA) 1,200-kV mechanical-test line. The objectives of the test program were to: (1) Characterize the dynamic and static properties of the 1,200-kV eight-conductor bundle and one of the suspension towers; (2) improve/verify dynamic finite element techniques used for transmission tower modeling; and (3) investigate and develop experimental testing and analytical methods for applying structural-dynamic technology to transmission-line systems. This paper presents the most significant results of the test program (2,3,4).

TEST SITE

In preparation for planned 1,200-kV transmission lines, the Bonneville Power Administration has constructed a mechanical-test line at Moro, Oregon. The test facility, shown in Fig. 1, consists of a 1.1-mile (1.8-km) test line with six towers. It is intended to provide information on the mechanical response of various ultra-high-voltage (UHV) insulator/conductor designs to artificial and natural excitation.

The transmission structures of the test line are modified double-circuit, 500-kV, self-supporting, lattice-steel towers, shown in Fig. 2. The tower foundations are rock footings that consist of stub angles grouted in bedrock which produce rigid boundary conditions. Special equipment such as work platforms, climbing ladders, and a cable elevator is installed on these towers.

During this test series, the test line was strung with single-, twin-, and eight-conductor bundle configurations of 1.6-in. (41.0-mm) diam aluminum-conductor-steel-reinforced (ACSR) conductor. Also, two 0.75-in. (19.1-mm) diam

¹Struct. Engr., Bonneville Power Administration, P.O. Box 3621, Portland, Oreg. 97208.

²Pres. Synergistic Tech. Inc., 20065 Stevens Creek Blvd., Cupertino, Calif. 95014.

³Vice Pres., Synergistic Tech. Inc., 20065 Stevens Creek Blvd., Cupertino, Calif. 95014.

Note.—Discussion open until March 1, 1982. To extend the closing date one month, a written request must be filed with the Manager of Technical and Professional Publications, ASCE. Manuscript was submitted for review for possible publication on March 12, 1980. This paper is part of the Journal of the Structural Division, Proceedings of the American Society of Civil Engineers, ©ASCE, Vol. 107, No. ST10, October, 1981. ISSN 0044-8001/81/0010-1895/\$01.00.

overhead ground wires provided lightning protection and two 0.5-in. (12.7-mm) diam steel messenger cables supported instrumentation lead wires in the spans.

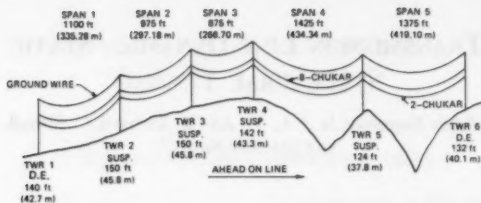


FIG. 1.—Mechanical Test Line Profile

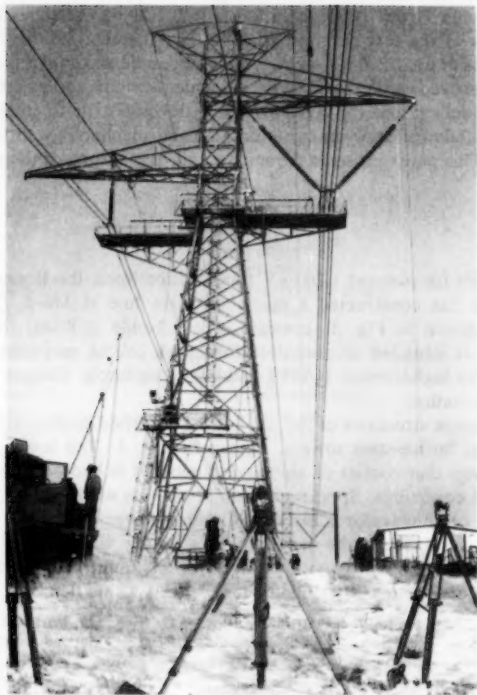


FIG. 2.—Tower Number 4

The eight-conductor bundle configuration, shown in Fig. 3 has a bundle diameter of 3.5 ft (1.07 m) with a 16 in. (406 mm) spacing between each conductor. The bundle is suspended from the tower with V-string insulator assemblies.

Spacer-dampers are installed on the bundle at staggered spacing. Span Number 4 is instrumented with accelerometers mounted on the conductors and spacer dampers.

The on-site data-acquisition system incorporates a Digital Equipment Corporation (DEC) PDP-11/35 minicomputer equipped with a 256-channel multiplexer-A/D converter.

TOWER DYNAMIC TESTS

The purpose of these tests was to characterize the dynamic properties of Tower Number 4. The experimentally determined dynamic mode shapes and frequencies were compared to the theoretical values obtained using the Structural Performance Analysis and Redesign (SPAR) finite-element computer program (Engrg. Information System, Inc., 5120 Campbell Ave., Suite 240, San Jose, Calif. 95130). The tower structural-damping coefficients were obtained from the experimental results.



FIG. 3.—Eight-Conductor Bundle

The physical nature of the transmission-line system restricted the dynamic excitation alternatives for testing. The classical excitation procedures were considered, i.e., sine dwell, sine sweep, fast sine sweep (chirp), random, impulse, release from initial displacement (twang), and ambient. The twang-excitation method was selected because of the capability of applying large loads at several locations high on the tower. The twang test is performed by loading the structure to a desired level and then suddenly releasing the load. This process approximates a step function excitation, which has a broadband frequency spectrum.

In theory, all dynamic modes should be stimulated by a single-point excitation. However, the existence of modal points and other practical considerations such as structural nonlinearity, data-acquisition resolution, and data-analysis dynamic-range restrictions require that tests be performed with loads at several points and in several directions. The analysis of each dynamic mode can be made from a test that produces the most useful response of that mode. Four twang tests were performed on the tower.

TABLE 1.—Tower Natural Frequencies, in Hertz

Mode type (1)	Frame (2)	Modified frame (3)	Truss (4)
Torsional/ longitudinal	2.24	2.27	— ^a
Transverse	2.37	2.38	2.37
Torsional/ longitudinal	2.64	2.55	2.97
Transverse	5.38	5.48	5.58
Longitudinal	7.83	8.03	8.36

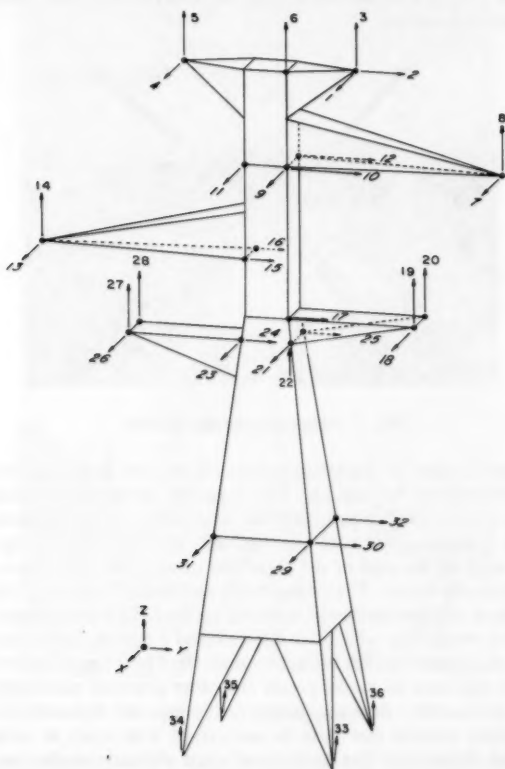
^aMode not detected.

FIG. 4.—Tower No. 4 Instrumentation

Two of the tests were performed by applying a load normal to and parallel with the direction of the test line. These excitations were primarily intended to excite the transverse and longitudinal tower dynamic modes, respectively. The remaining experiments were performed by applying a load to the tip of the upper crossarm in the vertical and longitudinal direction. These were intended to excite the transverse and torsional dynamic modes. A 10 kip (44.5 kN) load was applied for these tests. This load produced static stresses well within the elastic range of the tower members.

A pretest analysis of the tower was performed to select instrumentation and excitation locations and to give predictions of load and response levels. Three finite-element models of Tower Number 4 were developed using the SPAR program.

The structural models developed were a frame, modified frame, and space truss. The modified frame included the details of the work-platform grillage and the tower-leg bracing. There are approx 502 members and 177 node points in each of these models. The four base nodes of the tower were assumed fixed for all models.

An eigensolution was performed to estimate the resonant frequencies and associated mode shapes. The natural frequencies of the first five tower modes are shown in Table 1. In general, the modified frame and truss natural frequencies

TABLE 2.—Tower Dynamic Properties

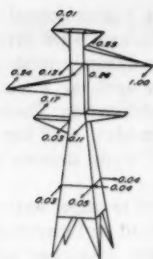
Mode type (1)	Theoretical frequency, in Hertz (2)	Experimental frequency, in Hertz (3)	Structural damping coefficient (4)
1st Transverse	2.37	2.09	0.016
1st Longitudinal	2.24	2.05	0.035
2nd Longitudinal	2.64	2.37	0.020

were higher than the frame results. The fundamental mode found with the frame analysis was not detected with the space truss model.

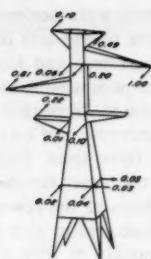
The eigensolution used the diagonal lumped mass matrix to obtain the results in Table 1. In addition, the consistent mass matrix was used to obtain the natural frequencies of the truss model. These frequencies were approx 3% higher than those shown in Table 1.

Thirty-six accelerometer positions were selected (see Fig. 4). An orthogonality check was performed on the analytically derived modes. These modes were truncated to contain only the degree-of-freedom at the instrumentation positions. The mass matrix used in the orthogonality check was determined by a Guyan (1) reduction of the full SPAR-generated mass matrix. This analysis was used to verify the adequacy of the instrument distribution. The orthogonality matrix is approximately the unit matrix, i.e., ones along the diagonal and small off-diagonal terms, which demonstrates the instrument distribution to be satisfactory for characterization of the analytical modes.

The final step in the pretest analysis was to compute the dynamic response of the tower to each of the planned loads. This analysis was performed using the Guyan-reduced mass and stiffness matrices.

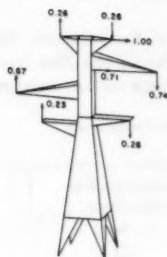


ANALYTICAL
FREQUENCY 2.24 Hz

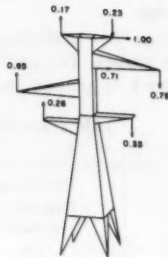


MEASURED
FREQUENCY 2.048 Hz

FIRST LONGITUDINAL MODE
ORTHOGONALITY VALUE 0.9474

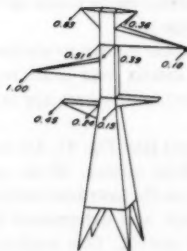


ANALYTICAL
FREQUENCY 2.37 Hz

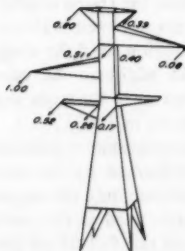


MEASURED
FREQUENCY 2.088 Hz

FIRST TRANSVERSE MODE
ORTHOGONALITY VALUE 0.9079



ANALYTICAL
FREQUENCY 2.639 Hz



MEASURED
FREQUENCY 2.373 Hz

SECOND LONGITUDINAL MODE
ORTHOGONALITY VALUE 0.9666

FIG. 5.—(a) First Longitudinal Tower Mode; (b) First Transverse Tower Mode; (c) Second Longitudinal Tower Mode

Experimental modal analysis was performed by calculating transfer functions and using least-squares techniques to determine a set of linear, superimposed modes which best fit the data. The Vibration Analysis and Measurement Processor (STI-VAMP, Synergistic Tech. Inc., Cupertino, Calif.) was used for all data reduction and display. The result of the analysis was a set of mode shapes, modal frequencies, and damping estimates.

Table 2 summarizes the modal characteristics of the first three tower modes determined by the theoretical and experimental analysis. The resonant frequencies determined by the theoretical analysis are approx 10% higher than the experimental determinations. Refinement of the tower model to include the effect of the conductor and insulator assemblies would lower the theoretical values. Other factors, which would cause discrepancies in these values, include flexibility and slippage of the tower joints which can not be accurately modeled. Curvefit analysis of the experimental transfer functions produced structural-damping coefficients ranging from 0.015–0.040.

Figs. 5(a), 5(b), and 5(c) show a comparison of the normalized analytical and experimental mode shapes. These results are for the first three tower modes.

TABLE 3.—Tower Dynamic Response, in Gravitational Acceleration

Test type (1)	Degree of freedom (Fig. 4) (2)	Theoretical acceleration (3)	Measured acceleration (4)
Torsion	7	4.1	3.9
Torsion	8	3.1	2.9
Longitudinal	4	1.8	1.9
Transverse	8	0.8	0.8
Transverse	2	0.7	0.4
Vertical	8	4.5	3.0

This figure represents measured degrees-of-freedom with significant response.

Correlation of all the experimental and theoretical modes was determined by an orthogonality check. Also, measured mode shapes were plotted using the SPAR program. These plots were generated by expansion of the 32 measured motions to all of the modeled degrees-of-freedom by using 32 constrained static-displacement functions.

Table 3 is a comparison of some of the measured and theoretically predicted acceleration responses for the tower.

TOWER STATIC TESTS

Static load/deflection tests were performed prior to each tower dynamic test. The load was incremented to 10 kips (44.5 kN) in two cycles with a total of 18 load steps. Deflections were recorded using Wild T-16 theodolites and two close-range photogrammetric MK70 Hasselblad cameras. Fourteen theodolite and 43 photogrammetric targets were used.

The objective of the photogrammetric study was to evaluate its use for measuring tower deflections. This technique allows the determination of three-dimensional displacements for each photogrammetric target. With the two camera systems used, the measurement resolution (under ideal conditions) is ± 0.2 in. (± 5 mm). Good results were obtained with this method when displacements were on the order of 1.0 in. (25.4 mm) and greater. The reduction of this data is considered in Refs. 5 and 6.

Fig. 6 shows typical load/deflection plots obtained from the theodolite and photogrammetric data. The stiffness values for the theodolite data, 4.6 kip/in. (797 kN/mm), and the photogrammetric data, 4.9 kip/in. (860 kN/mm), show good agreement.

Deflections below the upper work platform (Fig. 2) were too small to detect with the measurement systems used. The photogrammetric data showed more

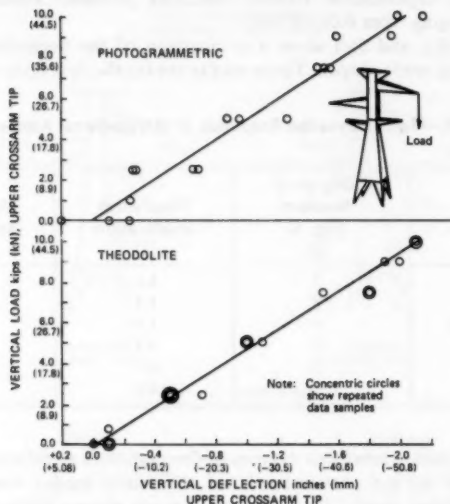


FIG. 6.—Tower Crossarm Load/Deflection Curve

scatter than the theodolite results but did verify the effectiveness of the approach. It is expected that at least a twofold improvement in accuracy can be obtained with improved techniques.

Analytical deflection results were obtained from the three finite-element models. Table 4 tabulates the deflections at the load point for a maximum load of 10 kips (44.5 kN). The model results show good agreement with the field measured values.

CONDUCTOR DYNAMIC TESTS

The eight-conductor bundle dynamic tests consisted of a 4-kip (17.8-kN) vertical load and a 1-kip (4.5-kN) torsional load twang test at Spacer Numbers 2 and

TABLE 4.—Deflection in inches (millimeters), at 10-Kip Load

Test type/ direction (1)	Experimental measurement (2)	Frame (3)	Modified frame (4)	Truss (5)
Torsion/ x direction	5.2 (132)	4.5 (114)	4.3 (109)	4.3 (109)
Transverse/ y direction	1.3 (33)	1.2 (30.5)	1.2 (30.5)	1.2 (30.5)
Longitudinal/ x direction	1.3 (33)	1.2 (30.5)	1.2 (30.5)	1.3 (33)
Vertical/ z direction	2.2 (55.9)	2.1 (53.3)	2.1 (53.3)	2.1 (53.3)

Note: 1 in. = 25.4 mm.

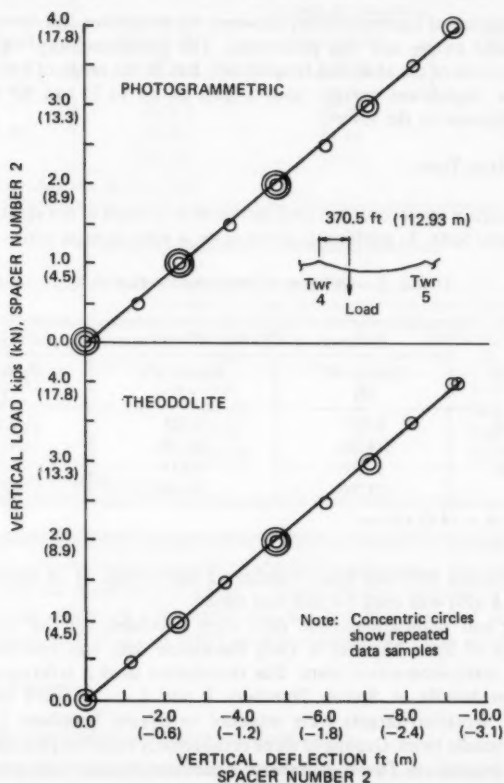


FIG. 7.—Spacer Number 2 Load/Deflection Curve

3 of Span Number 4. Spacer Number 2 and 3 are located at 26% and 43% of full span respectively, measured from Tower Number 4.

The primary instrumentation used to characterize the bulk dynamics (low-frequency response) of the eight-conductor bundle was a set of accelerometers mounted on Spacer Numbers 2 and 3. These transducers were installed in a radial pattern with an angle of 120° between each unit, and with the bottom accelerometer oriented in a horizontal position. Vertical, horizontal, and rotational motions can be separated by using this transducer configuration.

Response time histories and spectra were analyzed for a period of 60 s, starting 60 s after the initial excitation. During this period, the traveling waves, which dominated early conductor motion, have been damped out and only "modal" behavior remains. Curvefit analysis showed that the first two modes were at 0.16 Hz and 0.28 Hz and the structural-damping coefficient varied from about 0.08, for the low-frequency modes, to 0.004 for modes above 2 Hz.

An investigation of transmissibility between the conductor and tower response for a conductor twang test was performed. The transmissibility was found to be small over most of the analyzed frequencies, but, in the range of low-frequency tower modes, significant energy (with a gain of up to 1) can be transferred from the conductor to the tower.

CONDUCTOR STATIC TESTS

Displacements were recorded at load increments for each of the eight-conductor bundle dynamic tests. In addition to these tests, a span-to-span static interaction

TABLE 5.—Stiffness (Conductor Vertical Pull)

Load point (1)	Stiffness, in kips per foot (kilonewtons per meter)		
	Spacer #1 (2)	Spacer #2 (3)	Spacer #3 (4)
Spacer #2	0.983 (14.33)	0.428 (6.24)	0.699 (10.19)
Spacer #3	1.697 (24.74)	0.717 (10.45)	0.383 (5.584)

Note: 1 kip/ft = 14.58 kN/m.

test was performed between Span Numbers 2 and 3 (Fig. 1). A maximum load of 4 kips (17.8 kN) was used for this test series.

Theodolite and photogrammetric data were recorded for the vertical and torsional tests of Span Number 4. Only theodolite data was recorded for the span-to-span static-interaction tests. The theodolites used a reference point on the conductor bundle at Spacer Numbers 2 and 3 to measure the vertical displacement. Rotation targets were attached to Spacer Numbers 1, 2, and 3 to record the bundle twist. Groups of three orthogonally oriented photogrammetric targets were located on Tower Number 4 conductor-bundle yoke plate and on Spacer Numbers 1, 2, and 3. Three-dimensional translations plus rotational displacements were determined from the motion of these targets.

Fig. 7 shows typical values of the vertical deflection measured at Spacer Number 2 with the applied vertical load at this spacer. Good agreement was obtained between the theodolite and photogrammetric data.

Table 5 is a tabulation of the calculated stiffness values, i.e., slope of the load/deflection curve, for the vertical-load tests. This data shows an apparent in-span reciprocity between Spacer Numbers 2 and 3.

Table 6 tabulates the stiffness values, i.e., slope of the torque/angular deflection curve, obtained from the conductor-bundle torsion tests. The load/deflection plots of the torsion tests showed similar linear behavior to that shown in Fig. 7 for the conductor-bundle vertical tests.

TABLE 6.—Stiffness (Conductor Torsional Pull)

Load point (1)	Stiffness, in foot-pounds per degree (Joules per degree)		
	Spacer #1 (2)	Spacer #2 (3)	Spacer #3 (4)
Spacer #2	67.51 (91.81)	28.01 (38.09)	57.56 (78.28)
Spacer #3	164.43 (223.62)	56.66 (77.06)	23.41 (31.84)

Note: 1 ft-lb/deg = 1.36 m-N/deg.

TABLE 7.—Span-to-Span Interaction Test

Load point (1)	Stiffness, in kips per foot (kilonewtons per meter)	
	Center span #2 (2)	Center span #3 (3)
Spacer #2	0.41 (5.98)	5.10 (74.4)
Spacer #3	4.62 (67.36)	0.43 (6.27)

Note: 1 kip/ft = 14.58 kN/m.

The span-to-span static-interaction test was performed to determine the static behavior between two adjacent eight-conductor bundle spans. The results obtained from this test are presented in Table 7. These results represent a vertical load applied at the center of each span and the resulting vertical displacements. A span-to-span reciprocity of $\pm 10\%$ is demonstrated by these results.

CONCLUDING REMARKS

This study resulted in the following conclusions:

1. The analytical techniques used to determine the static and dynamic behavior of the transmission line tower provide sufficiently accurate results. The three tower models showed agreement among themselves for both the static and dynamic

analyses. However, the space truss model did not detect the fundamental mode that was found by both frame models and the experimental analysis. The experimentally and analytically generated modal frequency and mode-shape determinations agreed within 10%. The experimental determination of damping showed values from 0.015–0.040 for the structural damping coefficient.

2. This test series demonstrated the twang excitation technique to be adequate for characterizing the dynamic properties of the tower and conductor-bundle (for low-frequency response) system despite data analysis difficulties that arise from short-duration response. A potential improvement may be to provide a continuous excitation function that can be controlled in level and duration. A hydraulic shaker, driven by a sinusoidal or chirp (fast sine sweep), appears to be a potential solution. This excitation method would also allow for the study of the system response to a wide range of simulated "real" excitation.

APPENDIX I.—REFERENCES

1. Guyan, R. J., "Reduction of Stiffness and Mass Matrices," *Journal of the American Institute of Aeronautics and Astronautics*, Vol. 3, No. 2, Feb., 1968, p. 380.
2. Kempner, L., "UHV Moro Mechanical Test Line, Structural Static Tests, November 27–December 2, 1978," *Report No. ME-80-3*, Moro 1200 kV Project, Bonneville Power Administration, Portland, Oreg., May, 1980.
3. Kempner, L., Smith, S., and Stroud, R. C., "UHV Moro Mechanical Test Line, Structural Dynamic Tests, November 27–December 2, 1978," *Report No. ME-80-4*, Moro 1,200 kV Project, Bonneville Power Administration, Portland, Oreg., Apr., 1980.
4. Kempner, L., Smith, S., and Stroud, R. C., "Structural-Dynamic Characterization of an Experimental 1200 Kilovolt Electrical Transmission Line System," *The Shock and Vibration Bulletin*, No. 50, Part 3, Sept., 1980, pp. 113–123.
5. Pries, R. A., "Photogrammetric Data Analysis Moro Staged Tests, November 27–December 2, 1978," *Report No. ME-80-2*, Moro 1200 kV Project, Bonneville Power Administration, Portland, Oreg., Mar., 1980.
6. Veress, S. A., "Photogrammetric Monitoring Moro 1200 kV STR/MECH. Test Line, November 27–December 2, 1978," Final Technical Report for Bonneville Power Administration Contract No. DE-AC79-79BP11090, University of Washington, Seattle, Wash., 1979.

SHEAR STRESSES IN CIRCULARLY CURVED BARS

By Chirasak Thasanatorn¹ and Walter D. Pilkey,² M. ASCE

INTRODUCTION

The exact stress determination of a circularly curved bar subjected to pure bending and shear forces in the plane of curvature requires the solution of a boundary-value problem of three-dimensional elasticity. This presents formidable complications because of the difficulty of satisfying the boundary conditions. Few elasticity problems for curved bars have been solved. Analytical solutions of a curved bar with circular cross sections were developed by Golovin, as presented in Timoshenko (2). Also given in Ref. 2 are plane elasticity solutions for curved bars of small width. A so-called strength-of-material theory of curved bars was developed by Winkler using assumptions analogous to the Bernoulli-Euler hypothesis of straight beam theory. In this case, the equilibrium conditions are satisfied in an average sense.

This paper presents a method for the stress analysis of a circularly curved bar subjected to a transverse end force in the plane of the bar curvature. This formulation follows the semi-inverse method of Saint Venant, using a stress function. The assumption that stresses on any cross section depend upon forces at that particular cross section permits the three-dimensional elasticity problem to be reduced to determining the stresses on the cross section of the curved bar. The stress solutions obtained from this structural model may be extended to more general cases of loading by appealing to Saint Venant's principle, provided that the cross section of interest is sufficiently far from any points of rapid variation in the internal forces. Finally, a finite element method, which is suitable for a curved bar with complicated cross-sectional geometry, is used to determine the stresses on the cross section.

Torsional stresses for circularly curved bars are treated in Ref. 1.

ELASTICITY FORMULATION

Consider a planar curved bar of initial curvature R , with one end fixed and the other end free, as shown in Fig. 1. The bar is subjected to a transverse

¹Research Scientist, Hydronautics, Inc., Laurel, Md. 20810.

²Prof. of Applied Mechanics, Univ. of Virginia, Charlottesville, Va. 22901.

Note.—Discussion open until March 1, 1982. To extend the closing date one month, a written request must be filed with the Manager of Technical and Professional Publications, ASCE. Manuscript was submitted for review for possible publication on March 4, 1980. This paper is part of the Journal of the Structural Division, Proceedings of the American Society of Civil Engineers, ©ASCE, Vol. 107, No. ST10, October, 1981. ISSN 0044-8001/81/0010-1907/\$01.00.

radial force passing through the shear center at the free end. Assume: (1) The material is linearly elastic, continuous, homogeneous, and isotropic; (2) the curved bar is planar, lying in the x - z plane with the longitudinal axis coinciding with the geometric centroid of the cross section; (3) the curved bar can have any arbitrary cross-sectional configuration but must be prismatic; (4) the body forces are small compared to the magnitudes of the stresses and can be neglected; (5) the stresses at any cross section are assumed to depend upon only the internal forces at that cross section; and finally (6) the normal stress distribution is assumed to follow a hyperbolic law in the radial direction. The curved bar is modeled with fixed-free ends to simplify the mathematical formulation. For this case the variations of internal forces along the curved bar axis are either constant or are a function of sine or cosine functions.

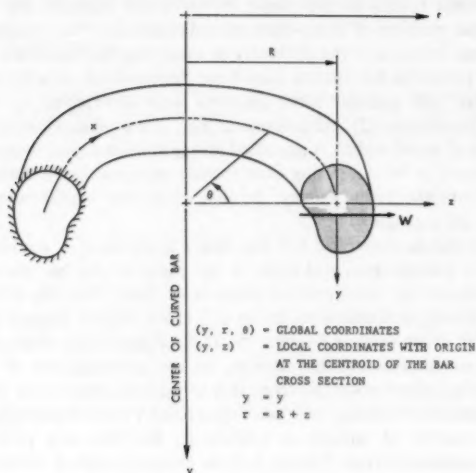


FIG. 1.—Structural Model for Direct Shear Stress Analysis

From the overall equilibrium conditions of the bar of Fig. 1, the internal forces at any cross section along the bar axis are

$$P = W \sin \theta; \quad M_v = -WR \sin \theta; \quad V_x = W \cos \theta$$

$$M_x = M_y = 0; \quad V_z = 0 \dots \dots \dots (1)$$

The twisting moment, M_x , vanishes due to the assumption that the force W passes through the shear center of the cross section.

From the aforementioned assumption 5 and Eq. 1, the three-dimensional elasticity problem may be reduced to a two-dimensional one by expressing the stresses in the form

$$\begin{aligned} \sigma_x &= \bar{\sigma}_x(y, z) \sin \theta; & \sigma_y &= \bar{\sigma}_y(y, z) \sin \theta; & \sigma_z &= \bar{\sigma}_z(y, z) \sin \theta \\ \tau_{yx} &= \bar{\tau}_{yx}(y, z) \sin \theta; & \tau_{xy} &= \bar{\tau}_{xy}(y, z) \cos \theta; & \tau_{xz} &= \bar{\tau}_{xz}(y, z) \cos \theta \quad \dots \dots (2) \end{aligned}$$

in which $\bar{\sigma}_x$, $\bar{\sigma}_y$, $\bar{\sigma}_z$, $\bar{\tau}_{yz}$, $\bar{\tau}_{xy}$, and $\bar{\tau}_{xz}$ = functions of cross-sectional coordinates (y, z) only. Assumptions 5 and 6 suggest trying to satisfy the stress equilibrium equations of elasticity theory by assuming a normal stress distribution in the form

$$\sigma_x = -\frac{ER^2}{(R+z)} [C_0 + C_y y + C_z z] \sin \theta \quad (3)$$

in which C_0 , C_y , and C_z = constants to be determined. By substituting Eq. 3 into the stress equilibrium equations, the remaining stress components can be derived. These stress components are expressed in terms of the two stress functions $\phi(y, z)$ and $\Psi(y, z)$ as follows:

$$\sigma_x = -\frac{ER^2}{(R+z)} [C_0 + C_y y + C_z z] \sin \theta \quad (4)$$

$$\sigma_y = \left\{ \frac{R^2}{(R+z)^2} \phi_{,zz} - \frac{R}{(R+z)} \Psi_{,zz} + \frac{1}{2} \frac{ER^2}{(R+z)^2} \frac{dF(z)}{dz} [F(z) - y] [C_0 + 2C_y F(z)] \right\} \sin \theta \quad (5)$$

$$\sigma_z = \left(\frac{R^2}{(R+z)^2} \phi_{,yy} - \frac{R}{(R+z)} \Psi_{,yy} + \frac{1}{2} \frac{ER^2}{(R+z)} \left\{ C_0 \left[\frac{G(y)}{(R+z)} - 1 \right] + C_z \left[\frac{G^2(y)}{(R+z)} - \frac{2RG(y)}{(R+z)} + 2R - (R+z) \right] \right\} \right) \sin \theta \quad (6)$$

$$\tau_{xy} = \left\{ \frac{R^2}{(R+z)^2} \phi_{,yz} + \frac{1}{2} \frac{ER^2}{(R+z)^2} (C_0 y + C_y y^2) - \frac{1}{2} \frac{ER^2}{(R+z)^2} F(z) [C_0 + C_y F(z)] \right\} \cos \theta \quad (7)$$

$$\tau_{xz} = \left(-\frac{R^2}{(R+z)^2} \phi_{,yy} + \frac{1}{2} \frac{ER^2}{(R+z)^2} [C_0(R+z) + C_z(z^2 - R^2)] - \frac{1}{2} \frac{ER^2}{(R+z)^2} G(y) \left\{ C_0 + C_z [G(y) - 2R] \right\} \right) \cos \theta \quad (8)$$

$$\tau_{yz} = \left\{ \frac{R}{(R+z)} \Psi_{,yz} - \frac{R^2}{(R+z)^2} \phi_{,yz} - \frac{ER^2}{(R+z)^2} (C_0 y + C_y y^2) + \frac{1}{2} \frac{ER^2}{(R+z)^2} F(z) [C_0 + C_y F(z)] \right\} \sin \theta \quad (9)$$

in which $F(z)$ and $G(y)$ are defined along the cross-sectional boundary.

The stress expressions in Eqs. 4-9 are derived independent of the displacements u , v , and w . The stress components, or more specifically the stress functions ϕ and Ψ , cannot be taken as arbitrary functions of (θ, y, z) but are subject

to the two stress compatibility conditions to ensure the existence of displacements u , v , and w corresponding to these stresses. A set of constant stress-displacement relations can be derived by using the Hellinger-Reissner variational principle, which is a mixed principle. Then, two independent stress compatibility conditions can be derived from the five constant stress-displacement equations. They are

$$\sigma_{y,rr} + \sigma_{r,yy} - 2\tau_{yr,rr} - \nu [\sigma_{y,yy} + \sigma_{r,rr} + 2\tau_{yr,rr}] \\ = -2\nu \frac{ER^2}{r^3} (C_0 + C_y y - C_z R) \sin \theta \dots \dots \dots (10)$$

$$\sigma_{y,\theta r} - \frac{1}{r} \sigma_{y,\theta} + \nu \left\{ -\sigma_{r,\theta r} + \frac{1}{r} \sigma_{r,\theta} - \frac{2ER^2}{r^2} \left[C_0 + C_y y + \frac{1}{2} C_z (r \right. \right. \\ \left. \left. - 2R) \right] \cos \theta \right\} + (1 + \nu) \left[-\tau_{yr,\theta r} + r^2 \left(\frac{\tau_{\theta r}}{r} \right)_{,yy} - r^2 \left(\frac{\tau_{\theta r}}{r} \right)_{,yr} \right] = 0 \dots \dots (11)$$

in which $r = (R + z)$. Cartesian and cylindrical coordinates are used interchangeably as convenience dictates. The constants C_0 , C_y , and C_z in the assumed normal stress expression of Eq. 2 are determined from the following equilibrium conditions for any section of the curved bar.

$$\iint_A \sigma_x dydz = W \sin \theta \dots \dots \dots (12)$$

$$\iint_A y \sigma_x dydz = 0 \dots \dots \dots (13)$$

$$\iint_A z \sigma_x dydz = WR \sin \theta \dots \dots \dots (14)$$

The constants C_0 , C_y , and C_z are found to be

$$C_0 = 0; \quad C_y = \frac{W I_{yz}}{E(I_y I_z - I_{yz}^2)}; \quad C_z = \frac{W I_z}{E(I_y I_z - I_{yz}^2)} \dots \dots \dots (15)$$

in which $I_y = \iint_A [z^2/(1 + z/R)] dydz$; $I_z = \iint_A [y^2/(1 + z/R)] dydz$; and $I_{yz} = \iint_A [yz/(1 + z/R)] dydz$. By substituting Eqs. 4-9 into 10 and 11, the two governing partial differential equations for the stress functions ϕ and Ψ can be obtained.

$$\frac{R^2}{(R+z)^2} \phi_{,zzzz} - \frac{4R^2}{(R+z)^3} \phi_{,zzz} + \frac{6R^2}{(R+z)^4} \phi_{,zz} - \frac{R}{(R+z)} \Psi_{,zzzz} \\ + \frac{2R}{(R+z)^2} \Psi_{,zzz} - \frac{2R}{(R+z)^3} \Psi_{,zz} + \frac{R^2}{(R+z)^2} \phi_{,yyyy} - \frac{R}{(R+z)} \Psi_{,yyyy} \\ - \frac{2R}{(R+z)} \Psi_{,yyzz} + \frac{2R}{(R+z)^2} \Psi_{,yyz} + \frac{2R^2}{(R+z)^2} \phi_{,yyzz} - \frac{4R^2}{(R+z)^3} \phi_{,yyz}$$

$$\begin{aligned}
& -\nu \left\{ \frac{2R^2}{(R+z)^2} \phi_{,yyz} - \frac{2R}{(R+z)} \Psi_{,yyz} - \frac{4R^2}{(R+z)^3} \phi_{,yyz} + \frac{6R^2}{(R+z)^4} \phi_{,yy} \right. \\
& + \frac{2R^2}{(R+z)^2} \Psi_{,yyz} - \frac{2R}{(R+z)^3} \Psi_{,yy} + \frac{2R}{(R+z)} \Psi_{,yyz} - \frac{2R}{(R+z)^2} \Psi_{,yyz} \\
& \left. - \frac{2R^2}{(R+z)^2} \phi_{,yyz} + \frac{4R^2}{(R+z)^3} \phi_{,yyz} \right\} + \left[\frac{1}{2} \frac{ER^2}{(R+z)^2} \frac{dF(z)}{dz} (F(z) - y) \right. \\
& \times (C_0 + 2C_y F(z)) \Big]_{,zz} + \frac{1}{2} \frac{ER^2}{(R+z)} \left[\frac{C_0}{(R+z)} \frac{d^2 G(y)}{dy^2} + C_z \left(\frac{2}{(R+z)} G(y) \right. \right. \\
& \times \frac{d^2 G(y)}{dy^2} + \frac{2}{(R+z)} \left(\frac{dG}{dy} \right)^2 - \frac{2R}{(R+z)} \frac{d^2 G}{dy^2} \Big) \Big] - \frac{2ER^2}{(R+z)^3} (C_0 + 2C_y y) \\
& - \nu \left\{ \left[\frac{1}{2} \frac{ER^2}{(R+z)} \left[C_0 \left(\frac{G(y)}{(R+z)} - 1 \right) \right. \right. \right. \\
& \left. \left. + C_z \left(\frac{G^2(y)}{(R+z)} - \frac{2RG(y)}{(R+z)} + R - z \right) \right] \right]_{,zz} \\
& \left. + \frac{2ER^2}{(R+z)^3} (C_0 + 2C_y y) + \frac{2ER^2}{(R+z)^3} (C_0 + C_y y - C_z R) \right\} = 0 \dots \dots \dots (16)
\end{aligned}$$

$$\begin{aligned}
& \frac{R^2}{(R+z)^2} \phi_{,zzz} - \frac{3R^2}{(R+z)^3} \phi_{,zz} - \frac{R}{(R+z)} \Psi_{,zzz} + \frac{2R}{(R+z)^2} \Psi_{,zz} \\
& + \nu \left\{ - \frac{R^2}{(R+z)^2} \phi_{,yyz} + \frac{3R^2}{(R+z)^3} \phi_{,yy} + \frac{R}{(R+z)} \Psi_{,yyz} - \frac{2R}{(R+z)^2} \Psi_{,yy} \right\} \\
& + (1 + \nu) \left\{ - \frac{R}{(R+z)} \Psi_{,yyz} + \frac{R^2}{(R+z)^2} \phi_{,yyz} - \frac{R^2}{(R+z)} \phi_{,yyy} \right. \\
& \left. - \frac{R^2}{(R+z)} \phi_{,yyz} + \frac{3R^2}{(R+z)^2} \phi_{,yyz} \right\} \\
& + (R+z) \left[\frac{1}{2} \frac{ER^2}{(R+z)^3} \frac{dF(z)}{dz} (F(z) - y) (C_0 + 2C_y F(z)) \right]_{,z} \\
& - (R+z) \left[\frac{1}{2} \frac{EvR^2}{(R+z)^2} \left[C_0 \left(\frac{G(y)}{(R+z)} - 1 \right) + C_z \left(\frac{G^2(y)}{(R+z)} - \frac{2RG(y)}{(R+z)} \right. \right. \right. \\
& \left. \left. + R - z \right) \right] \right]_{,z} - \frac{2EvR^2}{(R+z)^2} \left(C_0 + C_y y + \frac{1}{2} C_z (z - R) \right) \\
& + (1 + \nu) \left\{ \frac{1}{2} \frac{ER^2}{(R+z)^2} (C_0 + 2C_y y) - \frac{1}{2} \frac{ER^2}{(R+z)} [G(y) [C_0 \right. \\
& \left. + C_z (G(y) - 2R)] \right]_{,yy} + \frac{3}{2} \frac{ER^2}{(R+z)^2} (C_0 + 2C_y y) \Big\} = 0 \dots \dots \dots (17)
\end{aligned}$$

The traction-free boundary conditions on the lateral surface of a curved bar yield the values

$$\phi_{,y} = \phi_{,z} = 0; \quad \Psi_{,y} = \Psi_{,z} = 0 \quad \dots \dots \dots (18)$$

for the stress functions along the cross-sectional boundaries.

The governing partial differential equations given in Eqs. 16 and 17 are too complicated to solve for the two unknown stress functions directly. The finite element formulation will be derived directly from a stationary condition of a functional for which Eqs. 16 and 17 are the Euler conditions.

FINITE ELEMENT ANALYSIS

The governing equations for the stress functions, ϕ and Ψ , as given in Eqs. 16 and 17 are too complex to be suitable for closed form solutions. A variationally based finite element procedure will be applied to obtain the solutions. The problem of integrating the partial differential Eqs. 16 and 17 subject to boundary conditions of Eq. 18 may be transformed into the problem of finding the unknown stress functions ϕ and Ψ which make stationary a functional subject to the same boundary conditions. The functional may be expressed in matrix form as

$$\Pi = \int \int [(\Phi)^T [C] (\Phi) - (\Phi)^T (F) + D] dy dz \quad \dots \dots \dots (19)$$

$$\text{in which } (\Phi) = \begin{Bmatrix} \phi_{,yy} \\ \phi_{,zz} \\ \phi_{,yz} \\ \Psi_{,yy} \\ \Psi_{,zz} \\ \Psi_{,yz} \end{Bmatrix} \quad \dots \dots \dots (20)$$

$$(F) = \left\{ \begin{array}{l} -\nu \frac{R^4}{(R+z)^2} (C_y y + C_z z) + \nu \frac{R^4}{(R+z)^3} C_y F(z) (F(z) - y) \frac{dF}{dz} \\ -\frac{1}{2} \frac{R^4}{(R+z)^2} C_z \left[\frac{G^2(y)}{(R+z)} - \frac{2RG(y)}{(R+z)} + R - z \right] + \frac{1}{2} \frac{E}{G} \frac{R^4}{(R+z)^3} \\ \times C_z [z^3 - R^2 G(y) [G(y) - 2R]] \\ \hline -\nu \frac{R^4}{(R+z)^2} (C_y y + C_z z) - \frac{R^4}{(R+z)^3} C_y F(z) [F(z) - y] \frac{dF(z)}{dz} \\ + \frac{\nu}{2} \frac{R^4}{(R+z)^2} C_z \left[\frac{G^2(y)}{(R+z)} - \frac{2RG(y)}{(R+z)} + R - z \right] \\ \hline -\frac{E}{G} \frac{R^4}{(R+z)^3} C_y [y^2 - F^2(z)] \end{array} \right\} \quad \dots \dots (21)$$

$$\left[\begin{array}{l} \nu \frac{R^3}{(R+z)} (C_y + C_z z) - \nu \frac{R^3}{(R+z)^2} C_y F(z) [F(z) - y] \frac{dF(z)}{dz} \\ + \frac{1}{2} \frac{R^3}{(R+z)} C_z \left[\frac{G^2(y)}{(R+z)} - \frac{2RG(y)}{(R+z)} + R - z \right] \\ \hline \nu \frac{R^3}{(R+z)} (C_y y + C_z z) + \frac{R^3}{(R+z)^2} C_y F(z) [F(z) - y] \frac{dF}{dz} \\ - \frac{\nu}{2} \frac{R^3}{(R+z)} C_z \left[\frac{G^2(y)}{(R+z)} - \frac{2RG(y)}{(R+z)} + R - z \right] \\ \hline \frac{1}{2} \frac{E}{G} \frac{R^3}{(R+z)^2} C_y [y^2 - F^2(z)] \end{array} \right]$$

$$D = \frac{1}{2} \frac{ER^4}{(R+z)} \left[(C_y y + C_z z)^2 + \frac{1}{4} \frac{1}{(R+z)^2} (C_z z^2)^2 \right. \\ \left. - \frac{\nu}{2} \frac{1}{(R+z)} (C_y y + C_z z)(C_z z^2) \right] \\ + \frac{1}{4} (1 + \nu) E \frac{R^4}{(R+z)^3} [2(C_y y^2)^2 + (C_z z^2)^2] \dots \dots \dots (22)$$

$$[C] = \left[\begin{array}{cccccc} (3+2\nu) \frac{R^4}{2E(R+z)^3} & -\frac{1}{2} \frac{\nu}{E} \frac{R^4}{(R+z)^3} & 0 & -\frac{1}{2E} \frac{R^3}{(R+z)^2} & \frac{1}{2} \frac{\nu}{E} \frac{R^3}{(R+z)^2} & 0 \\ -\frac{1}{2} \frac{\nu}{E} \frac{R^4}{(R+z)^3} & \frac{1}{2E} \frac{R^4}{(R+z)^3} & 0 & \frac{\nu}{2E} \frac{R^3}{(R+z)^2} & -\frac{1}{2E} \frac{R^3}{(R+z)^2} & 0 \\ 0 & 0 & \frac{1}{G} \frac{R^4}{(R+z)^3} & 0 & 0 & -\frac{1}{2G} \frac{R^3}{(R+z)^2} \\ -\frac{1}{2E} \frac{R^3}{(R+z)^2} & \frac{1}{2} \frac{\nu}{E} \frac{R^3}{(R+z)^2} & 0 & \frac{1}{2E} \frac{R^2}{(R+z)} & -\frac{\nu}{2E} \frac{R^2}{(R+z)} & 0 \\ \frac{\nu}{2E} \frac{R^3}{(R+z)^2} & -\frac{1}{2E} \frac{R^3}{(R+z)^2} & 0 & -\frac{\nu}{2E} \frac{R^2}{(R+z)} & \frac{1}{2E} \frac{R^2}{(R+z)} & 0 \\ 0 & 0 & -\frac{1}{2G} \frac{R^3}{(R+z)^2} & 0 & 0 & \frac{1}{2G} \frac{R^2}{(R+z)} \end{array} \right] \quad (23)$$

The procedure will be to idealize the cross-sectional domain by an assemblage of triangular elements. The functional Π may be approximated as the sum of functionals evaluated for each element. Mathematically, the functional may be written as

$$\Pi = \sum_{i=1}^M \Pi_i^{(e)} \dots \dots \dots (24)$$

in which i indicates the element number; and M = the total number of elements. At node j the stress functions and their first derivatives (slopes) with respect

to y and z are chosen as the unknown nodal parameters and are expressed in matrix form as

$$\{\phi_j\}^T = [\phi_j \quad -\phi_{,y,j} \quad \phi_{,z,j} \quad \psi_j \quad -\psi_{,y,j} \quad \psi_{,z,j}] \quad \dots \quad (25)$$

The stress function behavior within each element may be written in terms of their nodal parameters

$$\begin{Bmatrix} \phi(y, z) \\ \psi(y, z) \end{Bmatrix}^e = [N]^e \{\phi_j\}^e \quad \dots \quad (26)$$

in which $[N]^e$ is a shape function matrix and $\{\phi_j\}^e$ is a vector of the unknown nodal parameters. The vector of derivatives in Eq. 20 may be obtained by differentiating Eq. 26 with respect to y and z . Thus

$$\{\Phi\} = [B]^e \{\phi_j\}^e \quad \dots \quad (27)$$

in which elements of matrix $[B]^e$ are the second derivatives of the shape functions with respect to y and z as defined in Eq. 20. The discretized functional for element i is obtained in terms of the unknown nodal parameters by substituting Eq. 27 into 19

$$\Pi_i^{(e)} = \iint_{A_i} [(\phi_j^e)^T [B^e]^T [C] [B^e] \{\phi_j^e\} - \{\phi_j^e\}^T [B^e]^T \{F\} + D] dydz \quad (28)$$

where integration is performed over the element domain A_i . Finally the total functional is obtained by collecting the contributions from all discretized functionals within the cross-sectional domain.

$$\begin{aligned} \Pi(y, z, \phi_j) &= \sum_{i=1}^M \iint_{A_i} [(\phi_j^e)^T [B^e]^T [C] [B^e] \{\phi_j^e\} \\ &- \{\phi_j^e\}^T [B^e]^T \{F\} + D] dydz \quad \dots \quad (29) \end{aligned}$$

The stationary solution of the functional Π can be derived from the condition that the variation of the functional $\Pi(y, z, \phi_j)$ with respect to the unknown nodal parameters vanishes. That is

$$\delta \Pi(y, z, \phi_j) = \sum_{i=1}^M \frac{\partial \Pi_i}{\partial \phi_j} \delta \phi_j = 0 \quad \text{for } j = 1, 2, \dots, N \quad \dots \quad (30)$$

in which N is the number of nodes on the cross section.

NUMERICAL RESULTS

The formulation will be applied to two curved bar cross sections. First, a homogeneous thin curved bar of rectangular cross section will be used so that the calculated stresses can be compared with an analytical solution available from plane elasticity theory. The second example is chosen to be a curved box section.

Homogeneous Thin Curved Bar of Rectangular Cross Section.—The thin rectangular curved bar of Fig. 2(a) has a 1 in. (0.0254 m) width, 10 in. (0.254 m) depth, and a radius of curvature of 20 in. (0.508 m). The cross section

is subjected to an internal shear force in the radial direction of 10,000 lb (44.48 kN) at its centroid. The discretized model of the cross section is shown in Fig. 2(b) and partial computer results are presented in Table 1. The stress results obtained by the present formulation are compared in Table 2 and Fig. 3 with those obtained from the plane elasticity theory. The direct shear stresses based on the present formulation are the average values across the bar width.

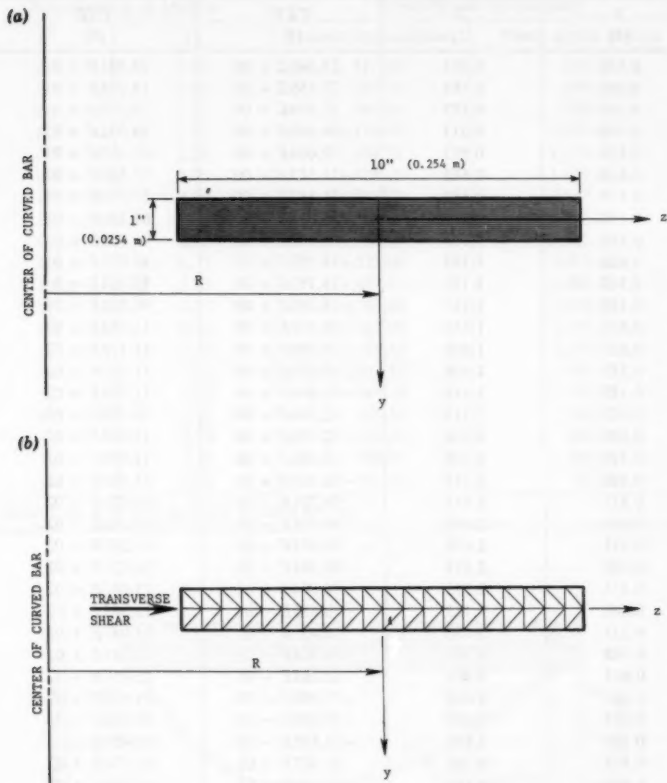


FIG. 2.—Thin Curved Bar Subjected to Transverse Shear: (a) Dimensions; (b) Finite Element Representation

Homogeneous Curved Box Girder Subjected to Direct Shear Force.—The second problem demonstrates the applicability of the method of analysis to a more complicated cross-sectional configuration. Choose the curved box section of Fig. 4. It is made of steel with a modulus of elasticity and Poisson's ratio of 30×10^6 psi (206.85 GN/m^2) and 0.3, respectively. The section is subjected

TABLE 1.—Shear Stresses due to Shear Forces (in pounds per square inch) on Thin Curved Bar Section of Fig. 2

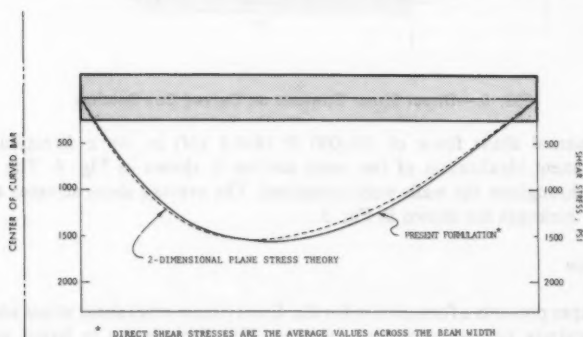
Coordinates of Element Centroid		Shear Stresses	
Y (1)	Z (2)	TXY (3)	TXZ (4)
0.813	0.313	24.640E + 00	24.335E + 01
0.688	0.188	-27.859E + 00	19.225E + 01
0.313	0.188	27.859E + 00	19.225E + 01
0.188	0.313	-24.640E + 00	24.335E + 01
0.813	0.813	22.034E + 00	61.280E + 01
0.688	0.688	-21.587E + 00	57.500E + 01
0.313	0.688	21.587E + 00	57.500E + 01
0.188	0.813	-22.034E + 00	61.280E + 01
0.813	1.313	18.585E + 00	90.825E + 01
0.688	1.188	-18.192E + 00	88.061E + 01
0.313	1.188	18.192E + 00	88.061E + 01
0.188	1.313	-18.585E + 00	90.825E + 01
0.813	1.813	15.448E + 00	11.382E + 02
0.688	1.688	-15.039E + 00	11.192E + 02
0.313	1.688	15.039E + 00	11.192E + 02
0.188	1.813	-15.448E + 00	11.382E + 02
0.813	2.313	12.568E + 00	13.105E + 02
0.688	2.188	-12.148E + 00	12.989E + 02
0.313	2.188	12.148E + 00	12.989E + 02
0.188	2.313	-12.568E + 00	13.105E + 02
0.813	2.813	99.201E - 01	14.321E + 02
0.688	2.688	-94.915E - 01	14.267E + 02
0.313	2.688	94.915E - 01	14.267E + 02
0.188	2.813	-99.201E - 01	14.321E + 02
0.813	3.313	74.804E - 01	15.087E + 02
0.688	3.188	-70.455E - 01	15.087E + 02
0.313	3.188	70.455E - 01	15.087E + 02
0.188	3.313	-74.804E - 01	15.087E + 02
0.813	3.813	52.285E - 01	15.457E + 02
0.688	3.688	-47.894E - 01	15.502E + 02
0.313	3.688	47.894E - 01	15.502E + 02
0.188	3.813	-52.285E - 01	15.457E + 02
0.813	4.313	31.467E - 01	15.474E + 02
0.688	4.188	-27.049E - 01	15.558E + 02
0.313	4.188	27.049E - 01	15.558E + 02
0.188	4.313	-31.467E - 01	15.474E + 02
0.813	4.813	12.189E - 01	15.178E + 02
0.688	4.688	-77.581E - 02	15.294E + 02
0.313	4.688	77.581E - 02	15.294E + 02
0.188	4.813	-12.189E - 01	15.178E + 02

Note: 1 in. = 0.0254 m; 1 psi = 6.895 kN/m².

TABLE 2.—Comparison of Shear Stresses (in pounds per square inch) along Center Line of Thin Curved Bar of Fig. 2 Obtained by Present Formulation with those of Two-Dimensional Plane Stress Theory

Coordinates, in inches		Direct Shear Stress (psi)	
y'	z'	Present formulation	Plane stress theory
0.5	0.25	217.80	244.69
0.5	0.75	593.90	650.58
0.5	1.25	894.43	960.69
0.5	1.75	1,128.70	1,190.69
0.5	2.25	1,304.70	1,353.40
0.5	2.75	1,429.40	1,459.40
0.5	3.25	1,508.70	1,517.50
0.5	3.75	1,547.95	1,535.01
0.5	4.25	1,551.50	1,518.06
0.5	4.75	1,523.60	1,471.81
0.5	5.25	1,467.55	1,400.58
0.5	5.75	1,386.40	1,308.04
0.5	6.25	1,283.05	1,197.31
0.5	6.75	1,159.65	1,071.03
0.5	7.25	1,018.55	931.45
0.5	7.75	861.51	780.52
0.5	8.25	690.26	619.87
0.5	8.75	506.31	450.95
0.5	9.25	310.97	274.96
0.5	9.75	105.47	92.96

Note: 1 in. = 0.0254 m; 1 psi = 6.895 kN/m².



* DIRECT SHEAR STRESSES ARE THE AVERAGE VALUES ACROSS THE BEAM WIDTH

FIG. 3.—Direct Shear Stress Distributions Along Center Line of Bar of Fig. 2 (1 in. = 0.0254 m; 1 psi = 6.895 kN/m²)

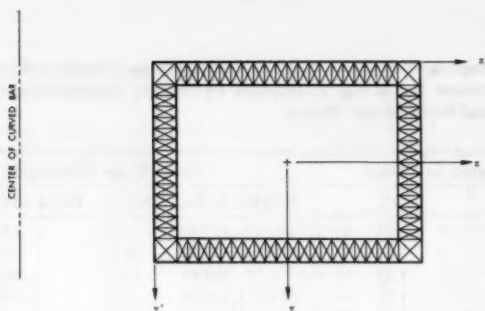


FIG. 4.—Finite Element Representation of Curved Box Section

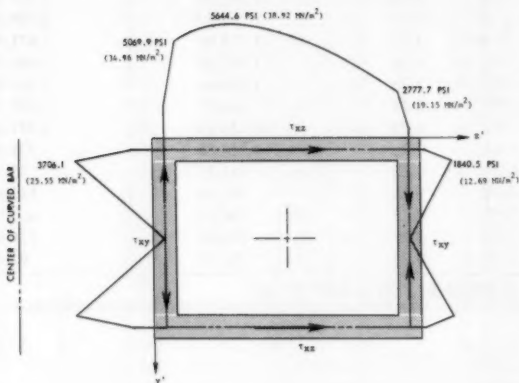


FIG. 5.—Direct Shear Stresses on Curved Box Section

to an internal shear force of 100,000 lb (444.8 kN) in the z direction. The finite element idealization of the cross section is shown in Fig. 4. The shear stresses throughout the walls were computed. The average shear stresses across the wall thickness are shown in Fig. 5.

CONCLUSION

The paper presents a formulation for the direct (transverse) shear stress analysis of a circularly curved structural member. The formulation is based on the three-dimensional theory of elasticity. The assumption "stresses at any cross section depend only on the internal forces at that particular cross section" enables the three dimensional elasticity theory to be reduced to the determination of the stresses at a particular (two-dimensional) cross section. Although the solution is based on a cantilevered bar with a particular applied loading, this

formulation can be used to compute the transverse shear stresses for a circularly curved bar with any boundary conditions and arbitrary loading. Thus, the formulation requires only that the internal forces be known on the cross section where the shear stresses are sought.

ACKNOWLEDGMENTS

This work was supported by the Office of Naval Research.

APPENDIX.—REFERENCES

1. Thasanatorn, C., and Pilkey, W. D., "Torsional Stresses in Circularly Curved Bars," *Journal of the Structural Division*, ASCE, Vol. 105, No. ST11, Proc. Paper 14984, Nov., 1979, pp. 2327-2342.
2. Timoshenko, S. P., and Goodier, J. N., *Theory of Elasticity*, 3rd ed., McGraw-Hill Book Co., Inc., New York, N.Y., 1970.

WIND LOADS ON EAVES OF LOW BUILDINGS

By Theodore Stathopoulos,¹ M. ASCE

INTRODUCTION

In the assessment of wind loads on roofs, the effect of eaves (otherwise called canopies or overhangs) is sometimes overlooked. Windward eaves, however, may be loaded severely due to wind, since the deflected flow from the windward wall gives rise to a pressure on the lower eave surface, which reinforces the high suction of the upper eave surface right after separation. Unfortunately, only a limited amount of information is available on the subject. This is the reason why most Standards and Codes of Practice have poor documentation of provisions relative to wind loads on eaves; in fact, they rarely include any such provisions at all.

Leutheusser (5) has published a comprehensive study on mean wind loads on eaves using models of various geometries, but he performed all his tests under uniform wind conditions (no velocity variation with height). Thus, his test conditions did not simulate natural wind effects, and therefore his results may not be representative. Dreher and Cermak (4) have examined local pressures on upper and lower eave surfaces in a boundary layer wind tunnel simulating natural wind conditions. Their measurements have been limited in one geometrical configuration only, but they have reported that pressures underneath the overhangs can account for 50% of the total wind load acting on the overhangs of a house. In contrast, Tieleman and Reinhold (10) have concluded that the presence, or absence, of eaves does not influence the magnitude of the wind pressures a great deal, i.e., the same pressure loads may apply on roofs with or without overhangs. Finally, Best and Holmes (2) have examined local pressures on eaves of a low-rise building model and have recognized that combining the negative peak values on the top with the positive peak values under the eave is somewhat conservative, since peak values do not occur together.

The lack of pertinent information regarding wind loads on eave sections, in combination with reports of severe wind damages on these areas, have led Code and Standard Committee Officials to significantly increase wind design specifications for eaves. Ref. 6, for instance, states that the Building Code

¹Asst. Prof. of Engrg., Centre for Building Studies, Concordia Univ., 1455 de Maisonneuve Blvd. W., Montreal, Quebec, Canada H3G 1M8.

Note.—Discussion open until March 1, 1982. To extend the closing date one month, a written request must be filed with the Manager of Technical and Professional Publications, ASCE. Manuscript was submitted for review for possible publication on October 31, 1980. This paper is part of the Journal of the Structural Division, Proceedings of the American Society of Civil Engineers, ©ASCE, Vol. 107, No. ST10, October, 1981. ISSN 0044-8001/81/0010-1921/\$01.00.

of Japan increased the wind loads for the design of eaves by 300% in 1973. No research work, however, appears to justify such a decision.

It is the purpose of this paper to describe the results of some recent experimental measurements of mean and fluctuating wind loads on eaves of low-rise buildings (8). Both local and spatially distributed loads over various eave areas have been measured, and the importance of the variation of dynamic action of wind with tributary areas of structural elements has been demonstrated. All measurements have been carried out for a variety of representative low-rise building geometries in turbulent flow conditions characteristic of the natural wind. Two terrain types and all critical wind directions have been considered. The analysis of the experimental data has finally led to some recommendations for design standards and Codes of Practice.

EXPERIMENTAL MEASUREMENTS

The experiments have been carried out in the Boundary Layer Wind Tunnel Laboratory of the University of Western Ontario. This well-known tunnel has

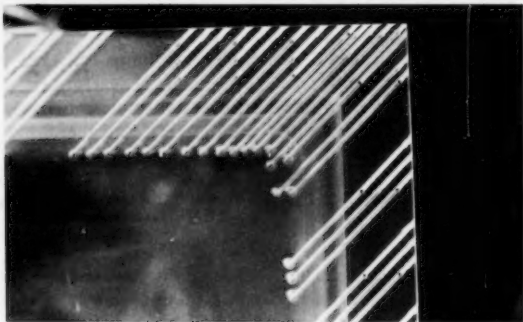


FIG. 1.—Detail of Model with Large Eave Section (Roof Corner)

a working section of about 80 ft (24 m) long, 8 ft (2.5 m) wide, and about 7 ft (2 m) high. Most of the fetch is required for the natural production of a boundary layer which grows in a manner paralleling the atmospheric process under neutral conditions. A detailed description of the tunnel has been given in Ref. 3. Two terrain models have been used for the measurements reported here, representing open country and suburban (built-up) full-scale conditions, respectively. The velocity and longitudinal turbulence intensity profiles measured at the test section without the model in position are representative of exposures *A* and *B* of the National Building Code of Canada (7) or *C* and *B* of the American National Standards Institute (ANSI) Standard (1).

The pressure measuring system used responds to pressure fluctuations on the model of up to about 100 Hz with negligible attenuation or distortion. Several pressure measurements can be made in parallel, each of which is sampled at a rate of about 1,000/sec. Sampling is continued for a period of up to about

30 sec in real time during which a computer records, for each input, the maximum and minimum values that occur, and computes the mean and root-mean-square values. At the end of the sampling period, the measured pressures are converted to pressure coefficients by dividing each by the reference dynamic pressure. The latter is measured in the free stream above the boundary layer where the wind speed is approx 50 ft/sec (15 m/s).

The basic models used for the measurements of wind loads on eaves represent (at a scale of 1:250) a 1:12 roof-sloped building, 80 ft (24 m) wide and 125 ft (38 m) long. Three different eave heights were tested corresponding to 16 ft, 24 ft, and 32 ft (5 m, 7.5 m, and 10 m) in full scale. Eaves of two different widths representing 5 ft and 10 ft (1.5 m and 3 m) in full scale were constructed

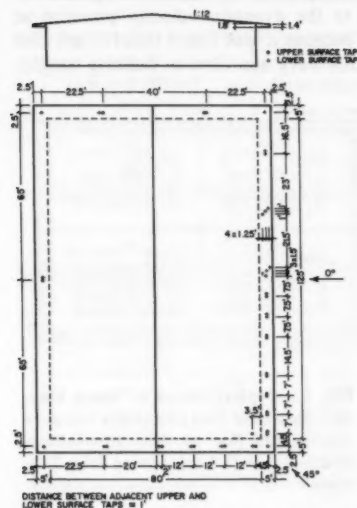


FIG. 2.—Exploded Plan View of 5-ft Eave Model Showing Pressure Measuring Locations (Note: 1 ft = 0.305 m)

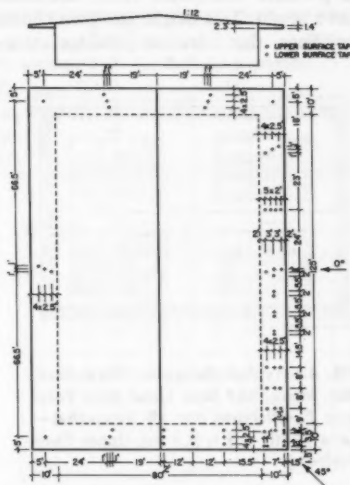


FIG. 3.—Exploded Plan View of 10-ft Eave Model Showing Pressure Measuring Locations (Note: 1 ft = 0.305 m)

as extensions of the roof surface perimetrically. The eave sections were equipped with pressure taps located on both upper and lower surfaces. Fig. 1 shows a picture from the top of a corner eave section of one of the models. The holes for upper and lower surface points of measurement have been drilled on the eave sections after drilling the path for the transmission of air into the tubing and pressure transducer. Because of the small thickness of the eave, this path for each pressure tap had to be drilled from the edge of the eave at an angle of 45°. The thickness of the eave was subsequently restored by plugging up the small part of the path between pressure tap and eave perimeter.

Figs. 2 and 3 show the pressure tap arrangement for both upper and lower surfaces of the models with smaller and larger eaves, respectively. The former

model was equipped with 44 pressure taps (22 on each surface), whereas the latter had 58 taps (24 on the lower and 34 on the upper surface). As can be seen, the pressure taps have been arranged in such a manner that measurement of local and area loads could be carried out at any region of interest. The close proximity of pressure taps on upper and lower surfaces serves the purpose of monitoring the total wind load acting on the eave at any instant.

LOCAL PRESSURES

Experimental data of local pressure measurements carried out for the small eave section [(eave width/building width) = 0.0625] have been summarized in Figs. 4 and 5 for upper and lower surfaces, respectively. Results are presented in pressure coefficient form referenced to the dynamic velocity pressure at eave height. This height has been chosen because it was found that for low-rise buildings, this selection provides values not very sensitive to building height.

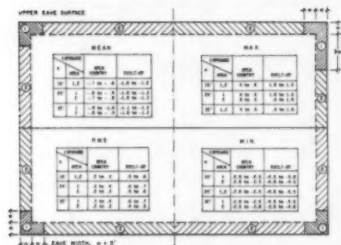


FIG. 4.—Typical Range of Worst Max, Min, Mean, and Rms Local Eave Pressure Coefficients (for all Azimuths)—Eave Width = 5 ft (1.5 m), Upper Eave Surfaces

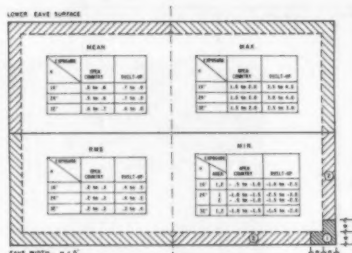


FIG. 5.—Typical Range of Worst Max, Min, Mean and Rms Local Eave Pressure Coefficients (for all Azimuths)—Eave Width = 5 ft (1.5 m), Lower Eave Surfaces

The measured pressure coefficients (referenced to gradient height) had thus to be converted to the new reference height, and this was done by using the experimentally determined variation of the wind speed with height. Table 1 shows the relationship of wind speeds at eave height and gradient height for the two terrain roughnesses. Pressure coefficients are defined as follows:

$$C_{p_{\max}} = \frac{P_{\max}}{q_H}, C_{p_{\min}} = \frac{P_{\min}}{q_H}, C_{p_{\text{mean}}} = \frac{P_{\text{mean}}}{q_H}, C_{p_{\text{rms}}} = \frac{P_{\text{rms}}}{q_H} \dots \dots \dots (1)$$

in which P_{\max} = the maximum instantaneous pressure measured over the sampling period; P_{\min} = the minimum instantaneous pressure measured over the sampling period; P_{mean} = the temporal mean pressure; P_{rms} = the root-mean-square pressure $[(P - P_{\text{mean}})^2]^{1/2}$; $q = 1/2 \rho \bar{V}_H^2$ = the dynamic velocity pressure associated with the mean wind speed, \bar{V}_H , at eave height; and all pressures are differential pressures with respect to the static pressure at gradient height.

The approximate range of local pressure coefficient values is indicated in

Figs. 4 and 5 for all wind azimuths (0° – 360° at 45° intervals), two terrain roughnesses and three building eave heights. By virtue of symmetry, only one quarter of the perimeter eave is necessary for the most critical pressure coefficient values. Zones 1 and 2 appearing on the overhangs have been determined somewhat subjectively and their boundaries should be considered very approximate. Fig. 4 shows that zone 1 is also larger for the maximum instantaneous pressure coefficients than for the minimum mean and root-mean-square pressure coefficients acting on the upper eave surface. It is interesting to note, however, the more uniform distribution of the lower eave surface pressure coefficients (Fig. 5) in comparison to the upper eave surface coefficient distribution (Fig. 5).

TABLE 1.—Ratios of Wind Speeds at Eave Height and Gradient Height

Eave height H , in feet (1 ft = 0.305 m) (1)	\bar{V}_H / V_G	
	Open-country exposure (2)	Built-up exposure (3)
16	0.544	0.373
24	0.589	0.401
32	0.618	0.457

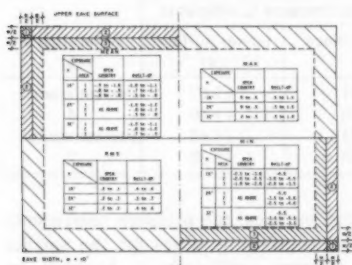


FIG. 6.—Typical Range of Worst Max, Min, Mean and Rms Local Eave Pressure Coefficients (for all Azimuths)—Eave Width=10 ft (3 m), Upper Eave Surfaces

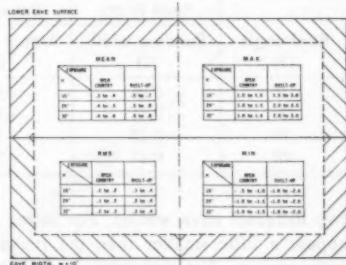


FIG. 7.—Typical Range of Worst Max, Min, Mean and Rms Local Eave Pressure Coefficients (for all Azimuths)—Eave Width=10 ft (3 m), Lower Eave Surfaces

4). The small dependence of coefficients on building height also, as previously mentioned, is apparent for all cases.

In general, results have somewhat lower values than were found for roof edges and corners of similar buildings without eaves exposed to the same terrain (8). This difference appears to be due primarily to the pressure taps being slightly farther from the edges than in the no-eave case. Obviously, some flow differences also exist. Nevertheless, the present results provide representative local loads on small eave sections around the roof. Mean pressure coefficients are positive for lower eave surfaces and their values are somewhat lower than the absolute values of mean pressure coefficients for the upper surfaces. Also,

the rms local coefficients are smaller for the lower eave surfaces, particularly for the higher heights and the rougher exposure.

Pressure coefficient values are higher for the built-up (suburban) exposure. This does not mean, however, that pressures are higher in the rougher exposure. In contrast, pressures are generally lower for higher terrain roughnesses because of the decreased dynamic velocity pressure at eave height in which all pressure coefficients are referenced.

Figs. 6 and 7 show ranges of upper and lower eave surface local pressure coefficients in a similar fashion for the larger eave section [(eave width/building width) = 0.125]. The number of areas for which the range of minimum and mean pressure coefficients for eave upper surface is given (Fig. 6) has been increased due to the rapid reduction of local pressures with distance from the edge. Maximum and rms values are quite uniform, so the number of areas has been minimized for them. Mean pressure coefficients for the outer eave surfaces appear somewhat higher than in the case of the smaller eave section. This may be, again, due to the closer proximity to the edge of the pressure taps used in the case of larger eave section or to alterations of the flow due to the big eave. Generally, the pattern of local pressures is similar for the

TABLE 2.—Extreme Local Pressure Coefficients for Upper and Lower Eave Surfaces

Roof angle (1)	Eave Width	Extreme Pressure Coefficients		Reference # (5)
	Building width (2)	Upper surface (3)	Lower surface (4)	
5°	0.06	-3.01	+2.07	Present study 4
13°	0.11	-3.50	+1.60	
5°	0.12	-3.25	+1.62	Present study 2
10°	0.17	-5.04	+2.82	

two different eave widths. For lower eave surfaces, the pressure coefficients appear a little smaller than the respective coefficient values for the smaller eave section. The distribution of these pressure coefficients is, however, as uniform as in the case of the smaller eave.

Table 2 compares the extreme local pressure coefficients reported from the measurements on upper and lower eave surfaces. Only studies conducted in simulated atmospheric boundary layers have been considered for the comparison. Despite the fact that there are geometrical and other minor terrain roughness differences between these studies, data show a fair agreement. The higher values of Ref. 2, however, may be attributed to the higher "eave width over building width" ratio. Nevertheless, more data are required to increase confidence in the reported values.

AREA LOADS

Fig. 8 indicates all the areas and uplift forces considered in both cases of small and large eave width. Vertical load coefficients were measured over different eave areas either separately or simultaneously on both surfaces by using the

pneumatic manifolding technique alone or in combination with the computer weighting method (8). The computation of the total load acting on various areas of eave sections was carried out "on-line" with a digital computer sampling one of: (1) Independent pressures; (2) independently manifolded upper and lower surface loads; or (3) the difference of the upper and lower local loads derived by using both sides of a pressure transducer simultaneously.

The component loads were weighted by appropriate tributary area factors determined for each pressure tap as the percentage of the total area over which the local pressure measured had been considered to be representative.

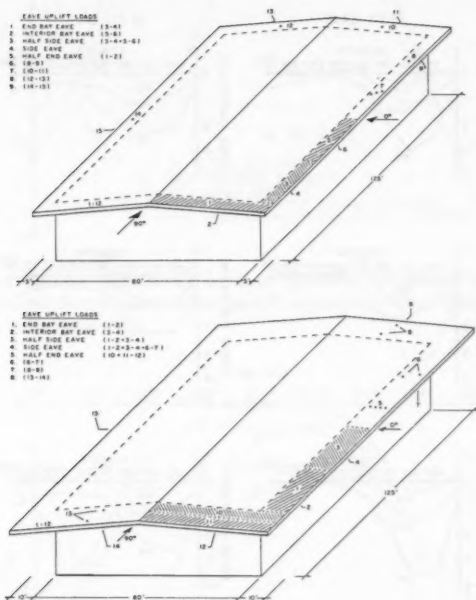


FIG. 8.—Eave Areas Examined (Note: 1 ft = 0.305 m)

Typical results of maximum, mean, and minimum vertical force coefficients for a half-end eave of a building exposed to open country terrain are presented in Fig. 9. Data are given for three eave heights, two eave widths, and all azimuths tested. As expected, critical loads occur for 45° and 90° azimuths for the half-end eave considered. The little dependence on height of the coefficients is also apparent. The loads appear consistently higher for the smaller eave width. Similar trends have also been found for the built-up (suburban) exposure.

Comparison of extreme vertical force coefficients with the difference of local coefficients obtained for points on the upper and lower eave surfaces (results summarized in Figs. 4-7) indicates some alleviation for area loading due to the beneficial (from the designer's point of view) lack of spatial correlation

of local pressures acting inside an area on the upper or lower eave surface. This is shown in Fig. 10 where experimental data are presented for the extreme suction acting on the end-bay eave, interior bay eave and half-end eave (as defined in Fig. 8) of a 16 ft (5 m) high building with an eave width of 5 ft (1.5 m) exposed in open country terrain. The solid lines of Fig. 10 represent the effective values measured, and these should be used for the design loads of eave sections. In contrast, the dashed lines indicate the calculated values assuming that peaks of upper and lower surface area loads occur simultaneously, no matter when in the record the peaks actually occurred. The alleviation found

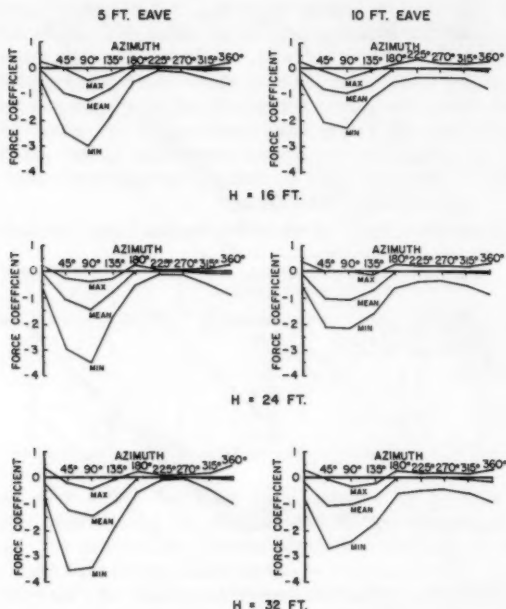


FIG. 9.—Mean and Peak Values of Vertical Force Coefficients for Half-End Eave (Open-Country Exposure)

by taking into account the true loads is in the order of 20% for the most critical azimuth (design case).

Similar results appear in Fig. 11 for the building with a 10-ft (3.0-m) wide perimeter eave. In this case, the alleviation is even higher—approx 30% for the most critical azimuths (0° or 90°). It should also be noted that this alleviation would be even higher if the true effective loads acting on eave sections were compared with the individual upper and lower surface area loads based on the envelope of extreme local pressure measurements; the latter used to be the common practice until very recently. This is shown in Fig. 12 where data

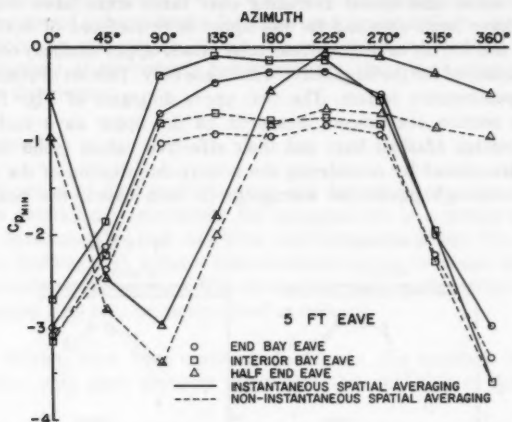


FIG. 10.—Peak Suction Coefficients on Eave Sections of Various Sizes by Using Instantaneous and Noninstantaneous Spatial Averaging—Eave Height = 16 ft (5 m), Exposure = Open Country

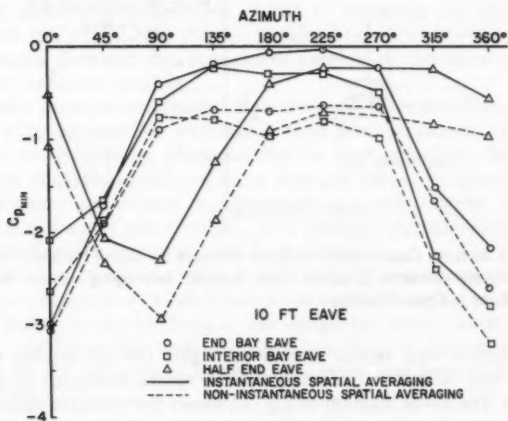


FIG. 11.—Peak Suction Coefficients on Eave Sections of Various Sizes by Using Instantaneous and Noninstantaneous Spatial Averaging—Eave Height = 16 ft (5 m), Exposure = Open Country

of extreme instantaneous suction coefficients acting on eave corner sections are presented. Measurements on individual pressure taps of smaller and larger eave corner areas and spatial averaging over these areas have been carried out. Loads have been obtained for the upper eave surfaces of both 5 ft and 10 ft (1.5 m and 3.0 m) eaves, whereas total (lower-upper surface) corner loads have been measured for the larger eave width case only. This set of measurements is for an open-country terrain. The two upper diagrams of Fig. 12 indicate the extreme suction coefficients measured on the upper eave surface, their arithmetic average (dashed line) and their effective values (solid line) which have been determined by considering the nonsynchronization of the individual peak values through pneumatic averaging. In both cases, the peak suction

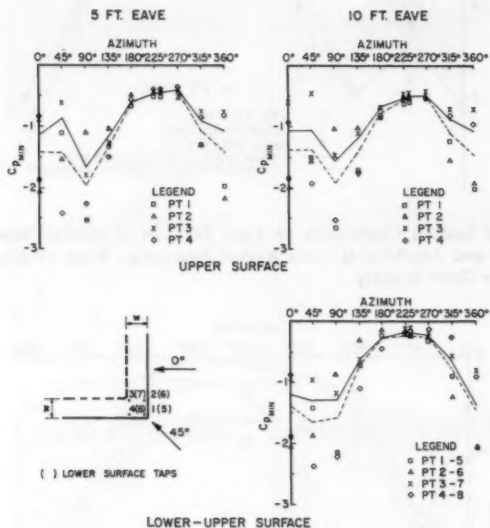


FIG. 12.—Peak Suction Coefficients on Eave Corners by Using Instantaneous (Solid Line) and Noninstantaneous (Dashed Line) Spatial Averaging—Eave Height = 16 ft (5 m), Exposure = Open Country

coefficients appear very similar (somewhat higher for the smaller eave) and a significant load reduction is apparent when spatial averaging is taken into consideration. The lower diagram of Fig. 12 shows the effective suction coefficients for the simultaneous wind action on upper and lower corner surfaces for the large eave section in a similar fashion. In addition to the alleviation due to spatial averaging, previously described, it is very interesting to note here that the maximum total uplift coefficients are not significantly higher than the suction coefficients loading the upper eave surface; in fact, they have somewhat smaller values for the critical azimuths. This beneficial result can be attributed to the low positive pressure or suction acting underneath the eave

corner and to favorable correlation of loads acting on the two eave surfaces.

All of the preceding shows the amount of conservatism involved when the upper bound load coefficient, which is derived by simple subtraction of worst case data measured independently for upper and lower surfaces, is considered. Unfortunately, no comparison of the present results with other studies can be made, because, to the writer's best knowledge, there is no other information available in this respect.

DATA CODIFICATION

The implication of data codification is the derivation of a simplified chart of pressure coefficients appropriate for incorporation in a design standard or a Code of Practice. This task has been undertaken previously for wind loads on low-rise buildings (9) without special consideration to eaves except some specifications for canopy corners. The main assumptions made for the codification of eave loading data may be summarized as follows:

1. Gust effects have been retained directly in the pressure coefficients; consequently, only peak pressure coefficients are included in the simplified chart.
2. Eave height and eave width have not been considered as critical parameters for the determination of effective pressure coefficients for design purposes. Consequently, only "worst case" data have been considered; i.e., the configuration (height and width) with the heaviest loading measured has been taken into account.
3. Terrain effects were significant enough to encourage the maintenance of two different sets of data for the two terrains examined; however, at present the code model proposed has been based entirely on the more conservative open country exposure results.
4. Effective pressure coefficients have been determined as functions of the respective tributary area for which they have been measured, since this has been found to be a strong parameter for the load definition. Data for eave corners have not been considered since they are limited in quantity and they suggest extremely low values in comparison with other areas. However, if additional data support these results, it is strongly recommended to include separate specifications for these areas in the chart.
5. For each configuration examined, the worst values of measured pressure coefficients—regardless of wind direction—have been considered. To avoid the significant conservatism involved in the design for such "worst cases," the designated coefficient has been established at 80% of the maximum value. Arguments for the adoption of the 80th percentile level have been considered in detail in Ref. 9.

Based on the assumptions stated, the codified eave pressure coefficients are presented in Fig. 13. The effective pressure coefficients given in the chart are total coefficients appropriate to be used for the design of eave sections against wind loads acting on both upper and lower surfaces. These values have been based on the bulk of experimental data for all configurations examined and do not reflect only the representative cases presented in this paper. The maximum

design pressure, P (in pounds per square foot) is given by the equation:

$$P = q_H C_p \dots \dots \dots (2)$$

in which $q_H = 0.00256 \bar{V}_H^2$, \bar{V}_H = mean hourly wind speed at eave height, in miles per hour; and C_p = the designated effective pressure coefficient. Note that, by virtue of assumption 3 above, the designated coefficients are appropriate for open country terrain conditions, but they will give conservative wind pressures when they apply to another exposure.

It is recommended that the pressure coefficients of Fig. 13 be used for wind loads on perimeter eaves of low-rise buildings whose eave height does not exceed 60 ft (18 m), (eave width/building width) ≤ 0.12 , and roof angle does not exceed 10° (8). The proposed height limit which is approximately double the maximum height of model tested, is justified from additional tests carried out and not described in this paper. For higher heights or roof slopes (or both)

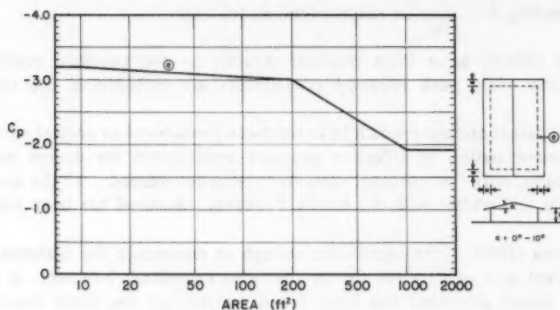


FIG. 13.—Codified Pressure Coefficients for Maximum Loads on Eave Sections (Open-Country Exposure) (Note: $1 \text{ ft}^2 = 0.093 \text{ m}^2$)

or different eave sizes and configurations (for instance overhangs on two opposite sides of building only) additional data are required for design specifications.

CONCLUSIONS

The results of a study of wind loads on perimeter eaves of low-rise buildings have been described in this paper. The most significant conclusions can be summarized as follows:

1. Windward eave sections are very sensitive to wind loading. Suction loads dominate on the upper eave surface; pressure loads appear on the lower eave surface with the exception of the overhang corner for which low positive or negative pressures act for critical azimuths.
2. Appropriate evaluation of eave wind loads cannot be made by considering the local pressures acting on various points of upper and lower eave surfaces as used to be common practice in the past. Instead, the effective loading of eave sections has to be determined by monitoring the statistics of the total

load acting on both canopy surfaces at any instant.

3. A codified chart of design pressure coefficients has been suggested. The design pressures are appropriate for perimeter eave sections of low-rise buildings not exceeding 60 ft (18 m) in height and 10° in roof angle. The eave width should be smaller than 12% of the building width. Additional data are required for other geometries.

ACKNOWLEDGMENTS

The writer would like to acknowledge the support and advice given by A. G. Davenport and D. Surry, of the University of Western Ontario, during the first stage of the work described in this paper. Financial assistance for the experimental measurements was provided by the National Research Council of Canada, the Metal Building Manufacturers Association, the American Iron and Steel Institute, the Canadian Steel Industries Construction Council, and the Boundary Layer Wind Tunnel Laboratory of the University of Western Ontario.

APPENDIX I.—REFERENCES

1. "American National Standard Building Code Requirements for Minimum Design Loads in Buildings and other Structures," *ANSI Standards*, American National Standards Institute, A58.1-1972.
2. Best, R. J., and Holmes, J. D., "Model Study of Wind Pressures on An Isolated Single-Storey House," *Wind Engineering Report 3178*, Department of Civil and Systems Engineering, James Cook University of North Queensland, Australia, Sept., 1978.
3. Davenport, A. G., and Isyumov, N., "The Application of the Boundary Layer Wind-Tunnel to the Prediction of Wind Loading," *Proceedings of the International Symposium of Wind Effects on Buildings and Structures*, Paper No. 7, 1967, pp. 201-230.
4. Dreher, K. J., and Cermak, J. E., "Wind Loads on a House Roof," *Report CER 72-73, KJD-JEC22*, Colorado State University, College of Engineering, Ft. Collins, Colo., Mar., 1973.
5. Leutheusser, H. J., "The Effects of Eaves on the Roof Pressure-Coefficients of Block-Type and Cylindrical Structures," *UT Mech E TP 6503*, University of Toronto, Department of Mechanical Engineering, Apr., 1965.
6. Murota, T., "Study on the Wind Effect on Eaves," *NBS Special Publication 477*, Wind and Seismic Effects, Proceedings of the Eighth Joint UJNR Panel Conference, May, 1976 (issued May, 1977).
7. "National Building Code of Canada 1975," *NRCC No. 13982*, National Research Council of Canada, Ottawa, Canada.
8. Stathopoulos, T., "Turbulent Wind Action on Low-Rise Buildings," Thesis presented to the University of Western Ontario, at London, Canada, in 1979, in partial fulfillment of the requirements for the degree of Doctor of Philosophy.
9. Stathopoulos, T., Surry, D., and Davenport, A. G., "A Simplified Model of Wind Pressure Coefficients for Low-Rise Buildings," presented at the 1980 4th Colloquium on Industrial Aerodynamics, held at Aachen, West Germany.
10. Tieleman, H. W., and Reinhold, T. A., "Wind Tunnel Model Investigation for Basic Dwelling Geometries," *VPI-E-76-8*, Virginia Polytechnic Institute and State University, Blacksburg, Va., May, 1976.

APPENDIX II.—NOTATION

The following symbols are used in this paper:

- C_p = pressure coefficient;
 H = eave height;
 p = pressure;
 q_H = dynamic velocity pressure at eave height;
 \bar{V}_H = mean wind speed at eave height;
 V_G = wind speed at gradient height;
 w = eave width;
 α = roof angle; and
 ρ = air density.

SEQUENTIAL GEOMETRIC OPTIMIZATION

By Ovadia E. Lev,¹ M. ASCE

INTRODUCTION

The optimization of nodal coordinates in discrete structures introduces several degrees of complexity above those of optimizing the element proportions with the geometry held fixed. Major contributors to this complexity are: (1) Increased number of decision variables; (2) the different degree of nonlinearity in the numerical behavior of these variables; and (3) the potential change in topology under both fixed and variable geometry optimization. These difficulties prevented the effective utilization of currently available geometric optimization algorithms in design practice. However, designers can no longer afford to neglect this type of optimization; the savings, which result from optimizing the structure configuration, far exceed those obtained assuming the geometry to be fixed.

Various methods were developed by researchers to overcome the difficulties cited above. The majority of these methods are based on alternating optimization in two design subspaces: the sizing variables subspace and the coordinate variables subspace. Refs. (7, 16, 19, 21, 25, 26) are representative works of this type. Pedersen (13) treated sizing and coordinates variables simultaneously, using a restrictive sequence of linear programming (SLP) approach. Most recently, Imai (4) and Schmit adapted the multiplier method (10, 14), also treating all variables simultaneously, and overcame some of the aforementioned numerical difficulties.

While the tools for numerical solution of complex problems, involving buckling, displacement, and geometrical constraints, are available, some drawbacks of optimization, from the designer's point of view, still remain. The process is complex and costly, even with the present decreasing costs of hardware and central processing unit (CPU) time. One of the main reasons for the high cost is the numerous analyses which are usually required in the optimization process. In the preliminary phase of the design process, fast as well as economical optimization is essential for generating initial configuration designs or for improving intuitive, experienced-based designs. For such purposes, simplified processes, yielding approximate solutions, are much needed. This explains the relative success of the stress-ratio method, otherwise known as the fully stressed

¹Mgr., Dept. of Advanced Design and Development, Merritt CASES, Inc., P.O. Box 1206, Redlands, Calif. 92373.

Note.—Discussion open until March 1, 1982. To extend the closing date one month, a written request must be filed with the Manager of Technical and Professional Publications, ASCE. Manuscript was submitted for review for possible publication on February 28, 1980. This paper is part of the Journal of the Structural Division, Proceedings of the American Society of Civil Engineers, ©ASCE, Vol. 107, No. ST10, October, 1981. ISSN 0044-8001/81/0010-1935/\$01.00.

iterative design method, the SLP, and the optimality criterion techniques.

This paper proposes a two-phase sequence of processes addressing the above problems of structural geometry optimization. The method used is heuristic but simple and economically attractive. It is shown that, for a single-loading condition, satisfactory solutions can be obtained by first completing the optimization, considering only constant stress constraints and assuming the geometry to be fixed. This simple process, which usually produces a statically determinate truss, also simplifies the optimization of the nodal coordinates performed in the second phase. If the optimal design under multiple loads is treated as some combination of single-load designs (5,6,12,15,18,22), the final truss can be formed and its optimization refined, using more accurate methods. A similar process was suggested by Dobbs and Felton (1) in 1969. At that time, many of today's sophisticated computer programs and methods were not available to evaluate the accuracy of approximate optimization methods.

GEOMETRIC OPTIMIZATION TECHNIQUES

The nonlinear programming formulation of geometric optimization can be conceptually cast in the following form:

$$\left. \begin{array}{l} \text{minimize } W(A, Q) = \sum \rho L_i A_i \\ \text{subject to } g(A, Q) \geq 0 \end{array} \right\} \dots \dots \dots (1)$$

in which W = the weight of the truss; A and L = the vectors of member cross-sectional areas and lengths, respectively; Q = the vector of nodal coordinates; and ρ = the density of the material. The set of constraint functions, g , are behavioral constraints, such as equilibrium, compatibility and constitutive relations, and side constraints restricting A and Q to vary between specified upper and lower bounds. Ref. (17) is cited here as a representative of works in which Q is assumed to be constant.

As pointed out in the Introduction, it is advantageous in common practice not to optimize all variables simultaneously. This is normally done by performing the optimization in two separate spaces: the sizing space, where A is optimized, assuming the geometry, or Q , to be fixed; and the coordinate space, in which Q is allowed to vary. The process in all these techniques is iterative and continuously alternating between the A and Q subspaces until convergence is reached. The sequence in which the optimization is carried out in the two subspaces differs depending on the techniques used.

It is important to note that while member sizes may be optimized under either fixed or variable geometry, the optimization of geometry must always be accompanied or followed by member proportioning. This necessity is due to changes in the equilibrium equations and member forces resulting from the change in coordinates. Variation of node coordinates is usually based on a search along a certain direction, indicated by the particular gradient approach used. Since several steps, ΔQ , are usually taken along any such direction, a corresponding number of resizing and re-analyses must be performed, requiring tens or hundreds of analyses, which may be quite costly in a sizable problem.

A representative method of geometric optimization is the technique used by Vanderplaats (24). A special-purpose program for trusses, SADT (25), calls a

general-purpose nonlinear optimization program CONMIN (23) whenever the coordinates are modified; thereupon the member proportions are updated and the truss is reanalyzed. Size optimization is performed under fixed geometry using the stress ratio method or a gradient method on the cross-section area reciprocals.

A variation of this method is the process used by Spillers (19), where the geometry is varied in steps, ΔQ , obtained from a set of linearized Kuhn-Tucker optimality criteria. Thus, no search along a direction is involved, and the number of analyses is substantially reduced. However, a trial-and-error process must be performed to find the correct ΔQ whenever the standard values prove to be too large. Because of this problem and because of the internal linearization, the program suffers from numerical instability and quite often stagnates. This (Spillers') program, however, provides the user maximum control and flexibility. The stress ratio method is used to update the member sizes, and it can be performed between geometric iterations in any number or as often as desired.

Lipson and Gwin (8) also used the stress ratio method for optimization in the sizing subspace. Stiffness changes due to displacement constraints are performed using a similar scaling method. By using the complex method (3) in the geometry subspace, the gradient methods are completely avoided at the expense of increased number of analyses.

DIFFERENT SEQUENCES

Within the research program reported in this paper, two different sequences of the two-phase geometric optimization were investigated. In the first sequence, the geometry is varied with no attempts to optimize member sizes. In the second sequence, the optimization in the sizing subspace is first completed using the stress ratio method with fixed geometry and then the coordinates are varied, while adjusting the areas, A , in each iteration until convergence is reached. Vanderplaats' (23,25) and Spillers and Kountouris' (21) programs were used and the results compared to the common continuously alternating phases described in the preceding section. While the sequences investigated both lack the rigor of techniques which consider all variables simultaneously, as in Ref. 4, for example, they do offer some advantages.

The first sequence, which concentrates on the geometry, essentially requires the minimization of $\sum L_i$, the sum of all member lengths. Quite expectedly, because of the gradient methods used in the above programs, no meaningful results were obtained. For this type of problem, general nonlinear programming methods and network theory are more appropriate. These methods were not pursued in this effort; the concept, however, is simple and quite challenging in the case of multiple loadings. In the remaining sections, the second sequence is proposed as a practical expeditious method of geometric optimization. An example is first presented for illustration and discussion. The conclusions drawn subsequently were based on several such examples. The results compared satisfactorily with those obtained by more exact methods.

EXAMPLE 1

Fig. 1(a) shows a given statically, indeterminate truss, the weight of which

was minimized under the given load. Nodes 1 and 4 were constrained to move only in the vertical direction. The results of the optimization using Spillers' and Vanderplaats' programs, discussed in the preceding sections, are shown in Figs. 1(c) and 1(b), respectively. Bars which reached minimal cross sections, but did not totally vanish, are shown in dashed lines. In both cases the initial cross sections were all assumed to be equal, and the geometric optimization began after a few stress ratio iterations without changing the initial geometry. Since most of the members below the main diagonal vanished, the simpler truss shown in Fig. 1(d) was optimized; the results are shown in Figs. 1(e) and 1(f), which correspond to Figs. 1(b) and 1(c), respectively.

Applying the proposed sequence of operations, the given truss in Fig. 1(a) or 1(d) was first optimized using the stress ratio method and holding the geometry

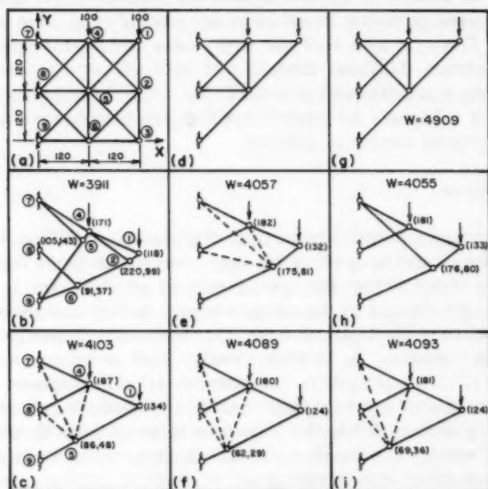


FIG. 1.—Example 1; $E = 30 \times 10^6$ (psi); $\rho = 1$ (lbs/in.³); allowable stress = 22×10^3 (psi); Loads in 10^3 (lbs); numbers in parentheses indicate coordinate values (inches); W = weight (lbs)

fixed. This resulted in the truss shown in Fig. 1(g). This truss is fully stressed and will be shown later to be a combination of two statically determinate configurations. Optimization of the geometry of the truss in Fig. 1(g) yielded the trusses in Figs. 1(h) and 1(i), which correspond to Figs. 1(b)–1(f), respectively. Note that in all cases the final locations of the loaded nodes are almost identical, while all other nodes are “floating.” Furthermore, if the kinks between nodes 1 and 9 and nodes 4 and 9 were straightened, several other members would have vanished, and the true theoretical optimum, discussed in the next section, would have been reached.

TOPOLOGICAL CONSIDERATIONS

Optimizing the topology, or the connectivity of a skeletal structure, has been and still is a major stumbling block of structural optimization. While methods for mixed-integer programming have been developed, the subject is still too complex for practical engineering applications. Two widely used methods of topological optimization are linear programming (2,11,20) and iterative stress ratio design (20). Using these methods, a set of redundants is eliminated from a larger admissible set of bars connecting all admissible nodes. Most known geometric optimization programs, however, assume the topology of the structure to be fixed; some do not even allow for vanishing cross sections. Such programs may be quite useful for optimizing a known topology. In preliminary design the configuration problem (geometry and topology) is critical. In this section, the role of statically determinate topologies is discussed as a potential, heuristic basis for determining truss configurations.

Weight minimization of stress-constrained trusses, under a single loading condition and fixed geometry, usually results in a statically determinate configuration. In linear programming terminology, such a configuration corresponds to a basic feasible solution. If more than one such solution is optimal, a fully stressed indeterminate truss of equivalent weight may result (20). It follows that if, hypothetically, all determinate topologies are exhaustively searched, at least one of them will lead to the optimal topology and geometry of the minimum weight truss.

EXAMPLE 2

Figs. 2(a), 2(b), and 2(c) show three of the determinate topologies of the truss shown in Fig. 1(d). The results of geometric optimization of these trusses are shown in Figs. 2(d), 2(e), and 2(f), respectively. These configurations should be compared to those of Fig. 1 and to the theoretical optima in Figs. 2(g), 2(h), and 2(i). It should be remarked that the fully stressed indeterminate solution, obtained by the stress ratio iterative method, shown in Fig. 1(g), is a combination of and has equal weight to the two optimal determinate trusses of Figs. 2(a) and 2(c). Furthermore, only one of these two trusses, the one shown in Fig. 2(c), leads to the global optimum shown in Figs. 2(h) and 2(i).

Note in particular, that the solution obtained using Vanderplaats' program, shown in Fig. 1(b), approaches the global solution in Fig. 2(h) while the solution in Fig. 1(c) obtained using Spillers' program approaches the local optimum shown in Fig. 2(g).

It is evident from the preceding example(s) that the initial topology and the method of optimization bear quite heavily on the optimum solution. It is also significant, however, that the coordinates of the loaded nodes converge in all cases to the true optimum, which suggests that this optimum is unique, for the given loading and with constant stress constraints. Heuristically, if this uniqueness is tentatively assumed, the optimal coordinates of the loaded nodes may be obtained by optimizing the geometry of any statically determinate set of members connecting these nodes to the supports. The topology may then be handled in a second phase.

The rigorous mathematical uniqueness proof of optimal node coordinates even

under a single loading condition is complex and challenging. Michell (9) in 1904 handled a closely related problem. He showed that the quantity, C , in the equalities

$$\sum F_i L_i = \sum P_j Q_j = C \quad (2)$$

in which F_i = the force in member, i , is constant for determinate fixed-geometry configurations and depends only on the loads, P (including the reactions), and the coordinates of their points of application. Consider Michell's expression

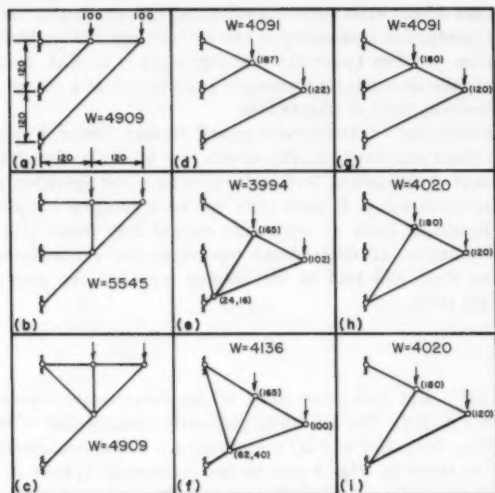


FIG. 2.—Example 2; $\rho = 1$ (lbs/in.³); allowable stress = 22×10^3 (psi); loads in 10^3 (lbs); Numbers in parentheses indicate coordinate values (in.); W = weight (lbs)

for the material volume, V , of a fully stressed truss

$$V = \alpha Z + \beta C \quad (3)$$

in which α and β = material constants; and

$$Z = \sum |F_i| L_i \quad (4)$$

For minimum V under fixed geometry, Michell's showed that it is sufficient to minimize Z since in this case C is constant. If the geometry is allowed to vary, the contributions of both Z and C to the volume must be further minimized. Thus, if the weight reaches a minimum with the geometry fixed, further reduction may be obtained by varying the "potential" function, C , i.e., by varying the coordinates. These notions are discussed in more detail in Ref. (7).

APPLICATIONS

Theoretically, only if $W(A, Q)$ is convex and continuous, is there hope for reaching a global minimum, regardless of the optimization sequence. In problems with buckling constraints, the feasible design space may be disjoint, as demonstrated by Imai and Schmit (4), so that the general problem is nonconvex. For many problems in practice, however, convexity can be assumed and advantageous sequences followed. The tremendous economy of fixed-geometry optimization, followed by geometric optimization of statically determinate trusses, makes the proposed two-phase sequence very attractive, compared with the commonly used alternating sequence. The number of analyses is substantially reduced. The solution may be subsequently modified using an exact method in a limited number of additional analyses including other constraints such as Euler buckling and allowable displacements. This, of course, assumes that the approximate and the exact solutions do not differ fundamentally.

As shown in Figs. 1(b) and 1(c), the results of the iterative optimization process, continuously alternating between the coordinate and area design subspaces may yield ambiguous results because of the topology. In large structures, this could be misleading. In optimizing determinate configurations, this deficiency is improved, and an experienced designer can extrapolate the final results and exercise judgement in providing redundancy and buckling resistance to the structure.

It should be pointed out that, in this paper, only a single-loading condition is considered. Multiple loadings, however, can be treated as combinations of single loadings (12,15,18,22). The stress-ratio method or programming procedures can, in such cases, be also effectively used in the fixed geometry phase. The problem of combining optimal geometries in the case of two-loading conditions has been treated (6,12). However, a methodology for the general case needs still to be developed.

CONCLUSIONS

A two-phase sequence of optimization is proposed as a heuristic method for optimizing truss configurations in preliminary design. In the first phase, an optimal determinate configuration is obtained with the initial geometry held fixed. In the second phase, the geometry is optimized. The advantages of this method lie in the substantial reduction in the number of analyses and the control it offers the designer. It is also suggested that through the proposed technique there may be obtained a reasonable initial geometry that allows one subsequently to optimize the topology.

ACKNOWLEDGMENT

This research was supported by the National Science Foundation under Grant No. PFR 78-04313 to Merritt CASES, Inc.

APPENDIX I.—REFERENCES

1. Dobbs, M. W., and Felton, L. P., "Optimization of Truss Geometry," *Journal of*

- Structural Division*, ASCE, Vol. 95 No. ST10, Oct., 1969, pp. 2105-2118.
2. Dorn, W. S., Gomory, R. E., and Greenberg, H. J., "Automatic Design of Optimal Structures," *Journal of Mechanics*, Vol. 3, Mar., 1964, pp. 25-52.
 3. Ghani, S. N., "An Improved Complex Method of Functional Minimization," *Computer Aided Design*, Jan., 1972, pp. 71-78.
 4. Imai, K., and Schmit, L. A., Jr., "Configuration Optimization of Trusses," *Journal of the Structural Division*, ASCE, Vol. 107, No. ST5, Proc. Paper 16251, May, 1981, pp. 745-756.
 5. Lev, O. E., "Optimum Choice of Determinate Trusses Under Multiple Loads," *Journal of the Structural Division*, ASCE, Vol. 103, No. ST2, Proc. Paper 12739, Feb., 1977, pp. 391-403.
 6. Lev, O. E., "Optimum Truss Geometry for Two Loading Conditions," *Journal of the Structural Division*, ASCE, Vol. 104, No. ST8, Proc. Paper 13953, Aug., 1978, pp. 1203-1210.
 7. Lev, O. E., "Topology and Optimality of Certain Trusses," *Journal of the Structural Division*, ASCE, Vol. 107, No. ST2, Proc. Paper 16054, Feb., 1981, pp. 383-393.
 8. Lipson, S. L., and Gwin, L. B., "The Complex Method Applied to Optimal Truss Configuration," *Computers and Structures*, Vol. 7, 1977, pp. 461-468.
 9. Michell, A. G. M., "The Limits of Economy of Material in Frame Structures," *Philosophical Magazine*, S6, Vol. 8, No. 47, Nov., 1904, pp. 589-595.
 10. Miele, A., Moseley, P. E., Levy, A. V., and Goggins, G. M., "On the Method of Multipliers for Mathematical Programming Problems," *Journal of Optimization Theory and Applications*, Vol. 10, No. 1, Jan., 1972.
 11. Moses, F., "Optimum Structural Design Using Linear Programming," *Journal of the Structural Division*, ASCE, Vol. 90, No. ST6, Dec., 1964, pp. 89-104.
 12. Nagtegaal, J. C., and Prager, W., "Optimal Layout of a Truss for Alternative Loads," *International Journal of the Mechanical Sciences*, Vol. 15, 1973, pp. 583-592.
 13. Pedersen, P., "Optimum Joint Positions for Space Trusses," *Journal of Structural Division*, ASCE, Vol. 99, No. ST12, Dec., 1973, pp. 2459-2475.
 14. Rockafellar, R. T., "The Multiplier Method of Hestenes and Powell Applied to Convex Programming," *Journal of Optimization Theory and Application*, Vol. 12, No. 6, 1973, pp. 555-562.
 15. Rozvany, G. I. N., and Hill, R., "Optimal Plastic Design: Superposition Principles and Bounds on Minimum Cost," *Computer Methods in Applied Mechanical Engineering*, Vol. 19, No. 1, 1979.
 16. Schmit, L. A., and Mallett, R. H., "Structural Synthesis and Design Parameter Hierarchy," *Journal of Structural Division*, ASCE, Vol. 89, No. ST4, Aug., 1963, pp. 269-299.
 17. Sheu, C. Y., and Schmit, L. A., Jr., "Minimum Weight Design of Elastic Redundant Trusses under Multiple Static Loading Conditions," *AIAA Journal*, Vol. 10, No. 2, Feb., 1972, pp. 155-162.
 18. Spillers, W. R., "A Note on the Decomposition of an Absolute-Value Linear Programming Problem," *Quarterly of Applied Mathematics*, Vol. 29, No. 4, Jan., 1972, pp. 541-544.
 19. Spillers, W. R., "Iterative Design for Optimal Geometry," *Journal of Structural Division*, ASCE, Vol. 101, No. ST7, July, 1975, pp. 1435-1442.
 20. Spillers, W. R., *Iterative Structural Design*, North-Holland Publishing Company, Amsterdam, The Netherlands, 1975.
 21. Spillers, W. R., and Kountouris, G. E., "Shape Optimization," presented at the ASCE Convention, Pittsburgh, Pa., Apr., 24-28, 1978.
 22. Spillers, W. R., and Lev, O. E., "Design for Two Loading Conditions," *International Journal Solids Structures*, Vol. 7, 1971, pp. 1261-1267.
 23. Vanderplaats, G. N., "CONMIN—A FORTRAN Program for Constrained Function Minimization, User Manual," *Technical Memorandum TMX-62,282*, National Aeronautics and Space Administration, Aug., 1973.
 24. Vanderplaats, G. N., "Design of Structures for Optimum Geometry," *Technical Memorandum TM-X-62,462*, National Aeronautics and Space Administration, Aug., 1975.
 25. Vanderplaats, G. N., "SADT" (Structural Analysis and Design of Trusses), a computer program developed at NASA Ames Research Center, Moffet Field, Calif., Mar., 1979.

26. Vanderplaats, G. N., and Moses, F., "Automated Design of Trusses for Optimum Geometry," *Journal of Structural Division*, ASCE, Vol. 98, No. ST3, Mar., 1972, pp. 671-690.

APPENDIX II.—NOTATION

The following symbols are used in this paper:

- A = member cross-sectional area vector;
- C = defined in text, Eq. 2;
- F = member force vector;
- g = constraint functions;
- i = member subscript;
- j = node or load subscript;
- L = member length vector;
- P = load vector;
- Q = coordinates vector;
- V = volume of truss material;
- W = weight of truss material;
- Z = defined in text, Eq. 4;
- α = material constant;
- β = material constant; and
- ρ = material density.

CYCLIC SHEAR TRANSFER AND TYPE OF INTERFACE^a

By Alan H. Mattock,¹ F. ASCE

INTRODUCTION

In the 1960's Birkeland and Birkeland (1) and Mast (4) developed a philosophy of connection design in which cracks are assumed to have occurred at disadvantageous locations within the region of the connection. Reinforcement is then designed to transfer shear, normal force and moment across these cracks when the connection is loaded. No dependence is placed on the tensile strength of the concrete. They proposed that the reinforcement needed to transfer shear across the cracks be designed using the "Shear-Friction" method of design.

Provisions for the shear transfer reinforcement design using the shear-friction method were subsequently included in the American Concrete Institute, (ACI), Building Code (2). These provisions were based on the test data obtained in monotonic loading tests of specimens made from normal weight natural aggregates. Subsequent tests (7) showed that the shear transfer strength of lightweight concrete under monotonic load is inferior to that of normal weight concrete of the same compressive strength. It was, therefore, proposed (7) that the shear transfer strengths of all-lightweight concrete and of sand-lightweight concrete be taken, respectively, as 0.75 and 0.85 times the shear transfer strength of normal weight concrete of the same compressive strength and having the same reinforcement.

Although the applicability of the ACI Code shear friction provisions to cyclic reversal of loads in earthquakes had not been verified experimentally, use has been made of these provisions in seismic design. An example of this was the extensive use of the shear-friction concept in the 1971 Prestressed Concrete Institute (PCI) *Design Handbook* (9).

This paper reports a study of the influence on cyclic shear transfer behavior of aggregate type and of type of interface, i.e., a crack in monolithic concrete or an interface between concrete cast at different times. The primary purpose of the study was to determine how shear transfer strength equations based on monotonic loading tests should be modified when they are used in the design of connections subject to seismic loading.

^aPresented at the April 14-18, 1980, ASCE Convention and Exposition, held at Portland, Oreg.

¹Prof. of Civ. Engrg., Univ. of Washington, Seattle, Wash.

Note.—Discussion open until March 1, 1982. To extend the closing date one month, a written request must be filed with the Manager of Technical and Professional Publications, ASCE. Manuscript was submitted for review for possible publication on July 24, 1980. This paper is part of the Journal of the Structural Division, Proceedings of the American Society of Civil Engineers, ©ASCE, Vol. 107, No. ST10, October, 1981. ISSN 0044-8001/81/0010-1945/\$01.00.

EXPERIMENTAL STUDY

Scope.—Shear transfer tests of 11 pairs of specimens are reported. One specimen of each pair was loaded monotonically to failure while the other was subjected to incrementally increasing, cyclically reversing shear.

TABLE 1.—Program of Tests

Series (1)	Type of specimen (2)	Type of concrete (3)	Bond condition of interface (4)	Initial condition (5)
MN	monolithic	normal weight	—	cracked
ML	monolithic	light weight	—	cracked
CB	composite	normal weight	bonded	cracked
CNB	composite	normal weight	bond broken	uncracked

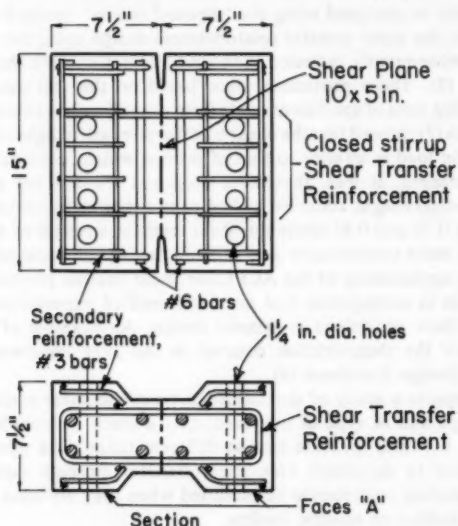


FIG. 1.—Typical Specimen (1 in. = 25.4 mm)

In addition to the type of loading, the variables included in the tests were: (1) Type of specimen, i.e., monolithic, or composite with the interface in the shear plane; (2) type of concrete, normal weight or lightweight; (3) condition of the interface in the composite specimens, either bonded and initially cracked, or without bond and not subject to the initial cracking process before the shear test; and (4) the amount and strength of the reinforcement crossing the shear

plane. The program of tests is set out in Table 1.

Test Specimens.—Details of a typical specimen are shown in Fig. 1. It is designed to be gripped by friction on faces "A" as shown in Fig. 2. The 50 in.² (32,260 mm²) shear plane is subject to shear without moment.

The shear transfer reinforcement was in the form of closed stirrups, which wrapped around longitudinal reinforcement so as to ensure positive anchorage on both sides of the shear plane. Additional reinforcement was provided to prevent failure of the specimen away from the shear plane (Fig. 1).

The composite specimens were cast in two stages, the interface between the two concretes lying in the shear plane. The first cast part of these specimens

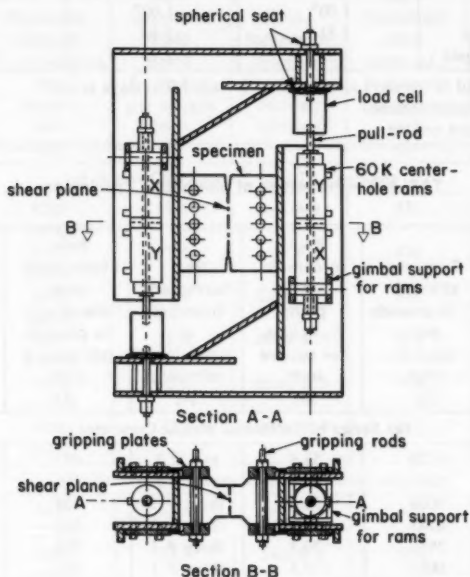


FIG. 2.—Arrangements for Test

was three days old when the second part was cast. The interface was deliberately roughened to an amplitude of 1/4 in. (6 mm) to conform to the requirements of the ACI Code (2). In Series CB specimens, an effort was made to obtain good bond between the two concretes by cleaning and wetting the first cast concrete surface. In series CNB specimens the interface was coated with a bond breaker of soft soap and talc before the second concrete was cast to prevent bond at the interface.

The concrete mix proportions are shown in Table 2. The normal weight concrete specimens were tested at age seven days, or seven days after casting the first concrete. They were cured in the forms under polythene sheets, until the time of test. The lightweight concrete specimens were moist-cured for seven days

and were tested at age 28 days, after a further 21 days curing in the air of the laboratory. (This curing procedure has been standardized for studies of lightweight concrete so that the degree of drying out of the concrete shall be consistent.)

TABLE 2.—Concrete Mix Proportions

Material (1)	Normal Weight Concrete ^a		Lightweight concrete (4)
	Mix "A" (2)	Mix "B" (3)	
Cement	1.00 ^b	1.00 ^b	1.00 ^c
Fine aggregate	1.81	1.63	2.10
Coarse aggregate	2.52	2.15	1.48

^aMix "A" aged seven days at test; Mix "B" aged four days at test.

^bType III portland cement.

^cType I portland cement.

TABLE 3.—Properties of Monolithic Specimens

Specimen number (1)	Concrete strength f'_c , in pounds per square inch (2)	Rein- forcement yield point f_y , in kips per square inch (3)	Rein- forcement (number of two leg stirrups) (4)	Rein- forcement para- meter ρf_y , in pounds per square inch (5)	V_s (calc.), in kips (6)
(a) Series MN (Normal Weight Concrete)					
MN2M	6120	53.6	two # 3	472	38.9
MN2C	6000	53.0	two # 3	466	38.6
MN3M	6000	53.6	three # 3	708	48.3
MN3C	6145	52.2	three # 3	689	47.6
MN4M	5950	70.3	three # 3	928	57.1
MN4C	6016	70.5	three # 3	931	57.2
(b) Series ML (Lightweight Concrete) ^a					
ML1M	4140	66.0	three # 2	396	25.8
ML1C	4140	66.0	three # 2	396	25.8
ML2M	4025	49.3	two # 3	434	27.4
ML2C	3825	51.8	two # 3	456	28.2
ML3M	4240	51.4	three # 3	678	37.1
ML3C	4240	52.0	three # 3	686	37.4

^a Average dry density 95 lb/ft³ (1,522 kg/m³)

Note: 1 psi = 6.89 kPa; 1 ksi = 6,890 kPa; 1 kip = 4.45 kN.

The normal weight concrete was made from a glacial outwash gravel of 5/8 in. (16 mm) maximum size. The lightweight concrete was made from a "coated" aggregate (Materialite) of 1/2 in. (13 mm) maximum size.

The properties of the monolithic and composite specimens are shown in Tables 3 and 4, respectively.

Testing Arrangements.—The specimens were tested in the specially constructed two-part frame shown in Fig. 2. Opposite sides of the specimen were attached to the two parts of the frame by gripping plates. The clamping force was provided by post-tensioned high strength steel rods passing through the plates and through oversize holes in the specimen. Two soft rubber O-rings were used to center

TABLE 4.—Properties of Composite Specimens

Specimen number (1)	Concrete strength f'_c , in pounds per square inch (2)	Reinforcement yield point f_y , in kips per square inch (3)	Reinforcement number of two leg stirrups (4)	Reinforcement parameter ρf_y , in pounds per square inch (5)	V_u (calc.), in kips (6)
(a) Series CB (Bonded, Initially Cracked)					
CB2M	6200 (5760)	53.4	two # 3	470	38.8
CB2C	6115 (5770)	53.4	two # 3	470	38.8
CB3M	6100 (6260)	51.4	three # 3	678	47.1
CB3C	6030 (5970)	52.6	three # 3	694	47.8
CB4M	6050 (5970)	72.4	three # 3	956	58.2
CB4C	5990 (5910)	72.1	three # 3	952	58.1
(b) Series CNB (Bond Broken, Uncracked)					
CNB2M	6120 (6120)	53.8	two # 3	473	38.9
CNB2C	6160 (6120)	53.9	two # 3	474	39.0
CNB3M	5750 (6170)	53.2	three # 3	702	48.1
CNB3C	6220 (5820)	53.5	three # 3	706	48.2

Note: 1 psi = 6.89 kPa; 1 ksi = 6,890 kPa; 1 kip = 4.45 kN.

the rods in the oversize holes to prevent the rods from bearing directly on the concrete.

The shearing forces were provided by the diagonally opposed pairs of 60 kip (266,880 N) capacity hydraulic center hole rams *X* and *Y* in Fig. 2. The loads were applied through load cells so that the applied shear could be monitored continuously. Each linear assembly of rams, pull rods, and load cell was attached to both parts of the frame by a spherical bearing at one end and a gimbal

at the other. This allowed the two parts of the frame to articulate as the specimen deformed under load, and prevented the frame from restraining the deformation of the specimen. Oil pressure was supplied to the rams through a four-way valve, by a Riehle "Pendomatic" pumping and measuring unit.

Both the slip, (or relative motion parallel to the shear plane of the two halves of the specimen), and separation, (or relative motion normal to the shear plane of the two halves of the specimen), were measured continuously using linear differential transformers as the sensing elements of slip and separation gages attached to reference points embedded in the face of the specimen.

TESTING PROCEDURES

Initial Cracking.—All the specimens except those of Series CNB were cracked in the shear plane before being subject to shear loading. The crack was produced by applying line loads to the back and front faces of the specimen along the line of the shear plane. The dilation of the specimen normal to the shear plane was measured during the cracking operation, using dial gages attached to a reference frame surrounding the specimen. Loading was continued until an average dilation of 0.013 in. (0.33 mm) was obtained. When the line loads were removed, a residual dilation of close to 0.01 in. (0.25 mm) remained. This was the average initial width of crack in the shear plane before shear was applied to the specimens.

Shear Loading.—Those specimens having specimen numbers ending in M were subjected to monotonically increasing shear until failure. Failure was considered to have occurred when the shear could not be increased further and both slip and separation increased rapidly.

Those specimens having specimen numbers ending in C were subjected to the following program of cyclic loading. The shear was first continuously increased to 50% of the calculated shear strength $V_u(\text{calc.})$ under monotonic loading, after which it was reduced to zero. Shear of opposite sign was then applied to the specimen, again being increased to 50% of the calculated shear transfer strength, before being reduced to zero to complete the first cycle of loading. Each specimen was subject to 10 such cycles of loading. The maximum positive and negative shears were then increased by 8% of the calculated shear strength, i.e., to $\pm 58\%$ of $V_u(\text{calc.})$ for the next five loading cycles. After each succeeding five cycles of load the maximum shears were increased by the same amount. This process was continued until failure of the specimen occurred. Failure was considered to have occurred when the shear could not be increased to the planned maximum shear for that cycle.

In calculating $V_u(\text{calc.})$, ACI strength reduction factor ϕ was taken as 1.0, since material strengths and specimen dimensions were known accurately.

$V_u(\text{calc.})$ was based on the following equations previously proposed (6,7):

For normal weight concrete

$$V_u(\text{calc.}) = (0.8\rho_f + 400)A_c \text{ lb} \quad [V_u(\text{calc.}) = (0.8\rho_f + 2.76)A_c \text{ N}] \quad \dots \dots (1)$$

but not more than $0.3f'_c A_c$

For all lightweight concrete

$$V_u(\text{calc.}) = (0.8\rho_f + 200)A_c \text{ lb} \quad [V_u(\text{calc.}) = (0.8\rho_f + 1.38)A_c \text{ N}] \quad \dots \dots (2)$$

but not more than $0.2f'_c A_c$ nor $800 A_c \text{ lb}$ ($5.52 A_c \text{ N}$).

in which $\rho = A_{vf}/A_c$; A_{vf} = total area of shear transfer reinforcement crossing the shear plane, in.^2 (mm^2); A_c = area of shear plane, in.^2 (mm^2); f_y = yield strength of shear transfer reinforcement, psi (kPa).

SPECIMEN BEHAVIOR

Monotonic Loading Tests.—Behavior under monotonically increasing load was essentially similar for all specimens. Slip occurred along the preformed crack from the commencement of loading, at a progressively increasing rate, as may

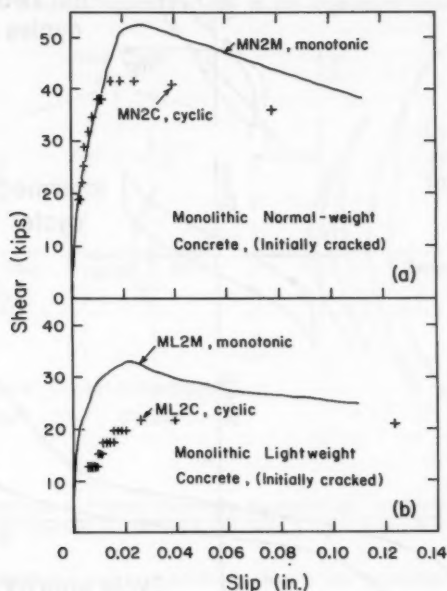


FIG. 3.—Typical Shear-Slip Curves for Cyclic Loading

be seen in Fig. 3. The slip along the crack was accompanied by separation across the crack. In general, the separation was much smaller in lightweight concrete specimens than in normal weight concrete specimens.

Diagonal tension cracks occurred adjacent to the shear plane in all specimens, more cracks occurring in the more heavily reinforced specimens. In the monolithic specimens and in the bonded composite specimens, these cracks were uniformly distributed along the shear plane. In the composite specimens in which the bond at the interface was deliberately broken, the cracks tended to concentrate in the vicinity of the shear transfer reinforcement. In these specimens also, a few cracks perpendicular to the shear plane occurred near failure, at the

locations of the shear transfer reinforcement.

At failure, both slip and separation increased rapidly and a slight amount of spalling occurred adjacent to the shear plane in most specimens. The spalling was most pronounced in the specimens in which the bond at the interface was broken. In these specimens the spalling occurred primarily in the vicinity of the shear transfer reinforcement.

Cyclic Loading Tests.—In these tests, the response of the specimens changed as the number of cycles of loading and the level of loading increased. This

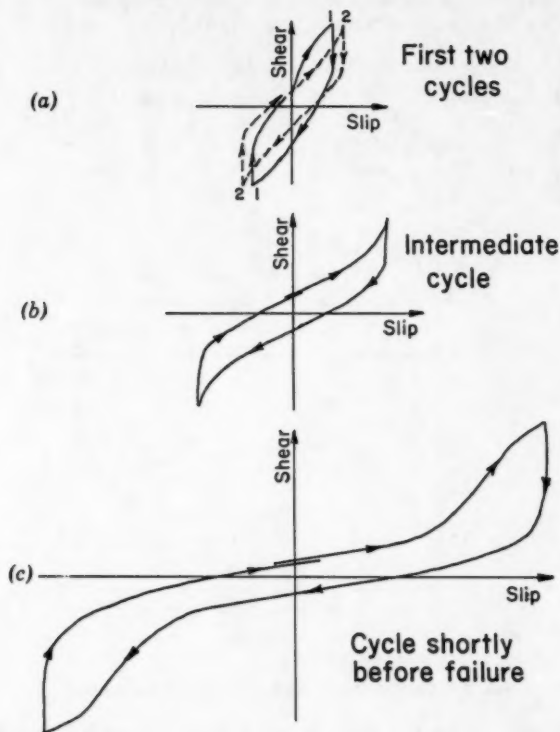


FIG. 4.—Typical Slip-Separation Curves for Cyclic Loading

is illustrated in Figs. 4 and 5, which show typical shear-slip and slip-separation curves at different stages of loading, for both the monolithic and composite specimens.

The separation values are the change in separation due to application of the shear. To obtain the total separation, the initial crack width or the width of any gap at the interface due to use of the bond breaking agent must be added.

Response to the first cycle of loading is characterized by a gradual reduction in shear stiffness as the shear is increased in both positive and negative directions and by retention of almost all of the slip caused by the maximum shear until the shear reduces to about half its maximum value Fig. 4(a).

Response to succeeding cycles of loading is characterized by a low shear stiffness at low values and a gradual increase in shear stiffness with increase in shear in both positive and negative directions. As the number of load cycles increases, the shear stiffness at low shears decreases and the increase in stiffness with increase in shear becomes greater. This causes the shear-slip curve for a complete loading cycle to assume a progressively more pinched appearance as the number of loading cycles increases. This was particularly marked in the lightweight concrete specimens and in the composite specimens without

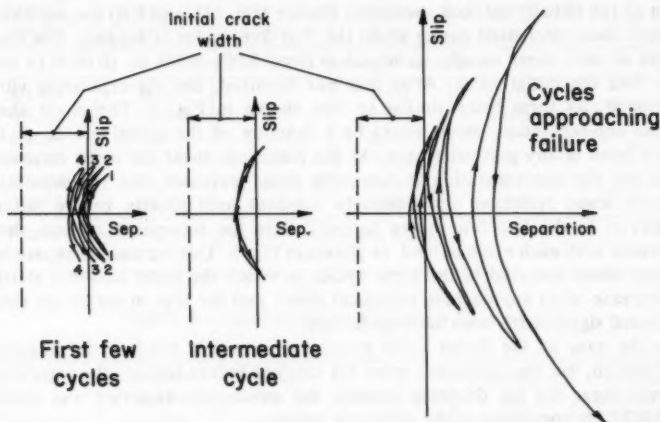


FIG. 5.—Comparison of Typical Shear-Slip Relationships for Cyclic and Monotonic Loading; Initially Cracked Monolithic Specimens (1 kip = 4,450 N; 1 in. = 25.4 mm)

bond at the interface, and was probably due to the smoother crack faces in these specimens.

The slip at maximum shear increased slightly each cycle, for about the first five cycles. Thereafter, for the normal weight monolithic and bonded composite specimens, the specimens responded in a stable manner Fig. 4(b).

For maximum shears of $\pm 0.5 V_u$ (calc.) the maximum slip was about ± 0.007 in. (0.18 mm) for the monolithic specimens and for the bonded composite specimens, and was about ± 0.015 in. (0.38 mm) for the composite specimens without bond at the interface.

The slip at maximum shear and the shape of the shear-slip curve remained essentially the same for a given maximum shear, until the maximum shear reached about 90% of the load at which failure occurred. At and above this load, the slip at maximum shear increased with each cycle, and by progressively increasing amounts. The characteristic shape of the shear-slip curve also changed, in that

after increasing as the shear increased, the shear stiffness then decreased again as the maximum shear was approached (Fig. 4). Failure occurred when the shear stiffness under increasing load reduced to zero, after which slip increased rapidly even though the load was decreasing.

In the case of the lightweight concrete specimens and the composite specimens without bond at the interface, the slip at maximum shear increased by varying amounts in all load cycles.

The shear-slip curves were in general approximately symmetrical about both the shear and slip axes. However, in some cases more slip occurred at maximum load due to shear acting in one direction rather than in the other. This was presumably due to the crack faces having an irregular profile. The general shape of the shear-slip curve was unaltered, but the relative motion of the two halves of the specimen became centered on a position different from the starting position.

In all the initially cracked specimens (Series MN, ML and CB) the separation at zero shear decreased during about the first five cycles of loading. The crack width at zero shear usually stabilized at from 0.003–0.005 in. (0.08–0.13 mm) less than the initial value. After this had occurred, the slip-separation curve stabilized, its form being similar to that shown in Fig. 5. The exact shape of the slip-separation curve would be a function of the actual profile of the crack faces in any particular case. As the maximum shear per cycle increases, both the slip and separation at maximum shear increased, but the separation at zero shear remained approximately constant until shortly before failure. However, in the last few cycles before failure the separation at zero shear increased with each cycle of load, as shown in Fig. 5. This increase in separation at zero shear occurred in the same cycles in which the shear stiffness started to decrease when approaching maximum shear, and the slips at maximum shear increased significantly with each cycle load.

In the case of the Series CNB specimens in which bond at the interface was broken, but the specimens were not cracked before testing, the separation at zero shear did not decrease initially, but subsequent behavior was similar to that of the specimens in the other test series.

Diagonal tension cracks occurred in all specimens subjected to cyclic loading. Two sets of cracks occurred, both inclined at 45° to the shear plane, and at right angles to one another. The two sets of cracks opened and closed alternately, as the direction of the shear was reversed. Until close to failure, the cracks were almost invisible at zero shear. They were fairly uniformly distributed along the shear plane in the case of the monolithic specimens and the composite specimens in which the bond at the interface was not broken. In the case of those specimens in which the bond at the interface was broken, the diagonal tension cracks tended to concentrate in the vicinity of the shear transfer reinforcement. In these specimens a few cracks also occurred perpendicular to the shear plane aligned with the shear transfer reinforcement.

At failure, one set of diagonal tension cracks widened and compression spalling of the concrete occurred adjacent to the shear plane. This spalling was more extensive than in the case of the specimens subjected to monotonic loading. Specimen failure was characterized by both slip and separation increasing rapidly, with the load carried by the specimen either held constant or decreasing.

Failure Data.—In Tables 5 and 6 the following data are given for each specimen tested: (1) Ultimate shear transfer strength; (2) number of cycles of load to

TABLE 5.—Test Results for Monolithic Specimens

Specimen number (1)	Ultimate shear strength, in kips (2)	Number of cycles to failure (3)	Slip at failure, in inches (4)	Separation at failure, ^a in inches (5)	(Cyclic strength) (monotonic strength) (6)
(a) Series MN (Normal Weight Concrete)					
MN2M	52.7	—	0.028	0.032	0.79
MN2C	41.7	44	0.032	0.054	
MN3M	66.1	—	0.026	0.034	
MN3C	56.0	47	0.033	0.026	0.85
MN4M	81.5	—	0.038	0.016	
MN4C	65.3	51	0.054	0.053	0.80
(b) Series ML (Lightweight Concrete)					
ML1M	26.3	—	0.031	0.005	0.88
ML1C	23.0	32	0.027	0.003	
ML2M	33.0	—	0.023	0.005	
ML2C	21.7	28	0.046	0.005	0.66
ML3M	48.0	—	0.023	0.011	
ML3C	38.2	42	0.031	0.007	0.80

^aValues of separation do not include initial crack width.

Note: 1 kip = 4.45 kN; 1 in. = 25.5 mm.

TABLE 6.—Test Results for Composite Specimens

Specimen number (1)	Ultimate shear strength, in kips (2)	Number of cycles to failure (3)	Slip at failure, in inches (4)	Separation at failure, ^a in inches (5)	(Cyclic strength) (monolithic strength) (6)
(a) Series CB (Bonded, Initially Cracked)					
CB2M	50.0	—	0.035	0.026	0.88
CB2C	44.2	46	0.030	0.007	
CB3M	59.2	—	0.017	0.010	
CB3C	54.5	47	0.022	0.038	0.92
CB4M	79.2	—	0.015	0.026	
CB4C	61.6	44	0.022	0.015	0.78
(b) Series CNB (Bond Broken, Uncracked)					
CNB2M	42.6	—	0.025	0.014	0.60
CNB2C	25.7	20	0.066	0.028	
CNB3M	60.9	—	0.021	0.022	0.59
CNB3C	35.7	21	0.030	0.030	

^aValues of separation do not include initial crack width.

Note: 1 kip = 4.45 kN; 1 in. = 25.5 mm.

which specimen was subjected; (3) slip and separation at ultimate shear; and (4) ratio of ultimate strength of specimen subject to cyclic loading to that of companion specimen subject to monotonic loading.

The ultimate shear is defined as the maximum shear carried by the specimen during the test. In a cyclic loading test this may be either the maximum shear to which the specimen has been cycled, or the maximum shear reached when the maximum shear was being increased at the end of a group of cycles of loading to a constant maximum shear.

For cyclic loading, the values of slip and separation at failure listed in Table 5 are the averages of the values measured at the maximum positive and negative shears in the last complete load cycle before failure.

TEST RESULTS

To facilitate the subsequent analyses of specimen behavior, the ways in which shear transfer resistance can be developed in a cracked shear plane, will first be identified.

1. By friction between the faces of the crack caused by the tension force developed in the reinforcement crossing the crack, as a result of separation of the rough crack faces when slip occurs.
2. By direct bearing of small asperities projecting from the faces of the crack.
3. By dowel action of the reinforcement crossing the crack; i.e. direct resistance of the bars to shearing action at the crack.

Behavior of Monotonically Loaded Specimens.—At low values of applied shear, the shear stiffness is very high and little or no separation occurs. This indicates that at this stage, most of the shear resistance comes from the direct bearing of asperities on the faces of the crack. With little or no separation occurring, the reinforcement crossing the crack is not stretched significantly. Consequently little or no compression exists across the crack and hence no significant frictional resistance to shear can be developed. Also, with near zero slip between the crack faces, shear resistance due to dowel action will be very small.

As the applied shear is increased, increasing numbers of the asperities are crushed and the intensity of bearing pressure on the remaining asperities increases more rapidly than the applied shear. Deformations, therefore, increase more rapidly, i.e., the shear stiffness decreases.

As slip and separation increase, an increasing amount of shear resistance will be provided by dowel action and by friction between the crack faces. However, at shears approaching ultimate, the tensile stress in the reinforcement will approach its yield point, if secondary failure of the concrete near the shear plane is prevented. The "dowel action" contribution to shear resistance will consequently reduce, and, at failure, it is believed that almost all the shear resistance will derive from direct bearing of asperities on the crack faces and friction between the crack faces due to the large tensile force developed in the reinforcement. The proportion of shear resisted by friction will increase as the total yield strength $A_v f_y$ of the reinforcement increases.

Dowel action probably contributes little to shear transfer strength when the yield strength of the shear transfer reinforcement is developed. This hypothesis

is supported by the following: when an external compression force is applied to a shear plane, the shear transfer strength is increased by the same amount as would result from providing additional reinforcement with a yield strength equal to the external compression force (5). If significant dowel action occurred after bar yielding one would expect a greater increase in shear strength from provision of the extra reinforcement than from the action of the equivalent compression force.

Because of the difference in concrete compressive strengths, the behavior and strengths of the normal-weight concrete and lightweight concrete monolithic

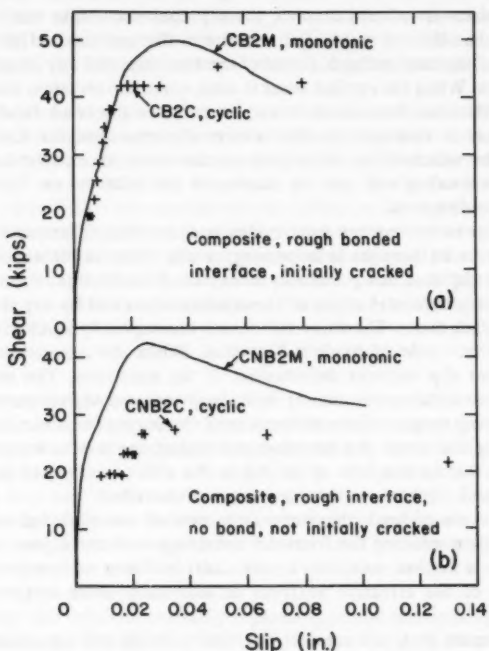


FIG. 6.—Comparison of Typical Shear-Slip Relationships for Cyclic and Monotonic Loading; Composite Specimens (1 kip = 4,450 N; 1 in. = 25.4 mm)

specimens cannot be directly compared. The behavior of the lightweight concrete specimens under monotonic loading was, however, generally similar to that previously reported (7).

In Figs. 3 and 6, and Tables 5 and 6, it can be seen that under monotonic loading the behavior and strength of the initially cracked composite specimens with good bond at the interface (Series CB), was very similar to that of the initially cracked, monolithic normal-weight concrete specimens (Series MN). This is in agreement with previous tests (8).

In earlier monotonic loading tests (8) of composite specimens in which bond at the interface was prevented, behavior and strength were found to be similar to that of comparable initially cracked, bonded composite specimens. In the current study, the behavior of specimens CNB3M and CB3M confirmed this finding, but specimen CNB2M did not behave as well as specimen CB2M. The reason for this disparity is not known.

Behavior of Cyclically Loaded Specimens.—On first loading, behavior is as described for monotonically loaded specimens subject to low loads, with most of the shear resistance being due to direct bearing of asperities on the faces of the crack.

When the shear is reduced to zero, the slip does not reduce until the applied shear is less than the net restoring force due to the combined effects of elastic deformation of the reinforcing bars and of the concrete, and any friction between the crack faces. When the applied shear is zero, some slip remains, corresponding to whatever frictional force continues to act between the crack faces.

As the shear is increased in the reverse direction for the first time, the mechanisms by which shear is resisted are the same as on first loading. The behavior on unloading will also be similar to the behavior on first unloading in the opposite direction.

The behavior in subsequent load cycles is somewhat different. In order for the asperities to be brought into bearing, a slip must occur almost equal to the maximum slip that has previously occurred. Prior to this, shear resistance is developed only by dowel action of the reinforcement and by any small friction between the crack faces. The shear stiffness is consequently much lower initially than in the first cycle of loading Fig. 4(a). When the asperities come into bearing, further slip requires deformation of the asperities. The resistance of the asperities to deformation results in a sharp increase in resistance to shear, and an increasing tangent shear stiffness until the maximum shear is reached.

On removing the shear, the response and underlying mechanism of behavior are similar to that in the first cycle. When the shear is reversed in direction, the response and mechanism of behavior are as described.

With each cycle of load, the surfaces in contact are abraded and become smoother, further reducing the frictional resistance to shear at low shears. This is reflected in a further reduction in the shear stiffness at low shears, which is about 20% of the effective stiffness at maximum shear in the same load cycle.

As the maximum shear is increased, the maximum slip and separations become greater. This leads to the development of larger dowel forces and tensile stresses in the reinforcement. Consequently, an increasing fraction of the shear is resisted by friction between the crack faces and by dowel action.

A further change in behavior occurs in the last few loading cycles before failure. In these cycles, the separation at zero shear starts to increase, the tangent shear stiffness approaching maximum shear starts to decrease, and the slip and separation at maximum shear increase significantly in each cycle. This behavior is in large part due to local crushing of the crack faces. Some of the mortar particles produced by this become trapped between the faces of the crack, wedging it open, and also acting like "ball bearings" when the crack faces move relative to one another. Progressive yielding of the reinforcing bars, under the combination of direct tension, and of bending and shear resulting

from dowel action, will also contribute to the deterioration in behavior at this stage.

It can be seen in Figs. 3(a) and 6(a) and Tables 5 and 6, that the behavior and strength of the initially cracked composite specimens with good bond at the roughened interface (Series CB) was very similar to that of the initially cracked, monolithic, normal-weight concrete specimens (Series MN). (In Figs. 3 and 6, the slip plotted for cyclic loading is the numerical average of the slip occurring at the maximum positive and negative shears in each loading cycle.) In both cases, until significant deterioration of the crack faces began to occur shortly before failure, the slip at maximum shear in each loading cycle was close to the slip occurring at same shear in the companion monotonic loading test. In both Series MN and Series CB, the ratio of the strength under cyclic loading to the strength under monotonic loading averaged a little over 0.8.

Fig. 3(b) shows an example of the progressive deterioration of initially cracked, monolithic, lightweight concrete specimens subjected to cyclic load. At all levels of load, the slip under cyclic loading was greater and the separation was less than that which occurred under monotonic loading at the same shear. It can be seen in Table 5 that the separations at failure in the lightweight concrete specimens were very much less than in the comparable normal weight concrete specimens. This difference in behavior was noted in earlier (7) monotonic loading tests. It was then postulated that this is because of the difference in minor roughness of the crack faces in the two cases, due to the absence of sand particles in the lightweight concrete. (It was pointed out that the magnitude of the slip and separation at failure was of the same order as the size of the sand particles.)

In the normal weight concrete the crack passes along the interface between the cement paste and the aggregate particles, because the bond strength between the cement paste and the aggregate particles is less than the tensile strength of the aggregate particles. The minor roughness of the crack faces, therefore, reflects the size and shape of the sand particles. In all lightweight concrete, the bond strength between the cement paste and the aggregate is greater than the tensile strength of the aggregate. In this case the crack passes through the aggregate particles and both the minor and major roughness are less than in normal weight concrete.

Stable shear-slip behavior probably depends upon the interlocking of asperities on the crack faces. This would not be possible to the same extent in the case of the smoother crack faces of the lightweight concrete, as in the case of the rougher crack faces of the normal weight concrete. The shear transfer strength of cracked, monolithic, lightweight concrete is less than that of cracked, monolithic normal weight concrete under both monotonic and cyclic loading. As a result, the ratio of the shear transfer strength under cyclic loading to the shear transfer strength under monotonic loading is about 0.8 for both concretes.

In the cyclic loading tests, the behavior of the unbonded composite specimens deteriorated much more rapidly than did that of the initially cracked, bonded composite specimens. It can be seen in Fig. 6(b) that, in the unbonded composite specimens, the slip at maximum shear never stabilized for a given range of shear, as was the case in the cracked, bonded composite specimens and cracked, monolithic, normal weight concrete specimens. This difference in behavior may

be due to a difference in the minor roughness in the two types of composite specimens, as in the case of lightweight concrete and normal weight concrete previously mentioned.

In the cracked, composite specimens, which had good bond at the interface, it is likely that the crack propagated along and close to the formed interface. At cracking, sand particles would be exposed to create minor roughness conditions approaching those for a crack in monolithic concrete. This minor roughness in the cracked, bonded composite specimens was evidently able to resist the repeated abrasion of cyclic loading as effectively as was the minor roughness in the cracked monolithic concrete, since in both cases the reduction in shear transfer strength due to cyclic loading was about the same.

In the case of the composite specimens without bond, the reduction in shear transfer strength due to cyclic loading was much greater, 40% compared to 20%, than in the case of the bonded, composite specimens. The bond breaker formed the equivalent of a fine crack at the interface, and the major roughness was probably the same as for the cracked, bonded specimen. However, the minor roughness would only be that formed incidentally in the mortar, when the interface was roughened at the time the first half of the specimen was cast. The minor roughness of such an interface would be softer and less able to resist the repeated abrasion of cyclic loading, than would the minor roughness consisting of exposed sand grains in the cracked, bonded composite specimens and cracked monolithic specimens.

Only in the case of the composite specimens without bond did splitting cracks occur perpendicular to the shear plane at the location of the reinforcement. This indicates that for these specimens, larger dowel forces were developed in the reinforcement than in the case of the cracked monolithic and bonded composite specimens, where such cracking did not occur. The greater dowel forces probably resulted from the combination of lower axial tension in the bars and the occurrence of larger slips in the shear plane, both due to the smoother interface.

In Fig. 7, average values of damping factor β for each test series are plotted against percentage of cycles to cause failure. The damping factor calculated was defined by Jacobsen (3).

$$\beta = \frac{1}{2\pi} \cdot \frac{\text{Area within hysteresis loop}}{\text{Area under "skeleton curve"}} = \frac{1}{2\pi} \cdot \frac{A_h}{A_1} \dots \dots \dots (3)$$

in which A_h and A_1 are as shown in Fig. 7. No attempt was made to draw skeleton curves for the shear-slip hysteresis loops obtained in these tests. Instead, it was assumed that the skeleton curve divides the hysteresis loop into two equal areas. β is then given by

$$\beta = \frac{1}{2\pi} \cdot \frac{A_h}{\left(A_2 - \frac{A_h}{2}\right)} \dots \dots \dots (4)$$

in which A_2 is the area bounded by LMNOPQL in Fig. 7. The damping factor calculated in this way has a maximum possible value of 0.318. The significance of the individual numerical values is questionable, but it is thought that the

trends in the variation of the values are of interest and reflect the observed behavior.

In all cases the damping factor dropped rapidly in the first few cycles of loading to 50% of $V_u(\text{calc.})$, reflecting the greater amount of energy dissipated in the initial shearing off of asperities, as compared to later cycles. Similarly, in the last few cycles before failure, the damping factor increased rapidly in

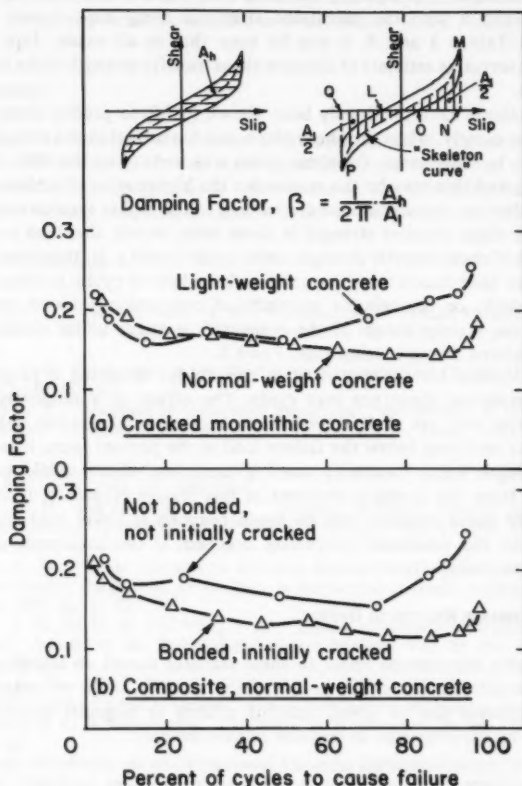


FIG. 7.—Variation of Damping Factor with Number of Cycles of Load and Type of Specimen

all cases, due to the dissipation of energy as the crack faces were increasingly severely damaged approaching failure.

In the interim, the damping factor decreased only a small amount in the cases of the cracked, monolithic, normal weight concrete and the cracked, composite concrete. This corresponds to the period during which the shear-slip

hysteresis loops were stable for these types of specimen. However, after an initial tendency to exhibit the same damping behavior, the damping factor increased significantly in the cases of the cracked, monolithic, lightweight concrete and the composite concrete specimens without bond at the interface. This increase in damping corresponds to the increasing slips at constant maximum shear, noted in these specimens at relatively early stages in their loading.

Ultimate Strength.—Comparing the measured shear transfer strengths listed in Tables 5 and 6 with the calculated strengths using Eqs. 1 and 2, which are listed in Tables 3 and 4, it can be seen that in all cases, Eqs. 1 and 2 yielded a conservative estimate of ultimate shear transfer strength in the monotonic loading tests.

These equations have previously been shown (6,7,8) to predict shear transfer strength quite closely, when the shear plane was horizontal at the time of casting the concrete. In these tests, the shear plane was vertical at the time of casting the concrete, and this may be the reason for the higher strengths obtained.

It is probable that the circumstances leading to the higher than average values of monotonic shear transfer strength in these tests, would also lead to similarly higher values of shear transfer strength under cyclic loading. It, therefore, appears appropriate to base conclusions concerning the effect of cyclic loading on shear transfer strength, on the relative strengths of companion pairs of specimens; rather than on a comparison of the measured strength under cyclic loading and the calculated strength using Eqs. 1 and 2.

Only one loading history was used in this study, involving a progressively increasing maximum shear per load cycle. The effect of a randomly varying maximum shear was not studied. However, because of the stable behavior of the specimens until just below the failure load in the present tests, it is believed that the strength under randomly varying maximum shear would not differ significantly from the strength obtained in this study. However, it should be noted that the shear stiffness will be much reduced at lower maximum loads per cycle than the maximum previously reached, if the maximum shear per cycle varies randomly.

CONCLUDING REMARKS RELATED TO DESIGN

The following conclusions relate to shear transfer across an initially cracked shear plane or unbonded interface in composite concrete, when secondary failure of nearby concrete due to dowel splitting effects or diagonal tension cracks is prevented by the provision of suitable reinforcement.

1. It is recommended that shear transfer strength under cyclically reversing loading be taken as 0.8 of the shear transfer strength under monotonic loading, for the following cases: a shear plane in normal weight or lightweight monolithic concrete and a rough interface between concretes cast at different times, when good bond has been obtained at the interface.
2. If the interface is roughened as specified in Section 11.7.9 of ACI 318-77 (2) and if good bond is obtained at the interface, then after cracking shear transfer behavior under both monotonic and cyclic loading will be essentially the same as in the case of shear transfer across a crack in monolithic concrete.
3. If bond at the interface between concretes cast at different times is destroyed,

shear transfer behavior under cyclic loading deteriorates rapidly and the shear transfer strength is only about 0.6 of the shear transfer strength under monotonic loading.

4. Because of the considerable influence on shear transfer behavior and strength, of interface roughness and bond between concretes cast at different times; every precaution should be taken to obtain adequate roughness and good bond at interfaces that are likely to be subjected to cyclically reversing load, such as in composite construction and in construction joints subject to seismic loading.

ACKNOWLEDGMENT

This study was carried out in the Structural Research Laboratory of the University of Washington. It was made possible by the support of the National Science Foundation. Contributions were made to the execution of the study by graduate students I. J. Lin, C. L. Chou, A. B. Schroeder, and Y. S. Su.

APPENDIX I.—REFERENCES

1. Birkeland, P. W., and Birkeland, H. W., "Connections in Precast Concrete Construction," *Journal of the American Concrete Institute*, Vol. 63, No. 3, Mar., 1966, pp. 345-368.
2. "Building Code Requirements for Reinforced Concrete," (ACI 318-77), American Concrete Institute, 1977.
3. Jacobsen, L. S., "Damping in Composite Structures," *Proceedings of the 2nd World Conference on Earthquake Engineering*, Tokyo and Kyoto, Japan, 1960, Vol. 2, pp. 1029-1044.
4. Mast, R. F., "Auxiliary Reinforcement in Concrete Connections," *Proceedings, ASCE*, Vol. 94, ST6, June, 1968, pp. 1485-1504.
5. Mattock, A. H., and Hawkins, N. M., "Research on Shear Transfer in Reinforced Concrete," *Journal of the Prestressed Concrete Institute*, Vol. 17, No. 2, Mar.-Apr., 1972, pp. 55-75.
6. Mattock, A. H., "Shear Transfer in Concrete Having Reinforcement at an Angle to the Shear Plane," Publication SP-42 *Shear in Reinforced Concrete*, American Concrete Institute, 1974, pp. 17-42.
7. Mattock, A. H., Li, W. K., and Wang, T. C., "Shear Transfer in Lightweight Reinforced Concrete," *Journal of the Prestressed Concrete Institute*, Vol. 21, No. 1, Jan.-Feb. 1976, pp. 20-39.
8. Mattock, A. H., "Shear Transfer Under Monotonic Loading, Across an Interface Between Concretes Cast at Different Times," *Structures & Mechanics Report SM76-3*, Department of Civil Engineering, University of Washington, Seattle, Wash., Sept., 1976, 68 pp.
9. *PCI Design Handbook*, 1st ed., Prestressed Concrete Institute, Chicago, 1971.

APPENDIX II.—NOTATION

The following symbols are used in this paper:

- A_c = area of shear plane;
 A_h = area within hysteresis loop;
 A_{vf} = total area of shear transfer reinforcement crossing the shear plane;
 A_1 = area under hysteresis loop "skeleton curve";
 A_2 = area bounded by LMNOPQL in Fig. 7;

- f'_c = compressive strength of concrete measured on 6×12 in. (150 \times 300 mm) cylinders;
 f_y = yield strength of reinforcement;
 $V_u(\text{calc.})$ = calculated shear transfer strength;
 β = damping factor; and
 $\rho = A_v/A_c$.

ULTIMATE CAPACITY OF CIRCULAR TUBULAR JOINTS^a

By Joseph A. Yura,¹ M. ASCE, Nicholas Zettlemoyer,² M. ASCE,
and Ian F. Edwards³

INTRODUCTION

Circular tubular members are used extensively in offshore structures because their drag characteristics minimize wave forces on the structure, and their closed cross section provides for buoyancy needed during installation in the ocean environment. Tubular members are also used in many truss type structures which require long slender compression members, since the tubular cross section exhibits a high strength-to-weight ratio.

In most instances, the connections of tubular members are formed by full penetration welding of the carefully contoured ends of the branch members to the continuous chord of the truss. Typical simple tubular joints are shown in Fig. 1 along with some of the geometric terms used in defining joint behavior. The word "simple" implies no stiffening devices and, in the case of *K* joints, nonoverlapping branches.

The first widely used design approach for simple tubular joints, which appeared in 1973 in the American Petroleum Institute's *Recommended Practice* (API RP 2A), was based on a punching shear stress concept (2). The branch axial load and moments were converted to an average applied shear stress in the chord wall which attempts to punch out an area of chord around the perimeter of the branch-chord intersection. The punching shear resistance was developed from a lower bound fit to the results from 38 ultimate strength experiments available at that time (11). The experimental ultimate capacity was used because of the significant post-yield test strength and the inadequacy of theoretical elastic-plastic solutions. A safety factor of 1.8 was incorporated in the design formula.

When more experimental evidence became available, the single punching shear

^aPresented at the May 5-8, 1980, Offshore Technology Conference, held at Houston, Tex.

¹Prof. of Civ. Engrg., The Univ. of Texas at Austin, Austin, Tex.

²Sr. Research Engr., Exxon Production Research Co., Houston, Tex.

³Project Engr., Esso Australia Ltd., Sydney, N.S.W., Australia.

Note.—Discussion open until March 1, 1982. To extend the closing date one month, a written request must be filed with the Manager of Technical and Professional Publications, ASCE. Manuscript was submitted for review for possible publication on June 4, 1981. This paper is part of the Journal of the Structural Division, Proceedings of the American Society of Civil Engineers, ©ASCE, Vol. 107, No. ST10, October, 1981. ISSN 0044-8001/81/0010-1965/\$01.00.

resistance formula was no longer a lower bound, so the API concept was expanded in 1977 to include adjustments for type-of-loading and type-of-joint. The comparison of the more complex capacity equations with test data showed some improvement in reliability, but scatter was still significant (12).

The objective of this paper is to establish improved ultimate capacity equations for tubular joints. The empirical approach is employed here; however, the equation development benefits from a carefully screened data base, which existed as of early 1979. Some of the data are new, unpublished results from the University of Texas, including data for out-of-plane moment loading on the branch (25).

After preliminary discussion of the data base and the equation format, this paper systematically addresses axially loaded T, Y, and DT joints, axially loaded K joints, and moment loaded joints. In each section there is a review of joint performance characteristics, a presentation of the new equation(s), and an analysis

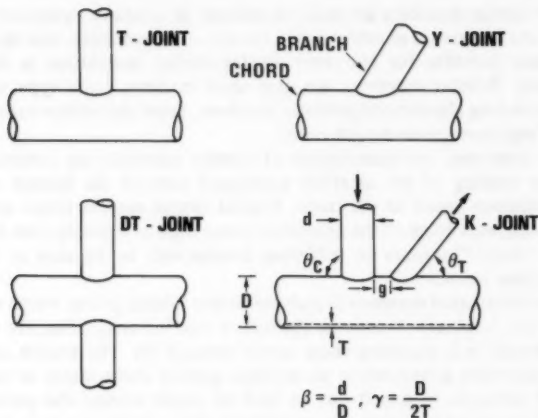


FIG. 1.—Typical Simple Tubular Joints

of each equation's accuracy relative to the data base. The prediction accuracy of the equations in the 1973 and 1977 editions of the American Petroleum Institute's (API) *Recommended Practice* (API RP 2A) (2), with the factor of safety of 1.8 removed, is also given for the same data base. While other published capacity equations exist (7, 16, 17, and 20), space limitations have excluded them from consideration here.

PRELIMINARY CONSIDERATIONS

Data Base Validity.—Comparisons of joint capacity test results, with the predictions of existing capacity equations, generally show extensive scatter (11,12). There are a number of likely sources of the scatter. First, many of the tests were conducted on very small joints—the chord diameters were less than 3 in. (75 mm). With small models it is difficult to properly scale the weld

and local behavior, particularly where fracture is involved. Second, for many tests the material properties were not measured and only minimum *specified* yield strengths are given. Yet, it is common for the actual yield strength in steel pipe to be more than 20% greater than the specified value. Third, much of the test documentation lacks deformation data. If deformations are large, the capacity may be controlled by deflection rather than load. Fourth, occasionally failure resulted from member rather than joint behavior. Finally, in some cases the same test results were reported in more than one publication, and the duplicates were not subsequently edited from the combined data base. This duplication tended to distort the statistics.

An evaluation of the test data was undertaken to provide a sound experimental basis for tubular joint capacity equations. Only those joints with chord diameters larger than 5.5 in. (140 mm) and measured material properties were considered acceptable. This minimum diameter limit is somewhat arbitrary, but the value selected does permit a significant number of data to be retained. Each test report was examined for deformation data and a capacity limit other than joint failure, such as general cross section yielding of the member(s). These and any duplicate data were eliminated from the base. Also, a few compression T results were discounted since short chord lengths gave abnormal importance to the boundary conditions.

In the screened data base, the minimum load from three potential failure criteria has been used to define the useful capacity of each joint. One criterion is the maximum load attained during the test. This is the limit recorded in virtually all test reports. However, in the axial tension situation, the load associated with first crack is considered a more appropriate limit. In laboratory specimens the branch is usually oversized to eliminate branch failure. While this overdesign is believed to have little or no effect on the first crack load, it results in unrealistic reserve strength beyond the crack's first appearance.

The third failure criterion incorporated in the data base is the load at an excessive deformation limit. For axial loading, it is assumed that a branch member reaches its practical deformation limit when the strain along its entire length is four times the yield strain (1,24). It is further assumed that the comparable practical limit of local joint deformation at each branch end is twice the branch yield deformation. Thus, the deformation limit, Δ , may be expressed as

$$\Delta = \frac{2 F_y L}{E} \dots \dots \dots (1)$$

in which L = branch length; and E = Young's modulus. A member length of 30 times its diameter (a typical upper limit for offshore structures) is used to evaluate the deformation limit. However, for many joint and load types this length has only a minor effect on the load limit since the load-deformation plot for the joint is relatively flat over a broad range of deformation.

Equation Format.—It is difficult for one formula to accurately predict the ultimate capacity of tubular joints for a large range of joint geometries and loading configurations. Among other things, the post-yield behavior varies. By introducing more than one equation it is possible to improve both the simplicity and the accuracy. The authors have found that separation of the data into six groups is advantageous and does not result in an unmanageable set of equations.

API RP 2A makes use of the punching shear concept to predict capacity (2,11,12). While the concept has proven useful, it does not properly reflect the actual mode of failure at a joint. Several recent equation recommendations have avoided the failure mode issue by describing the capacity in terms of ultimate branch force or moment (7,16,20). The branch loading format has been selected for the new equation development. Use of branch force and moment should simplify the design procedure, since member end forces and moments are the common products of a structural analysis.

AXIALLY LOADED T, Y, AND DT JOINTS

Performance Characteristics.—Typical load-deflection behavior of T and DT tubular joints subjected to axial compression and axial tension is shown in

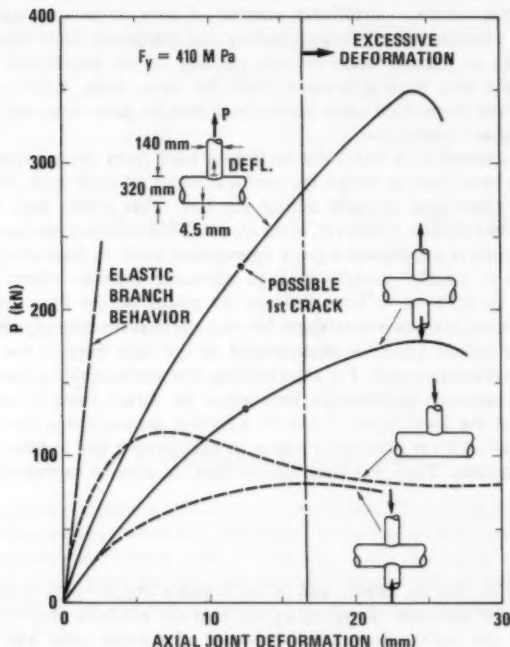


FIG. 2.—Load-Deflection Behavior of Axially Loaded T and DT Joints (21)

Fig. 2 for a companion set of four tests with similar member sizes (20). The behavior of the tension specimens is characterized by a gradually increasing rate of deformation caused by yielding of the chord around the branch and distortion of the cross section (ovaling) until a first crack has formed. [No first crack data are actually reported (20); the crack loads shown are for illustration

only.) The branch load continues to increase until gross separation occurs. The DT joint behavior in tension is similar to the T joint, but both the stiffness and capacity are reduced.

Compression loading produces the lowest joint capacity. Failure is usually associated with yielding, buckling, and gross distortion of the chord wall. Again, the DT joint is weaker than the T joint, except possibly at β values near 1.0. The initial stiffness of the joint is similar for both compression and tension loading. For reference purposes, the theoretical elastic response of the branch itself is also shown, assuming a member length of 30 times the branch diameter. The joint stiffness is significantly less than the member stiffness, especially for the DT joints.

Compression Data and Capacity Equations.—The published compression data for T, Y, and DT joints, which are considered reliable, are presented in Table 1. The ultimate test load, P_T , is nondimensionalized by the factor $T^2 F_y$, which is related to the plastic bending strength per unit length of plate. This factor is common to many suggested ultimate strength formulations for circular and rectangular tubular connections, especially those based on a yield-line analysis (7,13,19). Unless otherwise noted, the branches intersect the chord at a 90° angle.

The T and Y data are plotted in Fig. 3. Even though the range of γ (defined in Fig. 1) is quite large, the nondimensionalized ultimate load shows good correlation to β alone. The Y tests show an average 18% increase in strength above the companion T tests. This increase is close to the 21% indicated by the K_a term in the API formulas (2) in which $K_a = (1 + \sin \Theta)/2 \sin \Theta$.

T and Y data are available for β up to 0.7. At larger values of β , some tests were conducted (10), but the short chord lengths affected the results (7). In actual structures, T and Y joint failures at the $\beta = 1.0$ condition are unlikely because the chord member will fail due to the high bending moments introduced by the branch force. Thus, the following equation could be used to represent the lower bound capacity over the entire range of β :

$$P_u = \frac{F_y T^2}{\sin \theta} (3.4 + 19\beta) \dots \dots \dots (2)$$

No additional correction, such as K_a , is recommended for Y joints because of the limited number and scope of Y data. Also, tension tests to be discussed later suggest that the K_a adjustment is nonconservative.

It is interesting to reflect on the constant 3.4 in Eq. 2. As β approaches zero the branch represents more of a point load on the local chord surface, which might be viewed as a flat plate in the relative sense. A yield-line analysis of a square plate with a perpendicular point load gives a constant of 4.0, independent of the plate planar dimension. Thus, the limiting value of 3.4 seems reasonable with reference to the yield-line approach.

The DT data from Table 1 are plotted in Fig. 4 and cover the full practical range of γ and β . At low values of β , the ultimate load is similar to that developed in T joints. However, in the mid range of β , DT joints show a reduced capacity. At high β , the capacity increases significantly because the load is transferred between the branches, primarily by membrane action rather than bending of the chord wall.

TABLE 1.—Data Summary: T, Y, and DT Joints in Compression

Test (1)	D, in mil- li- me- ters (2)	d, in mil- li- me- ters (3)	T, in mil- li- me- ters (4)	F _y , in mega- pas- cals (5)	γ (6)	β (7)	P _T sin θ / T ² F _y (8)	Col- umn 8/ API- 73 (9)	Col- umn 8/ API- 77 (10)	Col- umn 8/ Equa- tion 2 or 3 (11)
(a) T-Joints										
CE 3 ^a	139.8	101.6	6.5	323	10.8	0.727	17.26	0.884	0.884	1.003
CF 4 ^a	139.8	101.6	6.5	323	10.8	0.727	18.70	0.957	0.957	1.086
CB-40-0.2 ^b	164.5	42.7	4.7	440	17.5	0.258	8.65	1.121	1.121	1.037
CB-40-0.4 ^b	164.5	76.3	4.7	440	17.5	0.462	11.97	0.870	0.870	0.980
CB-70-0.2 ^b	319.5	60.5	4.5	410	35.5	0.190	7.05	1.017	1.017	1.008
CB-70-0.4 ^b	319.5	139.8	4.5	410	35.5	0.440	12.23	0.761	0.761	1.043
CB-100-0.2 ^b	455.7	89.1	4.9	390	46.5	0.195	6.67	0.856	0.856	0.936
CB-100-0.4 ^b	455.7	165.2	4.9	390	46.5	0.362	10.41	0.721	0.721	1.011
(b) Y-Joints; $\theta = 45^\circ$										
CB'-40-0.4 ^b	164.5	76.3	4.7	430	17.5	0.464	13.82	0.832	0.832	1.131
CB'-70-0.4 ^b	319.5	139.8	4.4	410	35.5	0.440	15.56	0.802	0.802	1.327
CB'-100-0.4 ^b	455.7	165.2	4.9	390	46.5	0.362	11.56	0.663	0.663	1.122
(c) DT-Joints										
CS-40-0.2 ^b	165.2	42.7	4.7	480	17.5	0.260	6.84	0.894	0.894	1.013
CS-40-0.4 ^b	165.2	76.3	4.7	480	17.5	0.460	9.61	0.701	0.949	1.022
CS-40-0.6 ^b	165.2	114.3	4.7	480	17.5	0.690	12.93	0.617	0.881	1.020
CS-40-1.0 ^b	165.2	165.2	4.7	480	17.5	1.000	30.49	0.572	0.817	1.033
CS-70-0.2 ^b	318.5	60.5	4.4	420	36.2	0.190	6.01	0.858	0.858	1.023
CS-70-0.4 ^b	318.5	139.8	4.4	420	36.2	0.435	10.01	0.618	0.820	1.099
CS-70-0.6 ^b	318.5	165.2	4.5	410	35.4	0.520	11.29	0.594	0.833	1.113
CS-70-1.0 ^b	318.5	318.5	4.5	410	35.4	1.000	37.04	0.563	0.804	1.255
CS-100-0.2 ^{b,c}	457.2	89.1	4.8	390	47.6	0.195	5.54	0.709	0.709	0.933
CS-100-0.4 ^b	457.2	165.2	4.8	390	47.6	0.361	8.90	0.616	0.740	1.100
CG-1 ^a	139.8	139.8	6.5	323	10.3	1.000	32.37	0.712	1.017	1.097
CG-2 ^a	139.8	114.3	6.5	323	10.3	0.818	17.99	0.755	1.079	1.113
CG-3 ^a	139.8	101.6	6.5	323	10.3	0.727	14.46	0.752	1.039	1.075
CG-4 ^a	139.8	76.3	6.5	323	10.3	0.546	11.37	0.823	1.167	1.083
CG-5 ^a	139.8	48.6	6.5	323	10.3	0.348	8.42	0.956	1.126	1.063
1 ^d	190.1	48.3	4.69	310	20.3	0.254	6.94	0.881	0.881	1.036
2 ^d	193.7	48.3	6.50	330	14.9	0.250	6.81	0.964	0.964	1.024
3 ^d	193.7	48.3	9.39	280	11.0	0.250	6.97	1.081	1.081	1.048
4 ^d	188.9	101.6	4.65	310	20.3	0.538	11.28	0.676	0.955	1.085
5 ^d	193.7	101.6	6.50	330	14.9	0.520	10.78	0.734	1.030	1.061
6 ^d	193.7	101.6	9.30	280	10.4	0.520	11.37	0.861	1.210	1.119
7 ^d	190.0	159.0	4.56	310	20.8	0.837	19.20	0.620	0.885	1.164
8 ^d	193.7	159.0	6.50	333	14.9	0.820	16.00	0.598	0.854	0.985
9 ^d	193.7	159.0	9.35	280	10.4	0.820	18.23	0.759	1.084	1.122
A2-3 ^e	159 ^b	83	5	340	15.9	0.522	10.97	0.729	1.025	1.077
A2-4 ^e	159 ^b	83	5	340	15.9	0.522	10.63	0.707	0.992	1.044

TABLE 1.—Continued

(1)	(2)	(3)	(4)	(5)	(6)	(7)	(8)	(9)	(10)	(11)
-----	-----	-----	-----	-----	-----	-----	-----	-----	------	------

Note: For column 9, the mean of column 9 is 0.779, the standard deviation 0.144, and the coefficient of variation 18.5%. For column 10, the mean of column 10 is 0.923, the standard deviation 0.136, and the coefficient of variation is 14.7%. For column 11, the mean of column 11 is 1.067, the standard deviation 0.076, and the coefficient of variation is 7.1%.

^aFrom Ref. 10.

^bFrom Ref. 20.

^cDeformation controlled.

^dFrom Ref. 7.

^eFrom Ref. 18.

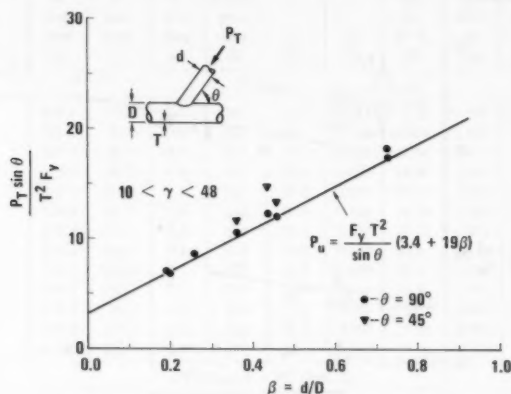


FIG. 3.—Compression Loading of T and Y Joints

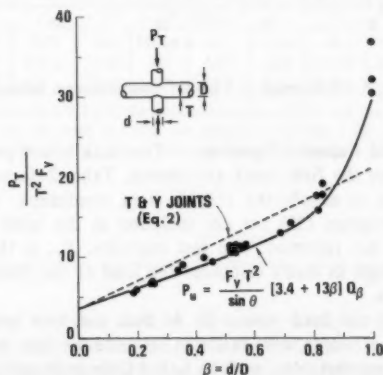


FIG. 4.—Compression Loading of DT Joints

Fig. 4 suggests that γ has no significant effect on joint capacity. This point is clarified in Fig. 5 where the data from Table 1 are organized as a function of γ . At β less than 0.6, a variation of γ from 10-36 shows no effect. At higher β , there is evidence of a slight effect.

The lower bound capacity equation shown in Fig. 4 is

$$P_u = \frac{F_y T^2}{\sin \theta} (3.4 + 13\beta) Q_\beta \quad (3)$$

in which $Q_\beta = 1.0$ for $\beta \leq 0.6$; and $Q_\beta = 0.3/\beta(1 - 5\beta/6)$ for $\beta > 6$. The $\sin \theta$ term is used in Eq. 3 even though no X (or DY) joints are reported in Table 1. Use of the DT equation for X joints is inferred from the relationship of T and Y data.

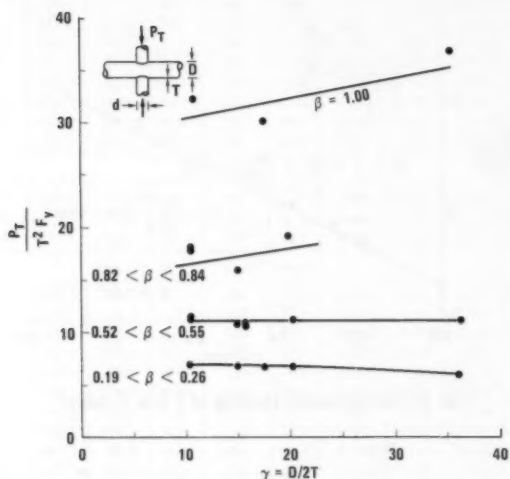


FIG. 5.—Influence of γ on DT Compression Strength

Tension Data and Capacity Equations.—Test data which provide information on the formation of the first crack are limited. Table 2 documents the 19 tests which were found to satisfy the reliable data conditions. The 16 tests from the large JSSC program (20) are not included in the table because the first crack loads were not reported. The test capacity, P_T , is the first crack load in all cases, although in many instances the load at the deformation limit was only slightly higher.

Fig. 6 plots the test load versus β . At best the data can be described as scattered. Various attempts were made to organize the data in a tighter arrangement using other test variables, such as γ , but little improvement was observed. Actually, the scatter cannot be reduced significantly because of the variation in the first crack load itself. The four data between points a and b represent

almost identical specimens, yet the first crack load varied by 60%. When failures are due to fracture of the material, considerable scatter should be expected because of difficulties in defining when the crack has formed and whether surface cracks, or through thickness cracks, are reported. Also, fracture characteristics of the material do not bear a constant relationship to yield strength.

TABLE 2.—Data Summary: T, Y, and DT Joints in Tension

Test (1)	D , in mil- li- me- ters (2)	d , in mil- li- me- ters (3)	T , in mil- li- me- ters (4)	F_y , in mega- pas- cals (5)	γ (6)	β (7)	P_T \sin $\theta /$ $T^2 F_y$ (8)	Col- umn 8/ API- 73 (9)	Col- umn 8/ API- 77 (10)	Col- umn 8/ Equa- tion 2 (11)
T-Joints										
T1 ^a	323.9	73.0	12.7	283	12.3	0.218	6.82	1.173	0.838	0.904
T2 ^a	323.9	73.0	6.4	283	25.5	0.214	17.56	2.471	1.765	2.352
T3 ^a	406.4	88.9	6.4	283	31.5	0.209	15.61	2.111	1.508	2.118
T4 ^a	323.9	141.3	6.4	283	25.5	0.425	14.83	1.051	0.751	1.292
T4 ^a	219.1	141.3	6.4	283	16.8	0.643	24.20	1.278	0.917	1.550
T6 ^a	323.9	141.3	6.4	283	25.5	0.425	16.78	1.189	0.849	1.462
T7 ^a	323.9	141.3	6.4	283	25.5	0.425	15.22	1.078	0.770	1.326
1 ^b	219.1	141.3	7.1	324	15.5	0.645	39.4	2.124	1.526	2.517
2 ^b	219.1	141.3	7.1	324	15.5	0.645	39.1	2.108	1.514	2.497
3 ^b	219.1	141.3	7.1	324	15.5	0.645	33.6	1.811	1.301	2.146
1 ^c	323.9	60.3	6.4	290	25.5	0.173	5.71	0.994	0.710	0.854
2 ^c	323.9	101.6	6.4	290	25.5	0.302	9.14	0.991	0.651	1.002
3 ^c	323.9	273.1	6.4	290	25.5	0.840	19.05	0.573	0.488	0.984
Y-Joints $\theta = 45^\circ$ (Ref. 3)										
5 ^c	323.9	60.3	6.4	290	25.5	0.173	5.93	0.855	0.890	0.887
6 ^c	323.9	101.6	6.4	290	25.5	0.302	8.08	0.668	0.695	0.884
7 ^c	323.9	273.1	6.4	290	25.5	0.840	16.16	0.403	0.420	0.835
DT-Joints										
10 ^d	193.7	48.3	6.67	333	14.5	0.249	9.25	1.325	1.325	1.138
11 ^d	193.7	101.6	6.59	333	14.7	0.525	13.55	0.917	0.917	1.013
12 ^d	193.7	159	6.65	333	14.6	0.821	19.95	0.748	0.748	1.050

Note: For column 9, the mean is 1.252, the standard deviation 0.593, and the coefficient of variation is 47.4%. For column 10, the mean is 0.978, the standard deviation 0.389, and the coefficient of variation 39.8%. For column 11, the mean is 1.411, the standard deviation 0.603, and the coefficient of variation is 42.7%.

^aFrom Ref. 21.
^bFrom Ref. 6.
^cFrom Ref. 3.
^dFrom Ref. 7.

A lower bound of the data follows the same trend as the compression T data (Fig. 3). Tests with the largest chord diameters are particularly close to the lower bound. The limited DT and Y data also follow the lower bound. A comparison of Beale's companion T and Y data (3) indicates the additional capacity of the Y joint is accurately reflected by the $\sin \theta$ term. Novikov's

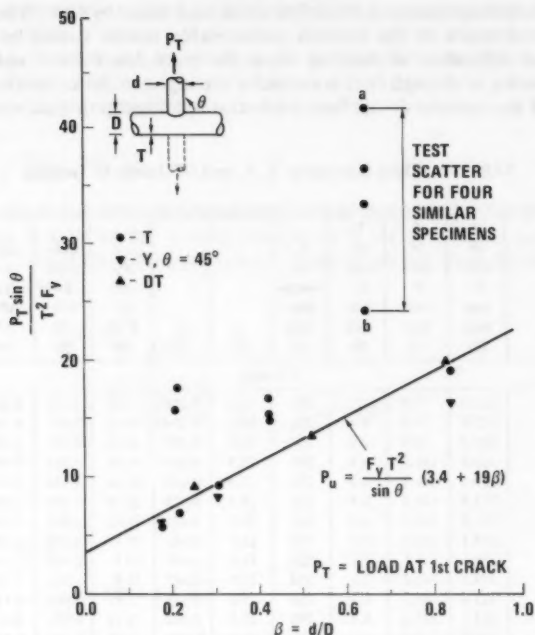


FIG. 6.—Tension Loading of T, Y, and DT Joints

tests on matched 90° and 30° DT specimens (15) also suggest the API K_a term overestimates the increase in joint capacity. Novikov's tests are not included in Table 2 because no first crack loads or material properties were reported.

DATA ANALYSIS

The experimental capacities of the compression specimens are compared to Eqs. 2 and 3 and to API predictions in Table 1. Histograms of the results are given (26). For these tests, the 1973 API equation typically overestimates the true capacity. The adjustments made in the 1977 API edition still result in significant scatter, but the ratios of test/theory are closer to the ideal value of 1.0. It can be seen that Eqs. 2 and 3 provide a good evaluation of the lower bound joint capacity with reduced scatter.

The statistical summary given in Table 2 for the tension data shows that all methods of strength prediction result in considerable scatter, while the coefficients of variation are 40% or greater. Once again, the 1977 API approach provides estimates close to the data mean, while Eq. 2 represents essentially a lower bound.

AXIALLY LOADED K JOINTS

Performance Characteristics.—Various studies on K joints have indicated that

TABLE 3.—Data Summary: Axially Loaded K Joints

Test (1)	D , in mil- li- meters (2)	d , in mil- li- meters (3)	T , in mil- li- meters (4)	F_y , in mega- pascals (5)	γ (6)	β (7)	g/d (8)	P_T \sin $\theta/T^2 F_y$ (9)	Col- umn 9/ API- 73 (10)	Col- umn 9/ API- 77 (11)	Col- umn 9/ Equa- tion 4 (12)
Bouwkamp, $\theta_c = 90^\circ$; $\theta_r = 45^\circ$ (Ref. 4, 5)											
I	323.9	168.3	6.4	290	25.0	0.520	0.236	36.90	2.150	2.039	1.725
II-3	168.3	60.3	5.6	395	14.6	0.358	0.186	20.60	2.049	1.756	1.223
II-6	219.1	88.9	5.6	395	19.2	0.406	0.024	20.60	1.664	1.299	1.041
II-9	273.1	88.9	4.8	425	28.1	0.326	0.324	14.58	1.308	1.201	0.986
I-10	168.3	60.3	7.1	290	11.3	0.358	0.186	18.22	1.957	1.677	1.082
EPRC, $\theta_c = 45^\circ$, $\theta_r = 45^\circ$ (Ref. 9)											
7	508.0	219.0	12.7	494	20.0	0.431	0.905	16.70	1.040	1.040	1.339
8	508.0	219.0	12.7	494	20.0	0.431	0.905	16.70	1.040	1.040	1.339
9	508.0	324.0	12.7	494	20.0	0.638	0.154	25.92	1.086	0.988	0.996
10	508.0	324.0	12.7	494	20.0	0.638	0.154	27.31	1.145	1.041	1.049
11	508.0	324.0	12.7	276	20.0	0.638	0.154	34.79	1.458	1.326	1.337
12	508.0	324.0	12.7	276	20.0	0.638	0.154	33.54	1.406	1.279	1.289
JSSC, $\theta_c = 90^\circ$; $\theta_r = 45^\circ$ (Ref. 20)											
CK-40-0.2	165.5	42.7	4.6	484	17.8	0.258	0.730	9.34	1.214	1.214	0.925
CK-70-0.2	318.4	60.5	4.4	412	36.2	0.190	1.425	10.82	1.544	1.544	1.544
CK-100-0.2	456.9	89.1	4.9	402	46.5	0.195	1.357	9.14	1.178	1.178	1.286
CK-100-0.4	458.9	165.2	4.9	402	46.8	0.360	0.182	24.38	1.700	1.454	1.439
JSSC, $\theta_c = 45^\circ$; $\theta_r = 45^\circ$ (Ref. 20)											
TK-40-0.2	165.5	42.7	4.7	490	17.6	0.258	2.460	9.28	1.003	1.003	1.118
TK-40-0.4	165.9	76.3	4.7	490	17.6	0.460	0.760	15.68	0.951	0.951	1.084
TK-40-0.6	165.2	114.3	4.7	490	17.6	0.692	0.031	31.05	1.223	0.995	1.057
TK-70-0.2	318.4	60.5	4.5	422	35.4	0.190	3.849	8.93	1.063	1.063	1.274
*TK-70-0.4	321.4	139.8	4.5	422	35.7	0.435	0.855	16.24	0.842	0.842	1.247
TK-70-0.6	317.7	165.2	4.5	422	35.3	0.520	0.509	21.11	0.919	0.919	1.141
*TK-100-0.2	456.9	89.1	5.0	451	45.7	0.195	3.714	7.38	0.793	0.793	1.039
*TK-100-0.4	458.9	165.2	5.0	432	45.1	0.360	1.364	13.44	0.785	0.785	1.313
Nakajima, $\theta_c = 45^\circ$; $\theta_r = 90^\circ$ (Ref. 14)											
1	165.2	76.3	1.6	348	51.6	0.461	0.131	38.20	1.673	1.419	1.853
2	165.2	76.3	2.3	288	35.9	0.461	0.131	28.05	1.370	1.162	1.361
3	165.2	60.5	2.3	338	35.9	0.366	0.165	23.52	1.447	1.227	1.362
4	165.2	48.6	2.3	340	35.9	0.294	0.205	23.00	1.762	1.494	1.565
5	165.2	76.3	2.3	294	35.9	0.461	0.131	35.56	1.737	1.473	1.725
6	165.2	76.3	3.2	314	24.8	0.461	0.131	30.04	1.639	1.390	1.457
7	165.2	76.3	4.5	348	18.4	0.461	0.131	28.33	1.691	1.434	1.374
8	165.2	76.3	6.0	278	13.8	0.461	0.131	24.78	1.612	1.367	1.202
9	165.2	76.3	6.0	282	13.8	0.461	0.131	22.17	1.443	1.223	1.076
Nakajima, $\theta_c = 90^\circ$; $\theta_r = 45^\circ$ (Ref. 14)											
10	165.2	76.3	1.6	358	51.6	0.461	0.131	42.92	2.270	1.925	2.082
11	165.2	76.3	2.3	339	35.9	0.461	0.131	41.80	2.470	2.095	2.033
12	165.2	60.5	2.3	342	35.9	0.366	0.165	31.31	2.325	1.972	1.813
13	165.2	48.6	2.3	270	35.9	0.294	0.205	32.72	3.025	2.565	2.226
14	165.2	76.3	2.3	285	35.9	0.461	0.131	35.34	2.084	1.767	1.715
15	165.2	76.3	3.2	263	25.8	0.461	0.131	39.97	2.602	2.207	1.939

TABLE 3.—Continued

(1)	(2)	(3)	(4)	(5)	(6)	(7)	(8)	(9)	(10)	(11)	(12)
16	165.2	76.3	6.0	360	13.8	0.461	0.131	20.81	1.635	1.386	1.010
17	165.2	76.3	6.0	292	13.8	0.461	0.131	22.56	1.772	1.503	1.095
Yura, $\theta_c = 90^\circ$; $\theta_t = 30^\circ$ (Ref. 25)											
*C1-1	507.2	326.4	11.1	352	22.8	0.643	0.117	28.03	1.364	1.181	1.052
*C1-2	507.2	326.4	11.1	352	22.8	0.643	0.117	29.67	1.437	1.250	1.113
Zimmermann, $\theta_c = 60^\circ$; $\theta_t = 60^\circ$ (Ref. 27)											
1	419.0	168.3	10.0	340	21.0	0.402	0.284	15.32	1.129	1.054	0.882
2	419.0	168.3	10.0	340	21.0	0.402	0.284	15.42	1.136	1.061	0.888
3	419.0	168.3	10.0	340	21.0	0.402	0.284	15.02	1.107	1.033	0.865
4	419.0	168.3	10.0	239	21.0	0.402	0.284	17.28	1.273	1.189	0.995
Beale—TK Joint, $\theta_c = 45^\circ$; $\theta_t = 90^\circ$; $\theta_c = 45^\circ$ (Ref. 3)											
8	323.9	60.3	6.5	290	15.4	0.173	1.225	9.15 ^b	1.853	1.853	1.368
9	323.9	101.6	6.5	290	15.4	0.302	0.237	13.91 ^b	1.614	1.395	0.945

Note: For column 10, the mean is 1.521, the standard deviation 0.497, and the coefficient of variation 32.7%. For column 11, the mean is 1.355, the standard deviation 0.393, and the coefficient of variation 39%. For column 12, the mean is 1.310, the standard deviation 0.342, and the coefficient of variation 26%.

*Deformation controlled.

^bLoad in tension branch.

the gap, g , between the intersecting branches has a significant influence on the capacity, as do the variables which affect single branch joints (16,23). If the gap is large relative to the members, the joint performs like a single branch joint. As the gap approaches zero, the overall joint strength is increased because the bending stiffness of the chord wall between the branches is increased. For large gaps, the joint capacity is usually controlled by plastic bending and buckling of the chord wall in the vicinity of the compression branch. For small gaps, the joint strength depends on conditions in the gap.

Many axial K tests have had one 90° branch loaded in compression, and a 45° branch loaded in tension. In these cases the gap was in tension, and failure was governed in part by fracture of the chord or welds in this region. Therefore, considerable scatter in the results could have been expected. The Nakajima experimental program included companion tests which had the direction of branch loads reversed (14). Generally, the value of $P_T \sin \theta$ was slightly lower when the 45° branch was in compression. In this case, compressive chord stresses developed in the gap region. More importantly, the need for a K_a term as in API was not supported.

Data and Capacity Equation.—A summary of the experimental K data is shown in Table 3. Except for two tests (25), the branches in each specimen are the same size. θ_c refers to the angle of the compression branch and θ_t to the tension branch. The joint failure loads listed in Table 3 are those on the compression branch (maximum load or load at the deformation limit), except for the TK joints (three branches). In these tests the single branch in tension failed by developing a crack.

The effect of the gap ratio, g/d , on joint strength is shown in Fig. 7. The test loads, P_T , are nondimensionalized by Eq. 2, the capacity prediction for

T and Y joints. Other researchers have related the joint capacity to g/D rather than g/d , but an analysis of both approaches indicates that g/d provides a better organization of the test data. For gaps greater than the branch diameter, the strength is independent of the gap and the connection should be treated

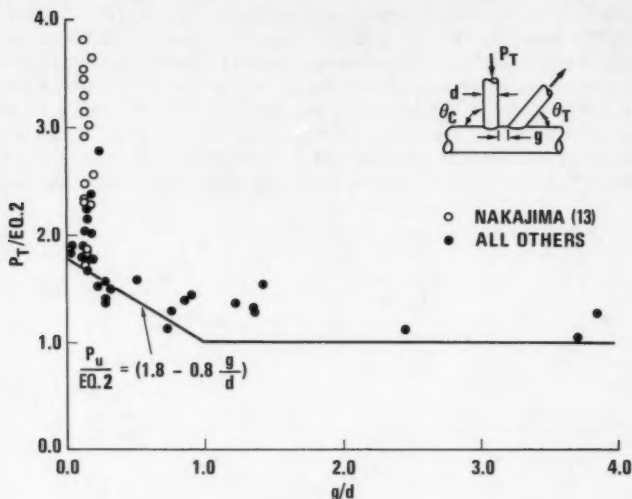


FIG. 7.—Effect of Gap on Axially Loaded K Joints

as a T or Y joint using Eq. 2. For smaller gaps the lower bound capacity can be taken as

$$P_u = \frac{F_y T^2}{\sin \theta} (3.4 + 19\beta) Q_s \dots \dots \dots (4)$$

in which $Q_s = 1.8 - 0.8 g/d \geq 1.0$.

DATA ANALYSIS

The statistical evaluation of the various capacity equations for K joints is given in Table 3. It is seen that Eq. 4 gives a good prediction of the lower bound capacity, while the 1973 and 1977 API equations show greater scatter. In addition, the API equations do not give lower bounds to the JSSC tests. Since the overabundance of data at $g/d < 0.2$ tends to skew the analysis, it is suggested that the 17 Nakajima tests be neglected when assessing the accuracy of the various equations.

MOMENT LOADED JOINTS

Performance Characteristics.—The response of tubular joints to applied in-plane

bending (IPB) and out-of-plane bending (OPB) moment is shown in Fig. 8 (20). Typically, the joint subjected to in-plane bending reaches a maximum load at moderate deformation, with actual failure due to plastic bending and buckling of the chord wall on the compressive side of the branch, and fracture through the chord wall on the tension side. For out-of-plane bending, the chord wall distorts locally, resulting in lower joint stiffness and strength. Fracture may occur, but only after excessive deformation. The practical deformation limit is defined as the joint rotation corresponding to the angle at the end of a simply supported beam, which is uniformly loaded to four times the first-yield strain. A beam length of 30 times the branch diameter is used to establish the limit.

Out-of-plane results are apt to be more sensitive to β than in-plane results. At high β values the branch transfers load to the chord primarily through membrane action in the chord, as opposed to wall bending. Improved capacity and stiffness

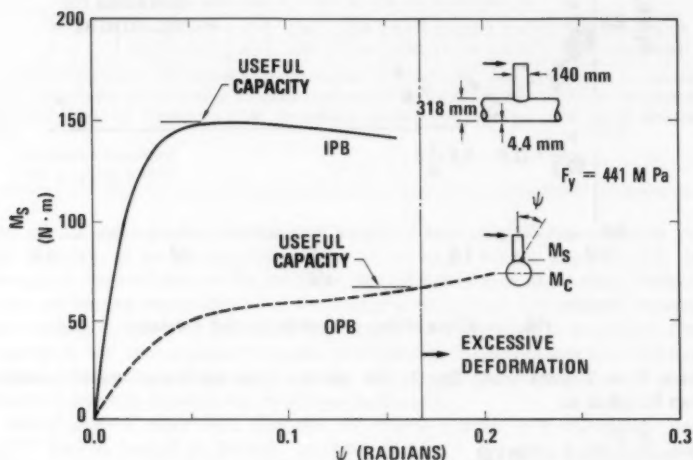


FIG. 8.—Load-Deflection Behavior of Tubular Joints Subjected to Bending

are expected, just as for the DT compression specimens. On the other hand, the mode of load transfer for in-plane bending load is not altered significantly by β .

In-Plane Bending Data and Capacity Equation.—In tests used to study the bending capacity, the branch is normally loaded at its end as a cantilever. Since the moment varies along the length of the branch, the useful strength must be related to a specific location, such as the maximum moment which occurs at the chord centerline, M_c , or the moment at the chord surface, M_s , where the failure actually occurs. In subsequent tables both moments are listed for each test cited, but M_s is used to develop the capacity formula since it provides a slightly better organization of the data. Capacity estimates based on M_s are conservative for situations in which applied moments from a structural analysis are established at the chord center line.

TABLE 4.—Data Summary: In-Plane Bending

Test (1)	D , in mil- li- me- ters (2)	d , in mil- li- me- ters (3)	T , in mil- li- me- ters (4)	F_y , in mega- pas- cals (5)	γ (6)	β (7)	M_x $\sin \theta$ $dT^2 F_y$ (8)	M_c $\sin \theta$ $dT^2 F_y$ (9)	Col- umn 8/ API- 73 (10)	Col- umn 8/ API- 77 (11)	Col- umn 8/ Equa- tion 5 (12)
T-Joints											
4 ^a	219.1	71.6	6.3	314	17.4	0.327	9.24	9.64	3.818	1.909	1.201
6 ^a	298.5	101.6	7.2	294	20.7	0.340	9.24	9.79	3.485	1.743	1.171
7 ^a	219.1	101.6	5.5	305	19.9	0.464	12.45	12.99	3.482	1.741	1.274
8 ^a	219.1	101.6	8.4	367	13.0	0.464	9.81	10.24	3.118	1.559	1.004
9 ^a	219.1	101.6	10.0	368	11.0	0.464	9.34	9.75	3.121	1.560	0.956
11 ^a	219.1	139.7	6.0	314	18.3	0.638	16.34	17.06	3.396	1.698	1.316
12 ^a	219.1	139.7	8.8	422	12.4	0.638	12.90	13.46	3.013	1.507	1.039
14 ^a	298.5	193.7	7.3	296	20.4	0.649	17.48	18.53	3.448	1.724	1.408
17 ^a	219.1	177.8	5.9	314	18.6	0.812	20.85	21.77	2.978	1.489	1.384
18 ^a	219.1	177.8	8.6	422	12.7	0.812	17.68	18.46	2.832	1.416	1.174
B-70-0.2 ^b	318.5	60.5	4.4	441	36.2	0.190	6.45	8.02	3.682	1.841	1.150
B-70-0.4 ^b	318.5	139.8	4.4	441	36.2	0.439	12.48	14.81	3.083	1.542	1.329
B-100-0.2 ^b	457.2	89.1	4.8	402	47.6	0.195	7.37	9.52	3.776	1.888	1.297
B-100-0.4 ^b	457.2	165.2	4.8	402	47.6	0.361	11.79	14.53	3.263	1.631	1.437
K-Joints											
A2-X-90° ^c	507.2	326.4	11.4	350	22.2	0.644	18.34	22.16	3.559	1.583	1.466
A2-X-30° ^c	507.2	455.9	11.4	350	22.2	0.899	16.73	20.92	1.353	1.198	1.021

Note: For column 10, the mean is 3.212, the standard deviation 0.577, and the coefficient of variation 18%. For column 11, the mean is 1.627, the standard deviation 0.185, and the coefficient of variation 11.4%. For column 12, the mean is 1.227, the standard deviation 0.163, and the coefficient of variation 13.3%.

^aFrom Ref. 8.

^bFrom Ref. 20.

^cFrom Ref. 25.

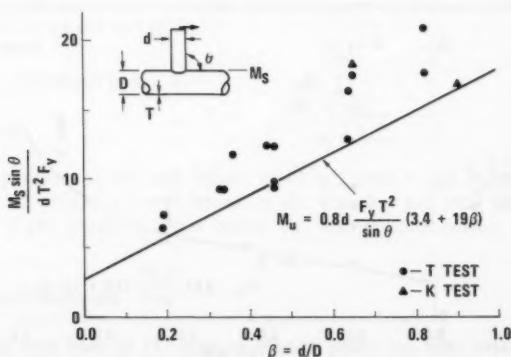


FIG. 9.—In-Plane Bending Loading of T and K Joints

TABLE 5.—Data Summary: Out-of-Plane Bending

Test (1)	D , in mil- li- me- ters (2)	d , in mil- li- me- ters (3)	T , in mil- li- me- ters (4)	F_y , in mega- pas- cals (5)	γ (6)	β (7)	M_s $\sin \theta /$ $dT^2 F_y$ (8)	M_c $\sin \theta /$ $dT^2 F_y$ (9)	Col- umn 8/ API- 73 (10)	Col- umn 8/ API- 77 (11)	Col- umn 8/ Equa- tion 6 (12)
(a) T Joints											
BL-40-0.5 ^a	165.2	76.3	4.5	471	18.4	0.462	5.46	6.08	1.570	1.570	1.029
BL-70-0.2 ^a	318.5	60.5	4.4	441	36.2	0.190	4.10	5.10	2.340	2.340	1.084
BL-70-0.4 ^a	318.5	139.8	4.4	441	36.2	0.439	5.53	6.56	1.366	1.366	1.068
BL-100-0.2 ^a	457.2	89.1	4.8	402	47.6	0.195	4.12	5.32	2.111	2.111	1.081
BL-100-0.4 ^a	457.2	165.2	4.8	402	47.6	0.361	4.36	5.37	1.207	1.207	0.920
G1 ^b	507.2	171.5	11.1	352	22.8	0.338	4.39	5.31	1.618	1.618	0.952
G2 ^b	507.2	171.5	11.1	352	22.8	0.338	4.83	5.84	1.780	1.780	1.047
H1 ^b	507.2	326.4	11.1	352	22.8	0.644	7.29	8.81	1.403	1.403	1.147
H2 ^b	507.2	326.4	11.1	352	22.8	0.644	7.86	9.50	1.513	1.513	1.236
I1 ^b	507.2	455.9	11.1	352	22.8	0.899	13.40	14.79	1.398	1.398	1.300
I2 ^b	507.2	455.9	11.1	352	22.8	0.899	13.45	14.86	1.403	1.403	1.305
(b) Y Joints											
E1 ^b	507.2	455.9	11.1	352	22.8	0.899	14.96	18.70	1.200	1.595	1.452
E2 ^b	507.2	455.9	11.1	352	22.8	0.899	14.90	18.62	1.195	1.588	1.446
(c) K Joints											
C2-1, 90° ^b	507.2	326.4	11.1	352	22.8	0.644	5.83	7.04	1.122	1.122	0.917
30° ^b	507.2	455.9	11.1	352	22.8	0.899	12.31	15.39	0.987	1.312	1.195
C2-2, 90° ^b	507.2	326.4	11.1	352	22.8	0.644	8.32	10.06	1.602	1.602	1.309
30° ^b	507.2	455.9	11.1	352	22.8	0.899	14.67	18.33	1.177	1.564	1.424

Note: All tests are deformation controlled except BL-100-0.4. For column 10, the mean is 1.470, the standard deviation 0.353, and the coefficient of variation 24%. For column 11, the mean is 1.558, the standard deviation 0.302, and the coefficient of variation 19.4%. For column 12, the mean is 1.171, the standard deviation 0.179, and the coefficient of variation 15.3%.

^aFrom Ref. 20.

^bFrom Ref. 25.

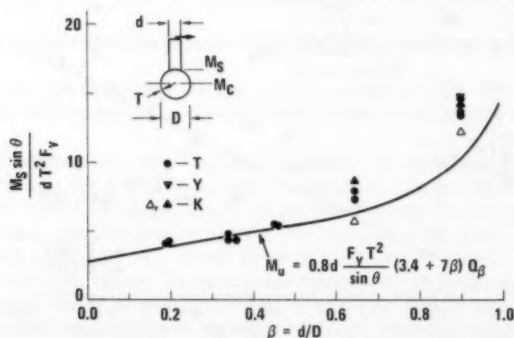


FIG. 10.—Out-of-Plane Bending Loading of T and K Joints

The results from 16 in-plane bending tests are summarized in Table 4. The loads on the two branches of the K joint are listed individually and were applied such that the branch moments opposed each other. The useful moment capacity at the chord surface is plotted in Fig. 9 as a function of β . There is significant scatter, but the lower bound follows the same trend as the axial compression data and is defined by

$$M_u = 0.8d \frac{F_y T^2}{\sin \theta} (3.4 + 19\beta) \dots \dots \dots (5)$$

Eq. 5 implies that the in-plane moment can be converted to an equivalent axial load by dividing the moment by $0.8d$, which is close to $0.785d$, the distance between the resultant tension and compressive forces on a tubular cross section with an elastic bending stress distribution. Gibstein suggested that the ultimate moment is related to $\sqrt{\gamma}$ in addition to β (8). However, the JSSC data do not follow the Gibstein trend, so the simple lower bound given by Eq. 5 is recommended.

Out-of-Plane Bending Data and Capacity Equation.—Test data from 17 branches subjected to out-of-plane bending loads are summarized in Table 5. The data cover a wide range of γ and β values, and include tests on T, Y, and K joint configurations. The Yura data provide replicate tests which established a test scatter of less than 10%.

In the K joint tests the branch shear loads were in the same direction. The maximum load in each branch at failure is recorded in Table 5 and shown in Fig. 10. In test C2-1, both branches failed simultaneously, with P_{30} equal to three times P_{90} . This test produced the lowest failure loads, as shown by the open data points. However, in test C2-2 the branches did not fail simultaneously, with P_{30} equal to one and one-half times P_{90} . Each branch showed an improved load capacity over the C2-1 test.

Despite the aforementioned K joint differences, it appears one equation can reasonably predict the lower bound joint capacity. The plot in Fig. 10 shows satisfactory representation by

$$M_u = 0.8d \frac{F_y T^2}{\sin \theta} (3.4 + 7\beta) Q_\beta \dots \dots \dots (6)$$

in which Q_β is defined in Eq. 3.

DATA ANALYSIS

The comparisons of test and theory listed in Tables 4 and 5 show that the API equations predict a lower bound to the data but are very conservative. Eqs. 5 and 6 also predict a lower bound, but with reduced scatter and greater reliability.

SUMMARY AND CONCLUSIONS

A reliable data base of 137 tests of tubular joints has been established and summarized. This base excludes data without measured material properties, section properties, deformation information, or fracture information. The base

also excludes tests with chord diameters less than 5.5 in. (140 mm) since scaling questions exist for smaller sizes.

The screened data base has been used to develop improved lower bound capacity formulas for a variety of joint and load configurations. These new equations are summarized in Fig. 11. One formula is recommended for both tension and compression in the branch of a K joint. This formula is identical to that for T and Y joints in tension and compression, except for the additional gap factor. Branch moment capacities can be converted to equivalent axial load capacities by dividing by 80% of the branch diameter.

The new equations and the API equations have been compared with the experimental results. The new equations consistently predict the lower bound with less scatter than the API equations. The 1977 API equation approximates roughly the mean of the T axial data, but is lower bound for joints with applied moment loading. Although the API prediction scatter is generally greater than for the new equations, the 1977 API equation shows distant improvement over the 1973 version.

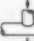
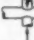
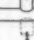
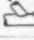
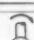
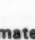
LOAD	JOINT	EQUATION
AXIAL COMPRESSION	 T, Y	$P_x = \frac{F_y T^2}{\sin \theta} (3.4 + 19\phi)$
	 DT, X	$P_x = \frac{F_y T^2}{\sin \theta} (3.4 + 13\phi) Q_\phi$
AXIAL TENSION	 T, Y, DT, X	$P_x = \frac{F_y T^2}{\sin \theta} (3.4 + 19\phi)$
AXIAL COMPRESSION AND TENSION	 K	$P_x = \frac{F_y T^2}{\sin \theta} (3.4 + 19\phi) Q_\phi$
IN-PLANE BENDING	 ALL JOINTS	$M_x = 0.8 d \frac{F_y T^2}{\sin \theta} (3.4 + 19\phi)$
OUT-OF-PLANE BENDING	 ALL JOINTS	$M_x = 0.8 d \frac{F_y T^2}{\sin \theta} (3.4 + 7\phi) Q_\phi$

FIG. 11.—Ultimate Capacity Equations for Tubular Joints

There are a number of questions which should be addressed prior to design implementation of the new equations. First, one or more safety factors should be established. With the new equations, one common safety factor becomes more realistic because the equations yield a constant level of performance (in this case lower bound) with a relatively constant degree of scatter. Second, load interaction should be considered. Some sort of interaction equation is required to predict joint capacity under combined branch loading. Also, the effect of load in the chord should be addressed (11,22). Until reliable test data are generated on the topics, it is suggested that the current API approaches for load interaction and chord load effects be used with the capacity equations developed herein.

APPENDIX.—REFERENCES

1. American Institute of Steel Construction, *Specification for the Design, Fabrication and Erection of Structural Steel for Buildings*, 7th ed., 1969.

2. American Petroleum Institute, *Recommended Practice for Planning, Designing and Constructing Fixed Offshore Platforms*, RP 2A, 4th ed., 1973, 9th ed., Nov., 1977.
3. Beale, L. A., and Toprac, A. A., "Analysis of In-Plane T, Y, and K Welded Tubular Connections," *Welding Research Council Bulletin* 125, New York, N.Y., Oct., 1967.
4. Bouwkamp, J. G., "Research on Tubular Connections in Structural Work," *Welding Research Council Bulletin* 71, New York, N.Y., Aug., 1961.
5. Bouwkamp, J. G., "Behavior of Tubular Truss Joints Under Static Loads," Phases I & II, University of California, Berkeley, Calif., July, 1965, Jan., 1968.
6. Brown and Root, Inc., "An Investigation of Welded Tubular Joints Loaded by Axial and Moment Loads," Offshore Structure Department, Job No. ER-0169, Houston, Tex., Feb., 1976.
7. Gibstein, M. B., "Static Strength of Tubular Joints," Det norske Veritas, *Report No. 73-86-C*, Oslo, Norway, May, 1973.
8. Gibstein, M. B., "The Static Strength of T-Joints Subjected to In-Plane Bending Moments," Det norske Veritas, *Report No. 76-137*, Oslo, Norway, July, 1976.
9. Grigory, S. C., "Experimental Determination of the Ultimate Strength of Tubular Joints," Southwest Research Institute, Project No. 03-3054, *Report to Humble Oil and Refining Co.*, San Antonio, Tex., Sept., 1971.
10. Kanatani, H., "Experimental Study on Welded Tubular Connections," *Memoirs of the Faculty of Engineering*, Kobe University, Vol. 14, No. 12, Kobe, Japan, 1966.
11. Marshall, P. W., and Toprac, A. A., "Basis for Tubular Joint Design," *Welding Journal*, Research Supplement, Vol. 53, No. 5, May, 1974, pp. 192-s-201-s.
12. Marshall, P. W., "A Review of American Criteria for Tubular Structures—and Proposed Revisions," International Institute of Welding, *Document XV-405-77*, London, 1977, Rev. March, 1978.
13. Mouty, J., "Calcul des Charges Ultimes des Assemblages Soudé de Profils Creux Carrés et Rectangulaires," *Construction Metallique*, Vol. 13, No. 2, 1976, pp. 37-58.
14. Nakajima, T., "Experimental Study on the Strength of Thin Wall Welded Tubular Joints," International Institute of Welding, *Document No. XV-312-71*, London, 1971.
15. Novikov, V., et al., "Direct Joining of Tubular Section Components," *Automatic Welding*, Vol. 9, 1959, pp. 61-68.
16. Pan, R. B., Plummer, F. B., and Kuang, J. G., "Ultimate Strength of Tubular Joints," *Journal of Petroleum Technology*, Vol. 29, No. 4, April, 1977, pp. 449-460.
17. Reber, J. B., "Ultimate Strength Design of Tubular Joints," *Journal of the Structural Division*, ASCE, Vol. 99, No. ST6, Proc. Paper 9793, June, 1973, pp. 1223-1240.
18. Sammet, H., "Die Festigkeit Knotenblechloser Rohrverbindungen im Stahlbau," (in German) *Schweisstechnik*, Vol. 13, 1963, pp. 481-485.
19. Sherman, D. R., and Marshall, P. W., "Commentary on the Static Design of Tubular Connections," Mtg. Preprint, ASCE National Convention, San Diego, Calif., April, 1976.
20. Society of Steel Construction of Japan, "Study on Tubular Joints Used for Marine Structures," March, 1972.
21. Toprac, A. A., Johnston, L. P., and Noel, J., "Welded Tubular Connections: An Investigation of Stresses in T-Joints," *Welding Journal*, Vol. 45, No. 1, Jan., 1966, pp. 1-s-12-s.
22. Washio, K., Togo, T., and Mitsui, Y., "Experimental Study on Tubular Cross Joints," (in Japanese) Architectural Institute of Japan, Kinki Branch, 1966.
23. Washio, K., Togo, T., and Mitsui, Y., "Experimental Study on Local Failure of Chords in Tubular Truss Joints," *Technology Reports of the Osaka University*, Vol. 18, Osaka, Japan, Oct., 1968, pp. 559-581.
24. Yura, J. A., Galambos, T. V., and Ravindra, M. K., "The Bending Resistance of Steel Beams," *Journal of the Structural Division*, ASCE, Vol. 104, No. ST9, Proc. Paper 14015, Sept., 1978, pp. 1355-1370.
25. Yura, J. A., Howell, L. E., and Frank, K. H., "Ultimate Load Tests on Tubular Connections," Civil Engineering Structures Research Laboratory, University of Texas, Report No. 78-1, *Report to Exxon Production Research Co.*, Austin, Tex., Sept., 1978.
26. Yura, J. A., Zettlemoyer, N., and Edwards, I., "Ultimate Capacity Equations for Tubular Joints," *OTC Paper No. 3690*, Proceedings, Offshore Technology Conference, May, 1980.

27. Zimmermann, W., "Tests on Panel Point Type Joints for Large Diameter Tubes," Otto Graf Inst., Stuttgart Tech. Hochschule, *Report to CIDECT Paris/London*, Stuttgart, Germany, Sept. 10, 1965.

VIBRATIONS OF CABLE-REINFORCED INFLATABLE STRUCTURES

By O. G. Vinogradov,¹ D. J. Malcolm,² A. M. ASCE
and P. G. Glockner,³ M. ASCE

INTRODUCTION

Due to the high flexibility of an air-supported structure, its equilibrium shape and associated external loading can be found only by considering the interaction between the structure and the loads, e.g., aeroelasticity in the case of wind load. As a step toward solving this complex interaction problem, the dynamic characteristics of air-supported structures under fixed external loads should be determined; progress towards this first goal has been limited (7), but such an analysis will itself be useful in design by showing the sensitivity of dynamic characteristics to different static loads and internal pressure.

The free and forced vibrations of an initially stressed membrane shell of revolution have been studied by Leonard (3) who found that the magnitude of the initial stress has a significant effect on the natural frequencies. A wind gust analysis of a cable reinforcing net for an air-supported dome is presented (6) in which the wind load has been considered as a static part plus small random fluctuations, and the spatial distribution of the wind pressure has been taken in accordance with data from tests on rigid domes (4). Ref. 6 is an interesting attempt to simulate the complex loading of the flexible structure.

The present paper deals with the dynamic characteristics of cable-reinforced inflatable caps and the influence of internal pressure and static loads on these characteristics. The results presented are based on a numerical method, with corresponding computer code, developed for the nonlinear static and small forced oscillation analysis of arbitrary cable-reinforced air-supported structures.

The inflatable cable-reinforced structure is modeled by a cable network with the action of the membrane neglected, except for transmitting the pressure load to the cables. The pressure load is considered as distributed along cable elements while all other loads, including inertia forces in the dynamic problem,

¹Asst. Prof., Dept. of Mech. Engrg., The Univ. of Calgary, Calgary, Alberta, Canada.

²Assoc. Prof., Dept. of Mech. Engrg., The Univ. of Calgary, Calgary, Alberta, Canada.

³Prof. and Head, Dept. of Mech. Engrg., The Univ. of Calgary, Calgary, Alberta, Canada.

Note.—Discussion open until March 1, 1982. To extend the closing date one month, a written request must be filed with the Manager of Technical and Professional Publications, ASCE. Manuscript was submitted for review for possible publication on July 11, 1980. This paper is part of the Journal of the Structural Division, Proceedings of the American Society of Civil Engineers, ©ASCE, Vol. 107, No. ST10, October, 1981. ISSN 0044-8001/81/0010-1985/\$01.00.

are concentrated at nodes. It is assumed that cables can be divided into segments in such a way that each is loaded by a uniform pressure line-load lying in one plane. For structures subjected to internal pressure, plus a smoothly varying wind load, this decomposition can always be performed by increasing the number of elements sufficiently to approximate any pressure loading. The equilibrium of each segment under the uniform plane pressure line-load is described by a simple nonlinear algebraic equation. Another advantage is that the finite element stiffness matrix can be derived for this type of segment in closed form.

The cables are considered as elastic elements undergoing large displacements. It is assumed that the change in shape of the structure does not influence the magnitude of the external pressure load. Under these assumptions the geometric nonlinear static problem is reduced to the determination of the equilibrium shape of the structure under the given load. In the program, the relaxation technique is used, and to ensure convergence of the iterative procedure, an additional condition of "virtual shapes" is introduced.

When the equilibrium shape of the structure, and the corresponding stiffness matrix are known, the small, forced oscillations are investigated by transforming the static stiffness matrix into the dynamic complex stiffness matrix, including inertia terms from concentrated masses.

The method of assembling the overall structural stiffness matrix at each cycle is based on that used in the SAP IV computer program (1), in which the position of non-zero elements in the overall structure stiffness matrix is noted and is used in the solution of the linear equations.

The numerical analysis has been applied to a spherical membrane cap comprised of two meridional reinforcing cables lying in mutually orthogonal vertical planes and having 3 degrees of freedom, and a spherical cap comprising 14 reinforcing cables lying along geodesic lines and having 147 degrees of freedom. Strong interdependence has been found between internal pressure, static load, and dynamic response of these structures.

Some of the results presented here were discussed at the 1980 Spring Convention of the ASCE (8).

CABLE SEGMENT AND STIFFNESS MATRIX

The cable segment shown in Fig. 1 is restrained against displacement at ends 1 and 2, and is in equilibrium under the plane uniform pressure, p , and end

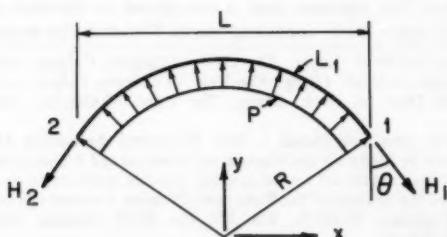


FIG. 1.—Cable Segment Under Uniform Pressure

forces $H_1 = H_2 = H = pR$. The elastic elongation, ΔL_1 , of a segment is

$$\Delta L_1 = \frac{HL_1}{EA} \quad (1)$$

in which L_1 = unstretched length, and EA = axial stiffness of the cable. It follows from the geometry of Fig. 1 that

$$2 \left(\frac{\pi}{2} - \theta \right) R = L_1 + \Delta L_1 \quad (2)$$

in which R = radius of curvature of the cable. Using the relationship

$$R = 0.5 \frac{L}{\cos \theta} \quad (3)$$

in which L = the span of the cable, the following equation may be obtained for the unknown angle, θ ,

$$\theta + e \cos \theta = \frac{\pi}{2} - \xi \quad (4)$$

in which $e = L_1/L$ and $\xi = 0.5 p L_1/EA$. The stiffness of the element in the deformed configuration is found by considering changes in end forces due to small end displacements and results (Appendix I) in

$$K = \frac{p}{2 \cos \theta} \begin{bmatrix} d & -d \\ -d & d \end{bmatrix} \quad (5)$$

$$\text{in which } d = \begin{bmatrix} \mu \sin \theta & +\cos \theta \\ -\cos \theta & \sin \theta \end{bmatrix} \quad (6)$$

$$\text{and } \mu = 1 + \frac{e}{\sin \theta (1 - e \sin \theta)} \quad (7)$$

Note that the stiffness matrix is proportional to the pressure load, p , and is a function of the current values of θ and e .

NONLINEAR STATIC PROBLEM

The solution of the nonlinear static problem is found by the relaxation method. Using the linearized structure stiffness matrix and residual nodal load forces as external forces, the coordinates for each node at step $j+1$ are found as

$$x_i^{j+1} = x_i^j + \lambda^j u_i^j \quad (8)$$

in which u_i^j = the coordinate increments or displacements;

$$\lambda^j = \begin{bmatrix} 1 & e' > 1 \\ \alpha < 1 & e' < 1 \end{bmatrix};$$

$i = 1, 2, 3$; and $j = 0, 1, 2 \dots$ and

$$e' = \frac{\text{length of the segment in previous step}}{\text{span of the segment in new step}} \quad (9)$$

The computation is continued until the residual force vector becomes insignificant. The process may fail to converge if the difference between the initial and final geometry is too large at any one step. If this occurs, then a value of $\lambda' = \alpha < 1$ should be chosen in Eq. 8 so that displacements will be small at this step. Applying this method of relaxation coefficient adjustment to cables subjected to pressure loading is equivalent to requiring convexity of the cable segment at each step, i.e., $e' > 1$. If this condition is not satisfied, λ' must be reduced and the step repeated. This procedure ensures convergence of the iterative process for any initial geometry with unstretched cables.

FORCED VIBRATIONS

Consider small oscillations with respect to the static equilibrium shape and assume all masses concentrated at the nodes.

The algebraic system describing small vibrations is obtained, according to the correspondence principle (2), by substitution of the complex moduli of elasticity

$$E^* = E \exp(i\delta) \quad (10)$$

into equations describing static equilibrium, and by adding inertia forces

$$f = -m\omega^2 v \quad (11)$$

in which $\delta = \gamma/\pi$; γ = logarithmic decrement of the material; m = mass; ω = circular frequency; and v = amplitude of vibration. For quasi-elastic materials in a relatively narrow frequency range, the real and imaginary terms of the complex moduli can be taken as frequency independent. Using a complex modulus in Eq. 4, θ becomes complex:

$$\theta^* + e \cos \theta^* = \frac{\pi}{2} - \xi \exp(-i\delta) \quad (12)$$

in which $\theta^* = \theta + i\theta_1$; and $i = \sqrt{-1}$

For quasi-elastic materials with small δ , and after separation of real and imaginary terms, Eq. 12 yields

$$\theta + e \cos \theta = \frac{\pi}{2} - \xi \quad (13)$$

$$\theta_1 - e \sin \theta \theta_1 = \xi \delta \quad (14)$$

The real part of θ^* is, therefore, expressed by Eq. 4 where the value of θ is known from the static analysis, and the imaginary part of θ^* is given through Eq. 14. The substitution $\theta = \theta^*$ transforms the static stiffness matrix, \mathbf{K} (Eq. 5), into the complex stiffness matrix, \mathbf{K}^* , which is transformed into the dynamic complex stiffness matrix by adding the inertia stiffness of the concentrated masses, $-m\omega^2$, to corresponding diagonal elements. External dynamic forces are also considered as complex in order to describe the phase shift.

COMPUTER PROGRAM

The FORTRAN computer program consists of two parts: (1) The solution of the nonlinear static problem; and (2) the determination of amplitudes and phases of small vibrations. The switch to the second part occurs when the condition

$$\frac{\text{norm of residual vector}}{\text{norm of node force vector}} \leq \delta_f \ll 1 \dots \dots \dots (15)$$

is satisfied.

The effectiveness of the program depends mainly on the effectiveness of its static part because it contains two kinds of iterative processes: (1) The solution of Eq. 4 for the cable segment; and (2) finding the equilibrium shape of the overall structure.

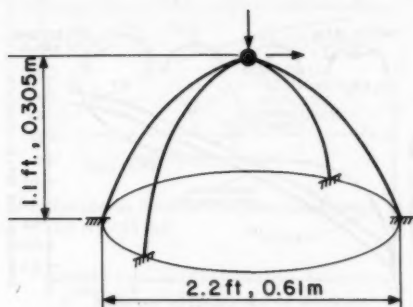


FIG. 2.—Two-Cable Reinforcement of Spherical Cap, ($EA = 20.6 \text{ kN} = 4.6 \times 10^3 \text{ lbf}$)

Eq. 4 is solved by the Newton-Raphson method with an initial value of θ equal to

$$\theta_0 = \frac{\pi^2}{8e} - \frac{\pi}{2} \left[\left(\frac{\pi}{4e} - 1 \right)^2 + \frac{\xi}{e} \right]^{1/2} \dots \dots \dots (16)$$

which is based on a half-sine-wave approximation and ensures convergence to within 5% of the correct shape after 2-4 cycles.

The initial geometry of the structure was taken as that of the structure, under small internal uniform pressure, without concentrated loads. To ensure convergence, the coefficient λ' was taken to be equal to 0.5 if the condition of Eq. 9 was not satisfied. For the following structures (Figs. 2 and 7) 3-5 iterations were needed for a value of $\delta_f = 0.25 \times 10^{-5}$.

Execution times on the University of Calgary's Honeywell DPS level 2 Computer System were 1 sec/iteration for the structure with 60 cable segments (Fig. 7). Calculations of amplitudes and phases of vibrations for the same structure, with 77 degrees of freedom, required 1.6 sec/frequency.

NUMERICAL RESULTS

Two spherical caps, one having two and the other 14 reinforcing cables, were analyzed numerically. Results for the first structure were compared with exact results, while some of the results for the second structure were compared with corresponding data for the static case (5).

Spherical Membrane Cap with Two Reinforcing Cables.—If the change in shape due to the change in internal pressure is negligible, then the natural frequencies are proportional to the square root of the pressure

$$f \sim p^{1/2} \quad (17)$$

Because the segment and, thus, the overall stiffness matrix is directly proportional to the internal pressure, it follows that the eigenvalues of this matrix are also proportional to the internal pressure and, therefore, the natural frequencies are proportional to the square root of this variable.

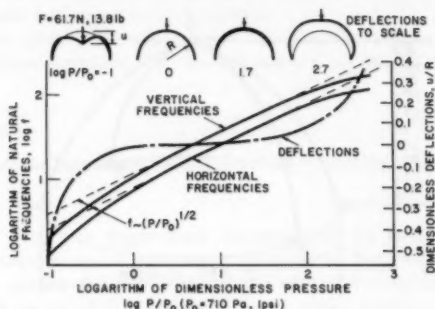


FIG. 3.—Log Natural Frequencies Versus Log Dimensionless Internal Pressure for Two-Cable Spherical Cap

The results presented in Fig. 3 confirm this relationship for the two-cable reinforced spherical cap over a wide range of pressures. However, for small values of p , when the displacements under the static load are large, and also for large values of the pressure when elastic elongations are large, again resulting in large displacements, the deviation of the real horizontal and vertical natural frequencies (solid lines), from those described by Eq. 17 (broken lines), becomes significant. The zones of deviation coincide with those where the deflections from the initially spherical shape are large (Fig. 3). There is, therefore, a range of internal pressures in which the natural frequencies can be considered as proportional to the square root of the magnitude of internal pressure. The width of this range depends on the stiffness of the cables and decreases with decreasing cable tensions.

Fig. 4 shows the effect, to scale, of vertical concentrated static loads, such as snow and water, on the change in shape of the structure. The relationship between the change of shape and change of resonant frequencies can be read from Fig. 4, using points on the stiffness curve as reference points. As can

be seen from the diagram, the relationship between force and natural frequencies is nonlinear. For relatively small changes in shape ($u/R \leq 0.15$), it may be approximated by a straight line so that a decrease in natural frequencies becomes proportional to the displacements or the forces.

Fig. 5 shows results for a horizontally applied static load. These results demonstrate a reversed influence, in which stiffness and natural frequency increase with load and displacement. For small displacements ($u/R \leq 0.15$), this relationship can also be approximated by a linear one.

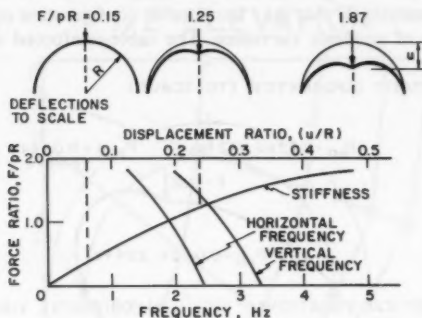


FIG. 4.—Vertical and Horizontal Natural Frequencies Versus Shape for Two-Cable Spherical Cap, ($pR = 33.6$ N, 7.55 lbf)

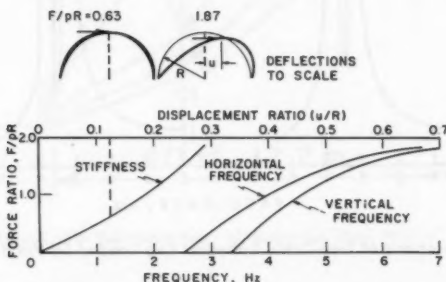


FIG. 5.—Vertical and Horizontal Natural Frequencies Versus Shape for Two-Cable Spherical Cap, ($pR = 33.6$ N, 7.55 lbf)

Under real loading conditions, the spectrum of wind load comprises low frequencies, which may be considered as an equivalent static pressure, as well as high frequencies. Under the action of slowly applied static forces, a structure undergoes changes of shape and corresponding changes in its dynamic response which may differ significantly from the response in the undeformed configuration. It is important, therefore, to check for any overlap between the spectrum of wind loading frequencies and that of the structure in the displaced configuration.

The case of wind pressure, and static vertical load acting simultaneously, is shown in Fig. 6 (to scale). Note that the static concentrated load increases the effect of the static wind pressure on the dynamic response of the structure, because the stiffness of the structure depends on its shape and pressure. Under wind loading, both of these parameters are affected. The existence of two peaks in the diagrams of Fig. 6 is a result of interaction between vertical and horizontal vibrations at corresponding resonant frequencies due to the unsymmetrical shape of the deformed structure.

Spherical Membrane Cap with 14 Reinforcing Cables.—It was found from previous static analysis (5) that the "best" cable configuration consists of cables that follow lines of geodesic curvature. The cable-reinforced structure shown

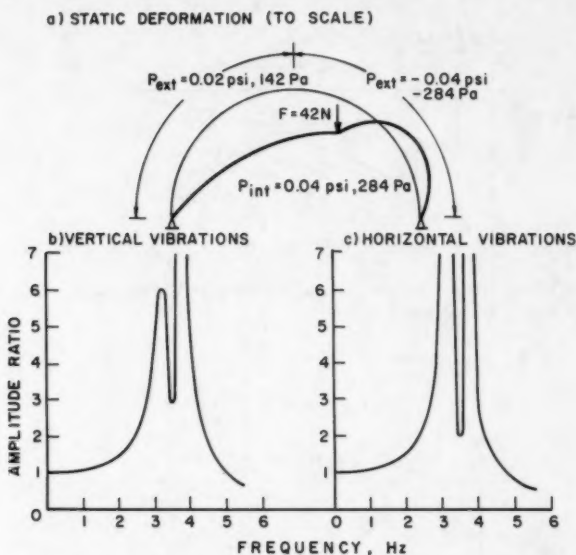


FIG. 6.—Vibrations of Two-Cable Spherical Cap Loaded by Wind Pressure

in Fig. 7 has cables coinciding with geodesic lines and has the same dimensions as that used in Ref. 5.

The static load has been taken as the dead weight of cables applied at nodes. The mass of each cable is also concentrated at nodes, and due to symmetry, all calculations are done for one-half the structure, comprising 60 cable segments and 28 masses. The dynamic characteristics of this structure were analyzed to demonstrate the influence of internal pressure and wind on natural frequencies, and to obtain the spectrum of vertical and horizontal vibrations. A unit harmonic force is applied at the apex of the cap (Fig. 7) in the vertical and horizontal directions, independently.

Fig. 8 shows the relationship between internal pressure and the first three

natural frequencies. The results of the analysis (solid lines) do not correspond exactly to those predicted by Eq. 17 (dotted lines), the reason being the same as for the two-cable reinforced membrane. The smaller the internal pressure, the larger the change in shape due to the static load. As the internal pressure increases and the importance of dead weight diminishes, the results approach those given by Eq. 17. Deviation from those results will also occur if the elastic extension of the cables is sufficient to change the undeformed geometry appreciably.

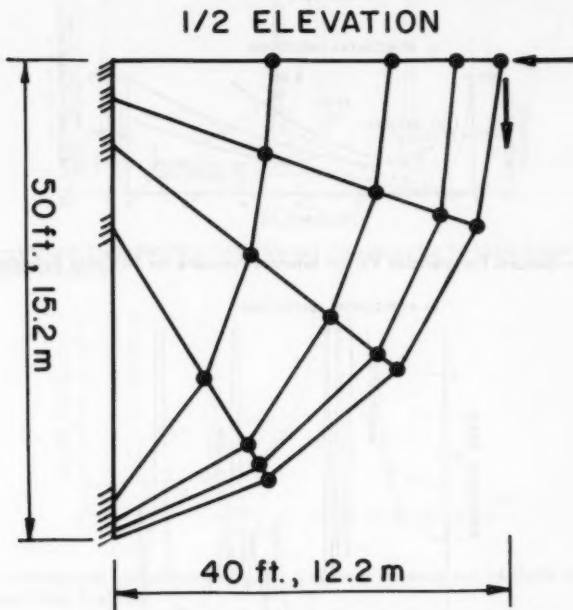


FIG. 7.—Fourteen-Cable Reinforcement of Spherical Cap, ($EA = 13.3 \times 10^4 \text{ kN} = 3 \times 10^4 \text{ lbf}$)

An example of the dynamic response of a spherical cap under an internal pressure of 0.4 in. (96 Pa) of water, is presented in Fig. 9. It can be seen that natural frequencies in the vertical direction are close to each other and are distributed in groups. The resonances would not be so sharp if acoustic damping and corresponding added masses had been included. As a result of relatively small material damping ($\delta = 0.01$), the interaction between vertical and horizontal vibrations at resonance have become significant.

In order to estimate the influence of the static part of the wind load on the dynamic characteristics of the cap, an idealized wind pressure of $\pm 3.8 \text{ lb/sq ft}$ (182 Pa) plus corresponding to the leeward side, minus to the windward side) was applied to the structure with an internal pressure of 4.3 lb/sq ft

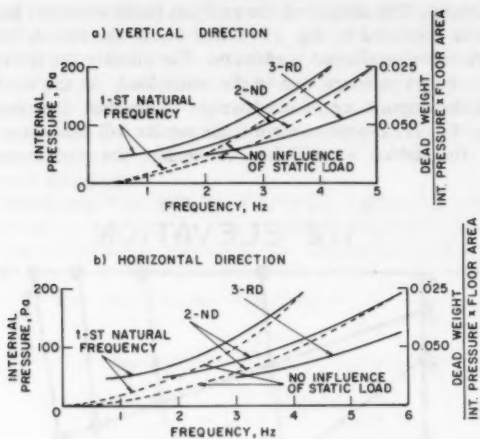


FIG. 8.—Natural Frequencies Versus Internal Pressure for 14-Cable Spherical Cap

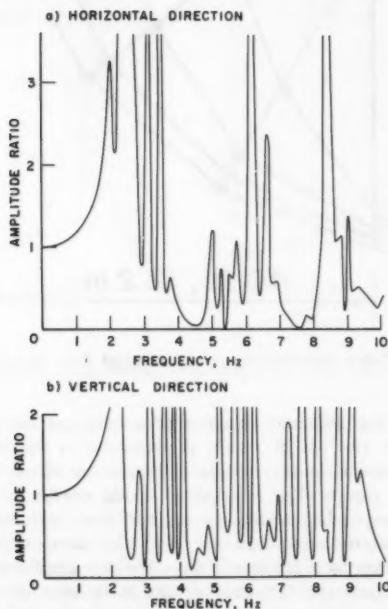


FIG. 9.—Magnification Factor Versus Frequency for 14-Cable Spherical Cap Under Internal Pressure $96 \text{ Pa} = 2 \text{ lb/ft}^2$

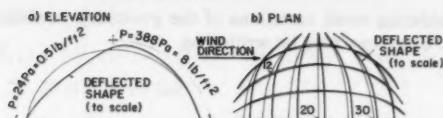


FIG. 10.—Effect of Idealized Wind Pressure on 14-Cable Spherical Cap

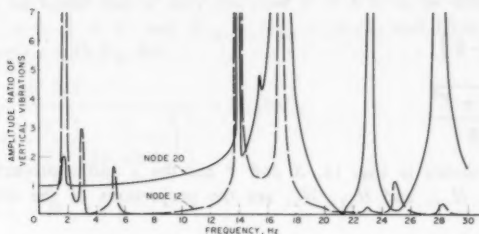


FIG. 11.—Vertical Magnification Factor Versus Frequency for 14-Cable Spherical Cap Under Wind Pressure

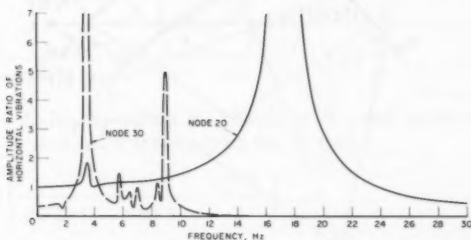


FIG. 12.—Horizontal Magnification Factor Versus Frequency for 14-Cable Spherical Cap Under Wind Pressure

(206 Pa). The deflected shape is shown in Fig. 10. The amplitude versus frequency curves are shown in Figs. 11 and 12 for the vertical and horizontal directions, respectively. The oscillating unit load was applied at node 20 (Fig. 10). It can be seen that some nodes have resonance frequencies lower than that of node 20.

In general, the response of the structure differs considerably from that without wind load, the reason being that wind load changes the pressure distribution on the structure as a result of which some cable segments experience higher pressures, while on others the load is decreased. Thus cable forces are redistributed throughout the structure affecting the natural frequencies of all cable elements, even though the change in shape of the structure may be insignificant.

FINITE ELEMENT STIFFNESS MATRIX

The stiffness matrix for the uniform pressure-loaded cable element may be

obtained by considering small variations of the governing nonlinear equilibrium equations. These equations may be written as

$$H_{2X} = H_{1X} - pY \quad (18)$$

$$H_{2Y} = pX - H_{1Y} \quad (19)$$

$$H^2 = H_{1X}^2 + H_{1Y}^2 = H_{2X}^2 + H_{2Y}^2 \quad (20)$$

$$H = pR \quad (21)$$

$$L_1 = 2R \left(\frac{\pi}{2} - \theta \right) \quad (22)$$

$$\cos \theta = \frac{\sqrt{X^2 + Y^2}}{2R} \quad (23)$$

in which, as shown in Fig. 13, X and Y are the x and y projections of the span L ; H_{1X} , H_{1Y} , and H_{2X} , H_{2Y} are the projections of the cable tension

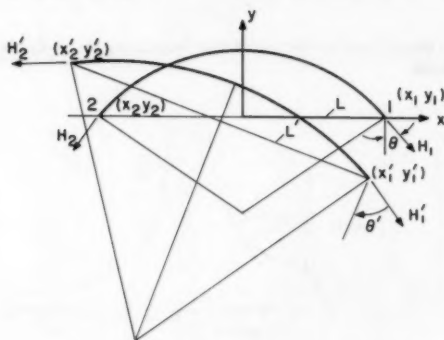


FIG. 13.—On Derivation of Finite Element Stiffness Matrix

H at ends 1 and 2 in the x and y directions, respectively. In general, variation changes in values of X , Y , R , H_{1X} , H_{2X} , H_{1Y} and H_{2Y} are considered, and from Eqs. 18-23 there results

$$\delta H_{2X} = \delta H_{1X} - p \delta Y \quad (24)$$

$$\delta H_{2Y} = p \delta X - \delta H_{1Y} \quad (25)$$

$$H \delta H = H_{1X} \delta H_{1X} + H_{1Y} \delta H_{1Y} = H_{2X} \delta H_{2X} + H_{2Y} \delta H_{2Y} \quad (26)$$

$$\delta H = p \delta R \quad (27)$$

$$0 = \delta R \left(\frac{\pi}{2} - \theta \right) - R \delta \theta \quad (28)$$

$$\delta \theta \sin \theta = \frac{L}{2R} \left(\frac{X \delta X + Y \delta Y}{L^2} - \frac{\delta R}{R} \right) \quad (29)$$

From Eqs. 24-26 one obtains

$$\delta H_{1Y}(H_{1Y} + H_{2Y}) = \delta H_{1X}(H_{2X} - H_{1X}) + p(H_{2Y}\delta X - H_{2X}\delta Y) \quad (30)$$

and from Eqs. 27-29 it follows that

$$\delta H \left(\frac{\pi}{2} - \theta - \frac{L}{2R \sin \theta} \right) = -\frac{p}{2 \sin \theta} (X\delta X + Y\delta Y) \quad (31)$$

It may now be noted that if only the case $Y = 0$ is to be considered, then $H_{2X} - H_{1X} = 0$, $X = L$, and $H_{1Y} = H_{2Y} = pL/2$, and from Eqs. 30 and 31 in conjunction with Eq. 26:

$$\frac{HpL\Delta X}{\left[2L \sin \theta \left(\theta - \frac{\pi}{2} + \frac{L}{2R \sin \theta} \right) \right]} = H_{1X}\delta H_{1X} + \frac{p}{2} \left(\frac{pL\Delta X}{2} - H_{1X}\Delta Y \right) \quad (32)$$

If Eqs. 21, 22, 23 and the relation $H_{1X} = H \sin \theta$ are used, then Eq. 32 becomes

$$\frac{p\delta X}{4 \cos^2 \theta (1 - e \sin \theta)} = \tan \theta \frac{\left(\delta H_{1X} - \frac{p}{2} \delta Y \right)}{2} + p\delta \frac{X}{4} \quad (33)$$

in which $e = L_1/L$. To obtain the change in H_{1X} due to an x -displacement, only $\delta Y = 0$ is used and it follows from Eq. 33 that

$$\delta H_{1X} = p\delta X \left(\frac{1}{\sin 2\theta (1 - e \sin \theta)} - \frac{\cot \theta}{2} \right) \quad (34)$$

substituting $\delta X = 0$, one obtains

$$\delta H_{1X} = \frac{p\delta Y}{2} \quad (35)$$

Using Eqs. 24-26 to remove δH_{1X} , δH_{2X} and δH_{2Y} , a similar procedure will result in the following influence of a y -only displacement

$$\delta H_{1Y} = \frac{p}{2} \tan \theta \delta Y \quad (36)$$

The complete stiffness matrix (Fig. 13) may now be written with the assistance of the reciprocal theorem as

$$\begin{Bmatrix} \delta H_{1X} \\ \delta H_{1Y} \\ \delta H_{2X} \\ \delta H_{2Y} \end{Bmatrix} = \frac{P}{2 \cos \theta} \begin{bmatrix} d & -d \\ -d & d \end{bmatrix} \begin{Bmatrix} \delta X_1 \\ \delta Y_1 \\ \delta X_2 \\ \delta Y_2 \end{Bmatrix} \quad (37)$$

$$\text{in which } \mathbf{d} = \begin{bmatrix} \mu \sin \theta & +\cos \theta \\ -\cos \theta & \sin \theta \end{bmatrix} \dots \dots \dots (38)$$

$$\text{and } \mu = 1 + \frac{e}{\sin \theta (1 - e \sin \theta)} \dots \dots \dots (39)$$

CONCLUSIONS

It is shown that the dynamic characteristics of air-supported structures are strongly dependent on internal pressure and static loads, including equivalent static wind pressure. For the relatively small static loads, e.g., snow and dead weight, the changes in natural frequencies can be considered as proportional to the square root of the internal pressure. The influence of an idealized static wind-type load is to decrease the fundamental frequency of the structure.

ACKNOWLEDGMENTS

The financial assistance provided by the Natural Sciences and Engineering Research Council of Canada in the form of a strategic grant No. G-0106, and operating grant No. A-2736, is gratefully acknowledged.

APPENDIX I.—REFERENCES

1. Bathe, K. J., Wilson, E. L., *Numerical Methods in Finite Element Analysis*, Prentice-Hall, Inc., Englewood Cliffs, N.J., 1976.
2. Christensen, R. M., *Theory of Viscoelasticity*, Academic Press, New York, N.Y., 1971.
3. Leonard, J. W., "Dynamic Response of Initially-Stressed Membrane Shells," *Journal of the Engineering Mechanics Division*, ASCE, Vol. 95, No. EM5, Proc. Paper 6859, Oct., 1969, pp. 1231-1253.
4. Maher, F. J., "Wind Loads on Dome-Cylinder and Dome-Cone Shapes," *Journal of the Structural Division*, ASCE, Vol. 92, No. ST5, Proc. Paper 4933, Oct., 1966, pp. 79-96.
5. Malcolm, D. J. and Glockner, P. G., "Optimum Cable Configuration for Air-Supported Structures," *Journal of the Structural Division*, ASCE, Vol. 105, No. ST2, Feb., 1979, pp. 421-435.
6. Morris, N. F., "Wind Effects on Air-Supported Structures," presented at the April 25-29, 1977, ASCE Spring Convention and Exhibit, held at Dallas, Tex. (Preprint 2860).
7. "State-of-the-Art Report on Air-Supported Structures," Task Committee on Air-Supported Structures of the Committee on Metals, of the Structural Division, ASCE, 1979.
8. Vinogradov, O. G., Malcolm, D. J., "Dynamic Response (Finite Element Approach) of Cable Reinforced Inflatables," presented at the April 14-18, 1980, ASCE Spring Convention and Exhibit held at Portland, Oreg., (Preprint 80-101).

APPENDIX II.—NOTATION

The following symbols are used in this paper:

- A = cross-sectional area of cable;
 E = modulus of elasticity;

- E^* = complex modulus of elasticity;
 f = inertia force;
 H = tension force;
 H_1, H_2 = cable segment end forces;
 K = finite element stiffness matrix;
 L_1 = unstretched length of cable segment;
 L = span of cable segment;
 m = mass;
 p = internal pressure;
 R = radius of curvature of cable segment;
 u = static displacements;
 v = amplitude of vibration;
 X_i, Y_i = local coordinates of ends of cable segment ($i = 1, 2$);
 γ = logarithmic decrement of material;
 ΔL_1 = elongation of segment;
 $\delta X_i, \delta Y_i$ = increments of displacements of cable segment ends ($i = 1, 2$);
 $\delta H_{ix}, \delta H_{iy}$ = increments of end forces of cable segment ($i = 1, 2$);
 θ = angle (Fig. 1);
 $\theta^* = \theta + i\theta_1$ = complex angle; and
 ω = circular frequency.

PARAMETER STUDY OF OUTRIGGER-BRACED TALL BUILDING STRUCTURES

By B. Stafford Smith¹ and Irawan Salim²

INTRODUCTION

An outrigger-braced tall building structure consists of a stiff core, comprised of shear walls or a braced steel frame in the center of the building, connected to exterior columns by flexurally stiff cantilevers at one or more levels, as shown diagrammatically in Fig. 1(a).

To the best of the author's knowledge, this bracing arrangement was first used by Barbacki in 1962 in the design of the 47-story Place Victoria Building in Montreal (1). It has since been the basis of design for many other tall buildings of a similar size, in both steel and reinforced concrete framing.

When lateral loading acts on the structure, the outriggers and columns resist the rotation of the core and hence reduce the drift and the base moment that would have resulted in a free-standing core Figs. 1(b) and 1(c). Outrigger bracing is one of the most efficient and economic systems for controlling drift in tall buildings: the core and columns are obviously necessary components of the structure while the additional elements, the outriggers, are usually incorporated within the plant levels and, therefore, interfere only minimally with the usable space of the building.

The magnitude of the reduction in drift and core moment depends on the relative flexural rigidities of the core, the outriggers, and the columns acting axially about the centroid of the core. The amounts of reduction also depend on the location of the outriggers within the height of the core.

Previous studies of the problem have assumed the outriggers to be flexurally rigid. Taranath (2) investigated one-outrigger structures and showed that the optimum location of an outrigger is close to the mid-height of the building, (0.455 of the total height, from the top). McNabb and Muvdi (3) verified Taranath's result for a one-outrigger structure and showed that the optimum locations for two outriggers are 0.312 and 0.685 of the total height from the top. Stafford Smith and Nwaka's study (4) produced generalized results for the optimum

¹Prof., Dept. of Civ. Engrg. and Applied Mechanics, McGill Univ., MacDonald Engrg. Building, 817 Sherbrooke St. West, Montreal, Canada.

²Canatom Ltd., Montreal, Canada.

Note.—Discussion open until March 1, 1982. To extend the closing date one month, a written request must be filed with the Manager of Technical and Professional Publications, ASCE. Manuscript was submitted for review for possible publication on August 8, 1980. This paper is part of the Journal of the Structural Division, Proceedings of the American Society of Civil Engineers, ©ASCE, Vol. 107, No. ST10, October, 1981. ISSN 0044-8001/81/0010-2001/\$01.00.

locations in multi-outrigger structures for any number of outriggers. They showed that if the outriggers are located at equidistant height intervals, but excluding, one at the top of the structure, a close to optimum reduction in drift is achieved.

In each of the above investigations, the assumption of flexurally rigid outriggers was adopted to simplify the solution of the problem. It was noted, however, that the flexibility of the outriggers would have an influence on the total drift and the core moment as well as on the optimum location of the outriggers for the maximum reduction in drift. In this paper, the results of an investigation of multi-outrigger structures with flexible outriggers are presented (5). Generalized equations are derived that allow the optimum locations of the outriggers and the magnitude of drift and reduction in core moment to be estimated. The equations developed for the solution of the optimum locations are too complex for direct practical use, involving higher orders of polynomials and necessitating a computer solution; therefore, graphical solutions are presented. These allow rapid manual solutions for multi-outrigger structures, within the constraints of the assumptions.

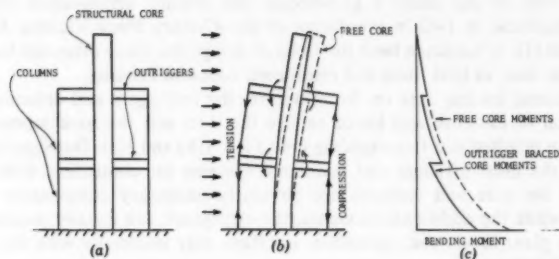


FIG. 1.—(a) Outrigger-Braced Structure; (b) Response to Lateral Loading; and (c) Resultant Bending Moment in Core

In practical structures, the size of cores and columns usually reduce up the height of the building; thus, the results for a uniform structure, as assumed here, cannot be applied exactly. Therefore, the results of the study are useful primarily as guidelines for estimating member sizes in the preliminary stages of design. When the exact sizes and locations of the components have been decided, a stiffness computer analysis should be used to provide a more accurate check on drift and member actions.

METHOD OF ANALYSIS

Assumptions.—The development of the analysis is based on the following simplifying assumptions: (1) The structure behaves linear elastically; (2) only axial forces are induced in the columns; (3) the outriggers are rigidly attached to the core, and the core is rigidly cantilevered from the base; (4) the sectional properties of the core, columns, and outriggers are uniform throughout the height; and (5) the distribution of wind loading is uniform over the height.

The validity of the member property assumptions for a structure under

consideration will depend upon the material of construction and the features of design. Assumption 4 is less restrictive than it might, at first, appear. Although, in a practical structure, the inertia of the core and sectional areas of the columns reduce the height, the results of concern in a preliminary analysis, i.e., the top drift, the core base moment, and the column axial forces are dominated by the structural properties in the lowest region. Therefore, a uniform analysis,

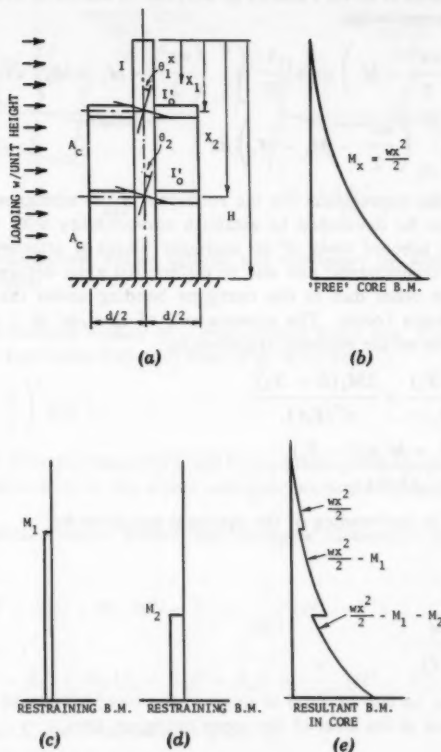


FIG. 2.—(a) Structure Dimensions; (b) External Loading Bending Moment Diagram; (c) Restraining Moment Due to Outrigger 1; (d) Restraining Moment Due to Outrigger 2; (e) Resultant Bending Moment in Core

using the sizes of core, columns, and outrigger in the lowest region, will give results acceptable for preliminary design purposes.

Compatibility Equations for Two-Outrigger Structures.—A two-outrigger structure will be used to demonstrate the method of analysis. The analysis of single or other multi-outrigger structures can be developed easily from the two-outrigger case. Compatibility equations will be developed for the rotation of the core

and outriggers at the outrigger levels Fig. 2(a). The bending moment diagram for the core consists of the free bending moment diagram due to the externally applied load Fig. 2(b) reduced by the outrigger restraining moments, which extend uniformly from the corresponding outrigger level to the base Fig. 2(c) and 2(d). The resulting bending moment diagram is, therefore, a stepped version of the original free moment diagram Fig. 2(e).

The core rotations at levels 1 and 2 Fig. 2(a) can be shown by the moment-area method to be, respectively.

$$\theta_1 = \frac{1}{EI} \int_{x_1}^{x_2} \left(\frac{wx^2}{2} - M_1 \right) dx + \frac{1}{EI} \int_{x_2}^H \left(\frac{wx^2}{2} - M_1 - M_2 \right) dx \dots \dots (1a)$$

$$\text{and } \theta_2 = \frac{1}{EI} \int_{x_2}^H \left(\frac{wx^2}{2} - M_1 - M_2 \right) dx \dots \dots \dots (1b)$$

The corresponding expressions for the rotations of the outriggers at locations 1 and 2 will now be developed to establish compatibility with the core. The rotations of the inboard ends of an outrigger where it attaches to the core consists of two components, one due to differential axial deformations of the columns and the other due to the outrigger bending under the action at its ends of the column forces. The components of rotation at 1 and 2 due to axial deformations of the columns are given by

$$\theta_{a1} = \frac{2M_1(H - X_1)}{d^2(EA)_c} + \frac{2M_2(H - X_2)}{d^2(EA)_c} \dots \dots \dots (2a)$$

$$\text{and } \theta_{a2} = \frac{2(M_1 + M_2)(H - X_2)}{d^2(EA)_c} \dots \dots \dots (2b)$$

while those due to the bending of the outrigger are given by

$$\theta_{b1} = \frac{M_1 d}{12(EI)_o} \dots \dots \dots (3a)$$

$$\text{and } \theta_{b2} = \frac{M_2 d}{12(EI)_o} \dots \dots \dots (3b)$$

Eqs. 1a, 2a, and 3a can be used to express the compatibility of the core and outrigger rotations at the level of the upper outrigger, thus

$$\begin{aligned} \theta_{a1} + \theta_{b1} &= \theta_1 \\ \frac{2M_1(H - X_1)}{d^2(EA)_c} + \frac{2M_2(H - X_2)}{d^2(EA)_c} + \frac{M_1 d}{12(EI)_o} \\ &= \frac{1}{EI} \left[\int_{x_1}^{x_2} \left(\frac{wx^2}{2} - M_1 \right) dx + \int_{x_2}^H \left(\frac{wx^2}{2} - M_1 - M_2 \right) dx \right] \dots \dots \dots (4a) \end{aligned}$$

and Eqs. 1b, 2b, and 3b for compatibility of rotations at the level of the lower outriggers

$$\theta_{a2} + \theta_{b2} = \theta_2$$

$$\frac{2(M_1 + M_2)(H - X_2)}{d^2(EA)_c} + \frac{M_2 d}{12(EI)_o} = \frac{1}{EI} \int_{x_2}^H \left(\frac{wx^2}{2} - M_1 - M_2 \right) dx \dots (4b)$$

It should be noted that $(EI)_o$ is the effective flexural rigidity of the outrigger, as though its length extended from the column to the centroid of the core. $(EI)_o$ can be found from the actual flexural rigidity of the outrigger $(EI')_o$ by

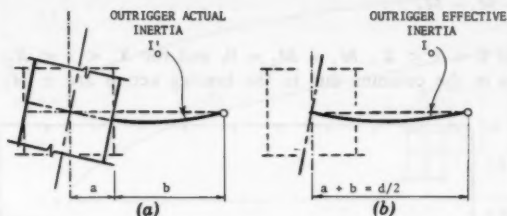


FIG. 3.—(a) Wide-column Action of Wall and Outrigger; (b) Action of Equivalent Full-Span Outrigger

converting the flexural rigidity of a wide-column beam Fig. 3(a), to the flexural rigidity of the equivalent full-span beam Fig. 3(b), thus

$$(EI)_o = \left(1 + \frac{a}{b} \right)^3 (EI')_o \dots (5)$$

The equivalent full-span beam $(EI)_o$ will be used throughout the paper. Conversion from, or reversion to the actual outrigger properties should be made using Eq. 5.

Core Moments, Column Forces and Outrigger Moments.—Rewriting Eqs. 4 *a* and *b*

$$M_1 [S_1 + S(H - X_1)] + M_2 S(H - X_2) = \frac{w}{6EI} (H^3 - X_1^3) \dots (6a)$$

$$\text{and } M_1 S(H - X_2) + M_2 [S_1 + S(H - X_2)] = \frac{w}{6EI} (H^3 - X_2^3) \dots (6b)$$

in which *S* and *S*₁ are parameters as given by

$$S = \frac{1}{EI} + \frac{2}{d^2(EA)_c} \dots (7)$$

$$\text{and } S_1 = \frac{d}{12(EI)_o} \dots (8)$$

The simultaneous solution of Eqs. 6*a* and *b* give expressions for the restraining moments that the outriggers apply to the core

$$M_1 = \frac{w}{6EI} \frac{S_1(H^3 - X_1^3) + S(H - X_2)(X_2^3 - X_1^3)}{S_1^2 + S_1 S(2H - X_1 - X_2) + S^2(H - X_2)(X_2 - X_1)} \dots (9a)$$

$$\text{and } M_2 = \frac{w}{6EI} \frac{S_1(H^3 - X_2^3) + S[(H - X_1)(H^3 - X_2^3) - (H - X_2)(H^3 - X_1^3)]}{S_1^2 + S_1S(2H - X_1 - X_2) + S^2(H - X_2)(X_2 - X_1)} \quad (9b)$$

The resulting core moment at any level, at a distance x from the top Fig. 2(e) is then given by

$$M_x = \frac{wx^2}{2} - M_1 - M_2 \dots \dots \dots (10)$$

in which, for $0 < x < X_1$, $M_1 = M_2 = 0$, and for $X_1 < x < X_2$, $M_2 = 0$.

The forces in the columns due to the bracing action are $\pm M_1/d$ for X_1

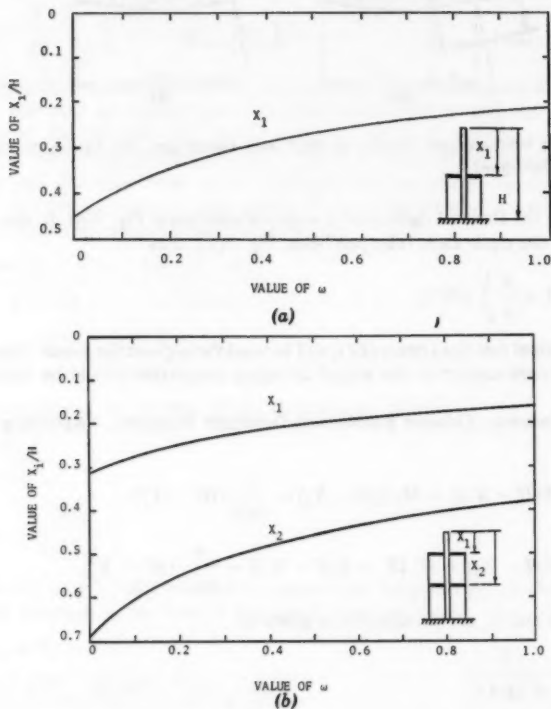


FIG. 4.—(a) Outrigger Optimum Levels in One-Outrigger Structure; (b) Outrigger Optimum Levels in Two-Outrigger Structure;

$< x < X_2$ and $\pm (M_1 + M_2)/d$ for $x > X_2$. Then the maximum bending moment in an outrigger is the product of the resultant column force at the end of the outrigger and the free length of the outrigger.

Drift Analysis.—The drift at the top of the structure is obtained conveniently

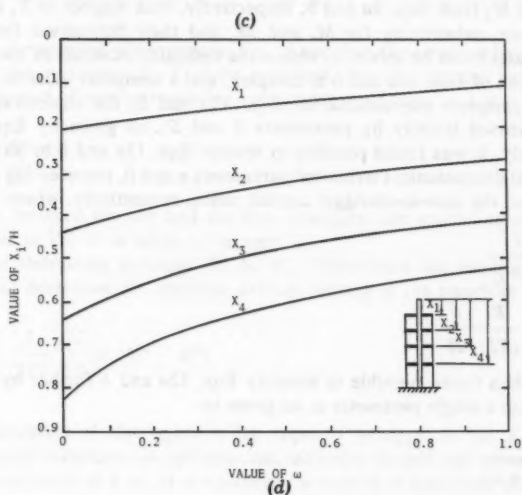
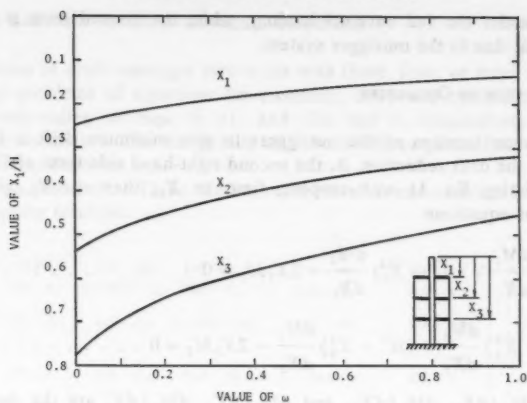


FIG. 4.—Continued: (c) Outrigger Optimum Levels in Three-Outrigger Structure; (d) Outrigger Optimum Levels in Four-Outrigger Structure

by the second moment-area method. Referring to the moment diagram Fig. 2(e)

$$\Delta_o = \frac{wH^3}{8EI} - \frac{1}{2EI} [M_1(H^2 - X_1^2) + M_2(H^2 - X_2^2)] \quad (11)$$

in which the first term on the right-hand side represents the free cantilever

deflection under the full external loading, while the second term is the drift reduction, Δ , due to the outrigger system.

OPTIMUM LOCATION OF OUTRIGGERS

The optimum location of the outriggers to give minimum drift is found by maximizing the drift reduction, Δ , the second right-hand side term of Eq. 11.

Differentiating Eq. 11 with respect, first, to X_1 , then, to X_2 , gives two simultaneous equations

$$(H^2 - X_1^2) \frac{dM_1}{dX_1} + (H^2 - X_2^2) \frac{dM_2}{dX_1} - 2X_1 M_1 = 0 \quad (12a)$$

$$\text{and } (H^2 - X_1^2) \frac{dM_1}{dX_2} + (H^2 - X_2^2) \frac{dM_2}{dX_2} - 2X_2 M_2 = 0 \quad (12b)$$

in which dM_1/dX_1 , dM_2/dX_1 , and dM_1/dX_2 , dM_2/dX_2 are the derivatives of M_1 and M_2 from Eqs. 9a and b, respectively, with respect to X_1 and X_2 .

Therefore, substituting for M_1 and M_2 and their derivatives from Eqs. 9, Eqs. 12a and b can be solved to obtain the optimum locations of the outriggers. The solution of Eqs. 12a and b is complex, and a computer must be used.

In the complete expressions for Eqs. 12a and b, the structural properties were expressed initially by parameters S and S_1 , as given by Eqs. 7 and 8, respectively. It was found possible to rewrite Eqs. 12a and b in terms of more meaningful dimensionless structural parameters α and β , representing the core-to-column and the core-to-outrigger inertial ratios, respectively, where

$$\alpha = \frac{2EI}{d^2(EA)_c} \quad (13)$$

$$\text{and } \beta = \frac{EI}{(EI)_o} \frac{d}{H} \quad (14)$$

It was then found possible to simplify Eqs. 12a and b further by combining α and β into a single parameter ω , as given by

$$\omega = \frac{\beta}{12(1 + \alpha)} \quad (15)$$

The parameter ω is a non-dimensional characteristic structural parameter for a uniform outrigger structure with flexible outriggers.

Eqs. 12a and b were solved to give the optimum outrigger levels X_1 and X_2 for a range of values of the structural parameter ω . These are plotted in Fig. 4(b). The restraining moments M_1 and M_2 and the top drift Δ_o for a structure with a characteristic parameter ω , and its outriggers located at the optimum drift reduction levels can be obtained by substituting the corresponding values of X_1 and X_2 from Fig. 4(b) into Eqs. 9a and b and 11, respectively. It should be noted that outriggers located for optimum drift reduction do not give a maximum core base moment reduction. The core base moment progressively reduces as the outriggers are placed lower on the structure.

GENERALIZED EQUATIONS FOR MULTI-OUTRIGGER STRUCTURES

The solution of multi-outrigger structures with three, four, or more outriggers (5) leads to problems of equations for moments, drift, and optimum outrigger levels corresponding to Eqs. 9, 11, and 12a and b, respectively, for the two-outrigger structure. The recognition of patterns allows generalized equations to be written as follows.

Restraining Moments.—These are expressed best in matrix form for simultaneous computer solution.

$$\begin{bmatrix} M_1 \\ M_2 \\ M_3 \\ \vdots \\ M_i \\ \vdots \\ M_n \end{bmatrix} = \frac{w}{6EI} \begin{bmatrix} S_1 + S(H - X_1) & S(H - X_2) & S(H - X_3) & \dots & S(H - X_i) & \dots & S(H - X_n) \\ S(H - X_2) & S_1 + S(H - X_1) & S(H - X_3) & \dots & S(H - X_i) & \dots & S(H - X_n) \\ S(H - X_3) & S(H - X_2) & S_1 + S(H - X_1) & \dots & S(H - X_i) & \dots & S(H - X_n) \\ \vdots & \vdots & \vdots & \ddots & \vdots & \ddots & \vdots \\ S(H - X_i) & S(H - X_2) & S(H - X_3) & \dots & S_1 + S(H - X_1) & \dots & S(H - X_n) \\ \vdots & \vdots & \vdots & \ddots & \vdots & \ddots & \vdots \\ S(H - X_n) & S(H - X_2) & S(H - X_3) & \dots & S(H - X_i) & \dots & S_1 + S(H - X_1) \end{bmatrix}^{-1} \begin{bmatrix} H^3 - X_1^3 \\ H^3 - X_2^3 \\ H^3 - X_3^3 \\ \vdots \\ H^3 - X_i^3 \\ \vdots \\ H^3 - X_n^3 \end{bmatrix} \quad (16)$$

in which n is the number of outriggers. Eq. 16 requires the structural properties and levels of the outriggers X_1 – X_n to be specified. Then the general expression for the distribution of core moment between outriggers j and $j + 1$ is

$$M_x = \frac{wx^2}{2} - \sum_{i=1}^j M_i \quad \dots \dots \dots (17)$$

In the region between the top and the first outrigger, the second term on the right-hand side of Eq. 17 is taken to be zero.

Drift.—The restraining moments M_1 to M_n , found from the solution of Eq. 16, are used to determine the resultant drift at the top of the structure ($x = 0$).

$$\Delta_o = \frac{wH^4}{8EI} - \frac{1}{2EI} \sum_{i=1}^n M_i (H^2 - X_i^2) \quad \dots \dots \dots (18)$$

Optimum Location of Outriggers.—The required outrigger levels X_1 to X_n , in an n -outrigger structure, to optimize the reduction in drift are given by the simultaneous solution of a set of n equations, written in matrix form as follows

$$\begin{bmatrix} M_{11} & M_{21} & M_{31} & \dots & M_{i1} & \dots & M_{n1} \\ M_{12} & M_{22} & M_{32} & \dots & M_{i2} & \dots & M_{n2} \\ M_{13} & M_{23} & M_{33} & \dots & M_{i3} & \dots & M_{n3} \\ \vdots & \vdots & \vdots & \ddots & \vdots & \ddots & \vdots \\ M_{1j} & M_{2j} & M_{3j} & \dots & M_{ij} & \dots & M_{nj} \\ \vdots & \vdots & \vdots & \ddots & \vdots & \ddots & \vdots \\ M_{1n} & M_{2n} & M_{3n} & \dots & M_{in} & \dots & M_{nn} \end{bmatrix} \begin{bmatrix} H^2 - X_1^2 \\ H^2 - X_2^2 \\ H^2 - X_3^2 \\ \vdots \\ H^2 - X_i^2 \\ \vdots \\ H^2 - X_n^2 \end{bmatrix} - 2 \begin{bmatrix} X_1 M_1 \\ X_2 M_2 \\ X_3 M_3 \\ \vdots \\ X_i M_i \\ \vdots \\ X_n M_n \end{bmatrix} = 0 \quad (19)$$

in which M_i is the restraining moment due to outrigger i , and M_{ij} is the derivative of M_i with respect to X_j , i.e.,

$$M_{ij} = \frac{dM_i}{dX_j}$$

Note that i and j both extend from 1- n . Thus, by substituting expressions for the restraining moments from Eq. 16, and their corresponding derivatives, Eq. 19 can be solved to obtain the optimum outrigger locations X_1 - X_n . These can be solved for ranges of values of the two structural parameters α and β , (Eqs. 13 and 14) or for a range of the single characteristic parameter ω (Eq. 15). Thus, curves can be drawn for a multi-outrigger structure giving the optimum levels of the outriggers for a range of values of the parameter ω .

Since the most usual number of outriggers in a structure is from 1-4, curves for the optimum outrigger levels in these structures are given in Figs. 4(a) to 4(d), respectively.

PERFORMANCE OF OUTRIGGER BRACED STRUCTURES

On the basis of the previous derivations, comments can be made on the performance of outrigger structures, with respect to variations in the size and structural arrangements of the core, outriggers, and columns. These variations include the core-to-column and core-to-outrigger inertia ratios and the number and levels of the outriggers.

Optimum Outrigger Levels.—Observation of the plots of outrigger optimum levels, Figs. 4(a)-4(d), show the following.

1. The more flexible the outriggers, the other properties remaining constant, the higher up the structure their optimum levels are.
2. The larger the value of the column system inertia, the relatively more sensitive the structure is to the outrigger flexibility.
3. For a constant value of core-to-outrigger inertia ratio, i.e., β constant, decreasing values of column stiffness, i.e., α increasing, cause the optimum outrigger levels to move downwards towards the optimum levels for the case of flexurally rigid outriggers.

Reduction in Core Moment.—A useful measure of the influence of the outrigger system on the core moment is to express the reduction in the core base moment as a percentage of the maximum possible moment reduction, M_c , that would occur if the core and columns behaved fully compositely. The result may be termed a "moment reduction efficiency," denoted by $M\%$. Fully composite behavior occurs when plane sections through the building before bending remain plane during bending. In the fully composite case the core moment reduction due to the columns is given by

$$M_c = \left[\frac{(EA)_c \frac{d^2}{2}}{EI + (EA)_c \frac{d^2}{2}} \right] \frac{wH^2}{2} \dots \dots \dots (20)$$

$$\text{or } M_c = \frac{1}{EIS} \frac{wH^2}{2} \dots \dots \dots (21)$$

in which S is given by Eq. 7. Then, expressing the actual moment reduction at the base as a percentage of the fully composite reduction

$$M\% = \frac{\sum_{i=1}^n M_i}{M_c} \times 100 \dots \dots \dots (22)$$

The moment reduction efficiency for structures with up to four outriggers optimally located for maximum drift reduction is given as a function of the

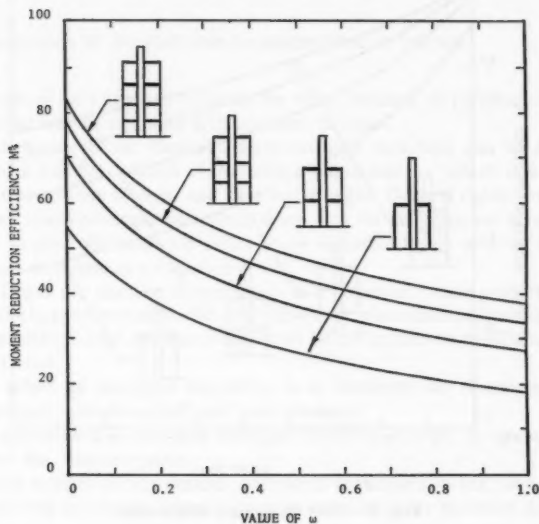


FIG. 5.—Moment Reduction Efficiencies for Optimum Located Outriggers

characteristic structural parameter ω in Fig. 5. Using Fig. 5 in reverse, the core base moment can be obtained from the graph by

$$M_H = \frac{wH^2}{2} \left(1 - \frac{M\%}{100} \cdot \frac{1}{EIS} \right) \dots \dots \dots (23)$$

In this study the reduction in the core moment has been considered as secondary to the reduction in drift. The, so called, "optimum outrigger levels" are calculated for the maximum reduction in drift at the top of the structure. The reductions in the core base moment, expressed by Eq. 22 and Fig. 5, are those corresponding to the optimum outrigger locations. If drift is not the critical consideration, additional reductions in core moments at the base and at the intermediate heights

could be achieved by locating the outriggers lower than their "optimum" levels. A hypothetical maximum reduction in base moment could be achieved with an outrigger placed close to the base. However, this would contribute little to the drift resistance. For outriggers located at other than optimum locations, the corresponding core moments and top drift can be calculated using Eqs. 17 and 18, respectively.

Reduction in Drift.—The drift performance of an outrigger structure can also be usefully expressed as a "drift reduction efficiency," $\Delta\%$. In this case, the drift reduction due to the outrigger system is expressed as a percentage of the drift reduction that would occur if the system behaved fully compositely.

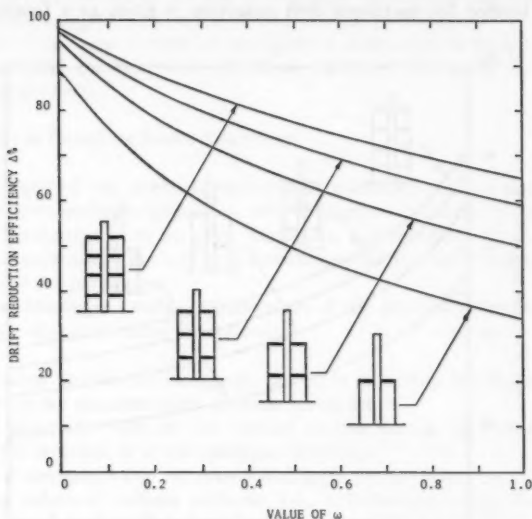


FIG. 6.—Drift Reduction Efficiencies

Corresponding to the fully composite moment reduction, Eqs. 20 and 21, the fully composite drift reduction is given by

$$\Delta_c = \frac{1}{EIS} \frac{wH^4}{8EI} \dots \dots \dots (24)$$

$$\text{then } \Delta\% = \frac{\frac{1}{2EI} \sum_{i=1}^n M_i(H^2 - X_i^2)}{\Delta_c} \dots \dots \dots (25)$$

Variations of $\Delta\%$ are plotted in Fig. 6, for 1-4 optimally arranged outrigger structures, as a function of the characteristic parameter ω . The curves can be used either to assess the efficiency of a proposed structural system or to determine the top drift of the system using

$$\Delta_o = \frac{wH^4}{8EI} \left(1 - \frac{\Delta\%}{100} \frac{1}{EIS} \right) \dots \dots \dots (26)$$

Fig. 6 shows that the larger the number of outriggers, other factors being constant, the greater the drift reduction. However, the "law of diminishing returns" applies in that the increments of increase in efficiency reduce for each additional outrigger. This effect of diminishing return suggests that four outriggers is probably the maximum number that can be justified.

Fig. 6 also indicates that outrigger flexibility reduces the drift efficiency of the structure, but with a lesser reduction for more flexible column systems.

CONCLUSIONS

The conclusions of the study can be summarized as follows.

1. The use of outriggers to mobilize the axial stiffness of peripheral columns is an efficient way of reducing drift and core moment.
2. The behavior of an idealized multi-outrigger structure can be expressed in terms of a nondimensional characteristic parameter, ω , which is a function of the core-to-column system, and core-to-outrigger, flexural rigidity ratios.
3. In any multi-outrigger structure, there is a set of optimum levels of the outriggers to give minimum top drift. These optimum levels may be expressed in a uniform structure as a function of ω .
4. The larger the number of outriggers in a structure, other properties being constant, the larger the reduction in drift. However, since each additional outrigger has a lesser effect, four outriggers appear to be the maximum justifiable number for drift control.
5. The effect of outrigger flexibility is to diminish the restraining effects of the outrigger system on drift and core moment.
6. The influence of a change in outrigger flexibility is larger for greater inertial stiffness of the column system.
7. If drift control is not critical, additional reductions in the core moments can be achieved by placing the outriggers at lower than the optimum drift levels.

APPENDIX I.—REFERENCES

1. Batiment, Les Nouveaux Edifices de la Place Victoria a Montreal, (in French) January, 1964.
2. Taranath, B. S., "Optimum Belt Truss Location for High-Rise Structures," *Structural Engineer*, Vol. 53, No. 8, Aug., 1975.
3. McNabb, J. W., and Muvdi, B. B., "Drift Reduction Factors for Belt High-Rise Structures," *Engineering Journal*, American Institute of Steel Construction, 3rd Quarter, 1975.
4. Stafford Smith, B., and Nwaka, I. O., "The Behaviour of Multi-Outrigger Braced Tall Buildings," American Concrete Institute Special Publication of Papers for Symposium on Reinforced Concrete Structures, sponsored by Committee 442, 1980.
5. Salim, I., "The Behaviour of Flexible-Outrigger Braced Tall Buildings," Mechanical Engineering Report, Department of Civil Engineering and Applied Mechanics, McGill University, Montreal, Canada, 1980.

APPENDIX II.—NOTATION

- A_c = sectional area of column;
 d = distance between columns;
 E = elastic modulus;
 H = height of structure;
 I = moment of inertia of core;
 I'_o = actual moment of inertia of outrigger;
 I_o = effective moment of inertia of outrigger;
 M_x = moment in core at distance x from top;
 M_1, M_2, M_i = restraining moments due to outriggers 1, 2, i ;
 M_c = reduction in core base moment for fully-composite structure;
 $M\%$ = moment reduction efficiency;
 S, S_1 = structural parameters;
 w = horizontal load per unit height;
 x = distance from top of structure;
 X_1, X_2 = distance of outriggers 1, 2 etc from top of structure;
 α = non-dimensional parameter representing flexural rigidity ratio of core-to-column system;
 β = non-dimensional parameter representing flexural rigidity ratio of core-to-outrigger;
 Δ = reduction in top drift due to outrigger systems;
 Δ_c = reduction in top drift in fully-composite structure;
 Δ_o = resultant drift at top of structure;
 $\Delta\%$ = drift reduction efficiency;
 θ = rotation of core or outrigger; and
 ω = non-dimensional characteristic parameter for outrigger structures with flexible cantilevers [$\omega = \beta/12(1 + \alpha)$].

SHAPE OPTIMIZATION: FINITE ELEMENT EXAMPLE

By William R. Spillers,¹ M. ASCE and Sohan Singh²

INTRODUCTION

Shape optimization (geometric optimization) of structures deals with situations in which the shape of a structure is not known a priori, but is to be determined along with other parameters, using some sort of optimization algorithm. Since it is most common to optimize other structural parameters keeping the shape fixed, the additional difficulty associated with changing geometry makes problems of shape optimization the most complex structural optimization problems encountered.

The literature of shape optimization within the finite element method is rather sparse. There is, first of all, a branch of it in which node locations do not change, but shape varies as some element thicknesses go to zero (13). (This is analogous to using an algorithm to determine an optimal skeletal substructure given an unnecessarily complex initial layout.) Since the node locations are not determined directly by the analysis, this type of shape optimization is not in the spirit of the present work.

Of the approaches that have been used in continuum-type structural optimization problems, there is little commonality. These methods range from the heuristic (11) in which Umetani and Hirai postulate a bone growth mechanism based upon the existing state of stress to the quasicontinuous (1) approach of Chung and Haug who only resort to the finite element method after performing sensitivity studies based in the calculus of variations. Somewhere in the middle lay the work of Ramakrishnan and Francavilla (7) and the work of Dems and Mroz (2) who optimize specific boundary-related parameters. It is typical of the state-of-the-art of structural optimization that no uniform approach to shape optimization has yet emerged. It is typical of the state-of-the-art of shape optimization that problem complexity obviates all but relatively simple applications.

This present effort derives from the 1971 Ph.D. thesis of Friedland (4), which dealt with optimal shape for trusses. Friedland's work was subsequently extended

¹Prof., Dept. of Civ. Engrg., Rensselaer Polytechnic Inst., Troy, N.Y.

²Graduate Student, Dept. of Civ. Engrg., Rensselaer Polytechnic Inst., Troy, N.Y.

Note.—Discussion open until March 1, 1982. To extend the closing date one month, a written request must be filed with the Manager of Technical and Professional Publications, ASCE. Manuscript was submitted for review for possible publication on November 26, 1980. This paper is part of the Journal of the Structural Division, Proceedings of the American Society of Civil Engineers, ©ASCE, Vol. 107, No. ST10, October, 1981. ISSN 0044-8001/81/0010-2015/\$01.00.

to other optimal shape problems for skeletal structures (8-10). The point is that the discretization process of the finite element method produces a structural system that shares much in form with the matrix formulation of skeletal structures. This similarity of form is used here as a basis for extending shape optimization procedures developed for skeletal structures to continuum problems when modeled by the finite element method.

This paper treats the most simple finite element problem of plane stress using a constant stress triangular element. It is hoped that the reader will regard this effort as an attempt to demonstrate feasibility and forgive—at least for the time being—the shortcomings of this particular element.

With regard to optimization itself, the paper adopts a simplification developed in earlier work in which the problem is formulated in terms of "force" variables neglecting the constitutive equations, i.e., the plate thickness is written in terms of element stresses, which must, in turn, satisfy node equilibrium equations. As argued earlier, this procedure is most simply explained in terms of plastic design, but may also be regarded as an "embedding" of an elastic design problem in a larger space that does not contain the constitutive equations. The point is that since the optimal design is statically determinate, the satisfaction of the constitutive equations can be argued a posteriori. The algorithm itself uses the Lagrange multiplier method to convert an optimization problem to a problem of solving a nonlinear system; then, Newton's method is applied. The algorithm is simple in concept and relatively direct. At every step in the process of iterating, all the node coordinates (which are allowed to change under the problem statement) change.

FINITE ELEMENT METHOD

It is, first of all, necessary to establish the notation of the finite element method. Following Zienkiewicz (14), the simple case of all triangular, plane stress, constant strain elements may be written as

$$\text{Node Equilibrium } \mathbf{q}^e = \mathbf{B}^T \mathbf{v}^e \boldsymbol{\sigma} \quad \dots \dots \dots (1)$$

$$\text{Constitutive Equation } \boldsymbol{\sigma} = \mathbf{D} \boldsymbol{\epsilon} \quad \dots \dots \dots (2)$$

$$\text{Strain-Displacement By } \boldsymbol{\epsilon} = \mathbf{B} \mathbf{u} \quad \dots \dots \dots (3)$$

in which $\boldsymbol{\sigma}$ = stress matrix; $\boldsymbol{\epsilon}$ = strain matrix; \mathbf{D} = elasticity matrix; \mathbf{B} = shape function matrix; \mathbf{q}^e = (applied) node force matrix; \mathbf{v}^e = element volume matrix; and \mathbf{u} = element displacement field.

Zienkiewicz (14) provides the detail of the finite element method for the case of triangular, constant strain, and plane stress elements as indicated below.

Element Variables.—Associated with each triangular finite element i are a stress matrix, $\boldsymbol{\sigma}$, a strain matrix, $\boldsymbol{\epsilon}$, and an elasticity matrix, \mathbf{D} , so that

$$\boldsymbol{\sigma} = \begin{bmatrix} \sigma_x \\ \sigma_y \\ \tau_{xy} \end{bmatrix} \quad \boldsymbol{\epsilon} = \begin{bmatrix} \epsilon_x \\ \epsilon_y \\ \epsilon_{xy} \end{bmatrix} \quad \mathbf{D} = \begin{bmatrix} 1 & \nu & 0 \\ \nu & 1 & 0 \\ 0 & 0 & (1-\nu)/2 \end{bmatrix} \frac{E}{1-\nu^2} \quad \dots \dots \dots (4)$$

in which E = Young's Modulus; and ν = Poisson's Ratio. The element strains are related to the element displacement field (u, v) as

$$\epsilon = \begin{bmatrix} \epsilon_x \\ \epsilon_y \\ \tau_{xy} \end{bmatrix} = \begin{bmatrix} \partial u / \partial x \\ \partial v / \partial y \\ \partial u / \partial y + \partial v / \partial x \end{bmatrix} \dots \dots \dots (5)$$

Node Variables.—Associated with each node, i , of the system in a displacement vector, u , and an applied load vector, q , so that

$$u = \begin{bmatrix} u_i \\ v_i \end{bmatrix} \quad q = \begin{bmatrix} U_i \\ V_i \end{bmatrix} \dots \dots \dots (6)$$

Shape Function Matrix.—The contribution of any element whose nodes are i, j, m to the equilibrium equations of the system can be written as

$$F^e = B^T \sigma (t A) \dots \dots \dots (7)$$

in which t = element thickness; and A = element area. In particular, the matrix B can be partitioned as

$$B = [B_i B_j B_m] \dots \dots \dots (8)$$

$$\text{in which } B_r = \begin{bmatrix} b_r & 0 \\ 0 & c_r \\ c_r & b_r \end{bmatrix} \frac{1}{2A} \quad r = i, j, m \dots \dots \dots (9)$$

and, for example,

$$b_i = y_j - y_m \quad \text{and} \quad c_i = x_m - x_j \dots \dots \dots (10)$$

In terms of these variables Eq. (7) can be written explicitly as

$$F^e = \frac{t}{2} \begin{bmatrix} b_i & 0 & c_i \\ 0 & c_i & b_i \\ b_j & 0 & c_j \\ 0 & c_j & b_j \\ b_m & 0 & c_m \\ 0 & c_m & b_m \end{bmatrix} \begin{bmatrix} \sigma_x \\ \sigma_y \\ \tau_{xy} \end{bmatrix} = \frac{t}{2} \begin{bmatrix} b_i \sigma_x + c_i \tau_{xy} \\ c_i \sigma_y + b_i \tau_{xy} \\ b_j \sigma_x + c_j \tau_{xy} \\ c_j \sigma_y + b_j \tau_{xy} \\ b_m \sigma_x + c_m \tau_{xy} \\ c_m \sigma_y + b_m \tau_{xy} \end{bmatrix} \dots \dots \dots (11)$$

The point is that, for the type of element under discussion, these matrices all have rather simple and "explicit" definitions that may be differentiated.

OPTIMIZATION PROBLEM

The intention of this section is to set up an optimization problem in which the volume of material, written in terms of stresses, is to be minimized while satisfying node equilibrium and varying some subset of node coordinates. While any well behaved stress-volume relationship could be used (8), for reasons of simplicity the Mises yield condition,

$$\sigma_x^2 - \sigma_x \sigma_y + \sigma_y^2 + 3 \tau_{xy}^2 = f_y^2 \dots \dots \dots (12)$$

will be used here to determine the element thickness given the element stresses.

In Eq. 12 f_y is the yield stress in uniaxial tension or compression. Furthermore, it should be noted that only a restricted set of node coordinates may be allowed to vary during the optimization process since, if all nodes were allowed to move, the loads would move to the supports giving an optimal design of zero volume.

The optimization problem can now be formulated to find the unknown node coordinates and the element thicknesses which

$$\text{Minimize } \sum_{\text{elements}} A_i t_i \text{ (material volume)} \dots \dots \dots (13)$$

$$\text{Subject to } \mathbf{q}^e = \mathbf{B}^T \mathbf{v}^e \boldsymbol{\sigma} \text{ (node equilibrium)} \dots \dots \dots (14)$$

$$t_i = t_i(\sigma_i, A_i) \text{ (yield condition)} \dots \dots \dots (15)$$

It should be noted here that there have been several solutions to this optimization problem when the node coordinates are fixed and only the element thicknesses vary (3).

For numerical reasons, it is convenient to make a change of variables at this point. As discussed earlier, the approach presented in this paper is motivated by the truss problem where it has been quite successful. In the truss problem, the "force" variables used are in fact bar forces. For the finite element method, the obvious choice of "force" variables, the member stress, leads to numerical difficulties in the solution of the Kuhn-Tucker conditions. In an attempt to arrive at variables with the same dimensions as the truss problem, the following transformations are used for each element

$$\sigma t \sqrt{A} = F; \quad \mathbf{B}^T \sqrt{A} = \mathbf{N}^T; \quad t \mathbf{D} = \mathbf{K}; \quad \text{and} \quad \Delta = \sqrt{A} \boldsymbol{\epsilon} \dots \dots \dots (16)$$

That is, new variables F , \mathbf{N} , \mathbf{K} , Δ that are analogous to the variables σ , \mathbf{B} , \mathbf{D} , $\boldsymbol{\epsilon}$ are introduced. In terms of these new variables, the optimization problem in Eqs. 13-15 becomes

$$\text{minimize } f = \frac{f_y}{E} \sum_{\text{elements}} Z_i A_i \dots \dots \dots (17)$$

$$\text{subject to } \mathbf{N}^T \mathbf{F} = \mathbf{q}^e \dots \dots \dots (18)$$

$$\text{in which } Z_i = t_i \sqrt{A_i} [\sigma_i^2 - \sigma_x \sigma_y + \sigma_y^2 + 3 \tau_{xy}^2]^{1/2} \dots \dots \dots (19)$$

Optimality Conditions.—Proceeding in a classical manner, it is now possible to replace the above optimization problem by a nonlinear system in the following manner. First of all the Lagrangian of Eqs. 17-19 is formed as

$$\mathcal{L} = f(F, r) + \delta^T (q^e - \mathbf{N}^T \mathbf{F}) \dots \dots \dots (20)$$

in which δ is a matrix of Lagrange multipliers, and r is the set of node coordinates that is allowed to vary. The Kuhn-Tucker (optimality) conditions are then derived as

$$\frac{\partial \mathcal{L}}{\partial \delta_i} = 0 \Rightarrow \mathbf{N}^T \mathbf{F} = \mathbf{q}^e \dots \dots \dots (21)$$

$$\frac{\partial \mathcal{L}}{\partial F_i} = 0 \Rightarrow \frac{\partial f}{\partial F_i} = (\mathbf{N} \delta)_i \dots \dots \dots (22)$$

$$\frac{\partial \mathcal{L}}{\partial r_i} = 0 \Rightarrow \frac{\partial f}{\partial r_i} = \frac{\partial (\delta^T N^T F)}{\partial r_i} \dots \dots \dots (23)$$

It has been convenient in the past to solve systems, such as Eqs. 21-23, in two steps, first fixing the geometry and computing element thickness, then fixing the thicknesses and computing new node coordinates. The case of fixed geometry has been described elsewhere (3), and it will only be noted here that to optimize in this case simply requires iterating with any standard finite element program using (Poisson's ratio) $\nu = 1/2$ and at each step using the yield condition to derive new element thicknesses.

For the step in which the thicknesses are fixed and new node coordinates are to be computed, Eq. 23 is simply linearized in a Newtonian manner and used to compute these changes in coordinates. Some of the details of this step will now be discussed.

Borrowing some from nonlinear structures, it is convenient to rewrite Eq. 23 as

$$\nabla f - K_G \delta = 0 \quad \text{or} \quad \mathcal{F} = 0 \dots \dots \dots (24)$$

in which the gradient operator refers to the unknown node coordinates and K_G is the geometric stiffness matrix. Using Newton's method, Eq. 24 is linearized as

$$\mathcal{F}_0 + \nabla \mathcal{F}_0 dr = 0 \quad \text{or} \quad dr = -\nabla \mathcal{F}_0^{-1} \mathcal{F}_0 \dots \dots \dots (25)$$

It is, therefore, necessary to compute the gradient matrix of both ∇f and $K_G \delta$ in order to compute the changes in coordinates, dr .

Some Gradient Terms.—As indicated in Eq. 20, the application of Newton's method to the optimality criterion of Eq. 23 requires that some derivatives of finite element terms be computed. These derivatives are discussed below.

It is convenient to note first of all that the gradient of the element area with respect to the x and y coordinates of the 3 nodes can be written simply in terms of the b 's and c 's of the finite element method as

$$\nabla A = \begin{bmatrix} b_i \\ c_i \\ b_j \\ c_j \\ b_m \\ c_m \end{bmatrix} \frac{1}{2} \dots \dots \dots (26)$$

Since f is defined by Eq. (9) it follows that

$$\nabla f = \frac{f_y}{E} \sum_{\text{elements}} Z_i \frac{1}{4A^{1/2}} \begin{bmatrix} b_i \\ c_i \\ b_j \\ c_j \\ b_m \\ c_m \end{bmatrix} \dots \dots \dots (27)$$

From the definition of the b 's and c 's (Eq. 10) it follows that

$$\nabla = \begin{bmatrix} b_i \\ c_i \\ b_j \\ c_j \\ b_m \\ c_m \end{bmatrix} = \begin{bmatrix} & & 1 & -1 \\ & -1 & & 1 \\ & & & 1 \\ & & & -1 \\ \text{symm.} & & & \end{bmatrix} \dots \dots \dots (28)$$

from which the Hessian matrix of the function, f , follows directly.

The geometric stiffness matrix and its gradient are somewhat more difficult to deal with. It is first of all convenient to define a new set of coefficients

$$b_i^* = b_i A^{-1/2} \quad c_i^* = c_i A^{-1/2} \text{ etc.} \dots \dots \dots (29)$$

whose derivatives may be computed as

$$b_{r,s}^* = \frac{\partial}{\partial x_s} \frac{b_r}{\sqrt{A}} = b_{r,s} A^{-1/2} - \frac{1}{2} b_r A^{-3/2} \frac{\partial A}{\partial x_s} \dots \dots \dots (30)$$

$$c_{r,s}^* = \frac{\partial}{\partial x_s} \frac{c_r}{\sqrt{A}} = c_{r,s} A^{-1/2} - \frac{1}{2} c_r A^{-3/2} \frac{\partial A}{\partial x_s} \dots \dots \dots (31)$$

Second derivatives may also be computed as

$$\begin{aligned} \frac{\partial}{\partial x_t} b_{r,s}^* &= -\frac{1}{2} b_{r,s} A^{-3/2} \frac{\partial A}{\partial t} - \frac{1}{2} \left[b_{r,t} A^{-3/2} \frac{\partial A}{\partial s} + b_r A^{-3/2} \frac{\partial^2 A}{\partial s \partial t} \right. \\ &\quad \left. - \frac{3}{2} A^{-5/2} \frac{\partial A}{\partial t} \frac{\partial A}{\partial s} b_r \right] \text{ etc.} \dots \dots \dots (32) \end{aligned}$$

It follows now from Eq. 11 that

$$K_G = \nabla \begin{bmatrix} b_i^* F_x + c_i^* F_{xy} \\ c_i^* F_y + b_i^* F_{xy} \\ b_j^* F_x + c_j^* F_{xy} \\ c_j^* F_y + b_j^* F_{xy} \\ b_m^* F_x + c_m^* F_{xy} \\ c_m^* F_y + b_m^* F_{xy} \end{bmatrix} \frac{1}{2} \dots \dots \dots (33)$$

or that K_G may be partitioned as

$$K_{Grs} = \begin{bmatrix} b_{r,x_s}^* F_x + c_{r,x_s}^* F_{xy} & b_{r,y_s}^* F_x + c_{r,y_s}^* F_{xy} \\ c_{r,x_s}^* F_y + b_{r,x_s}^* F_{xy} & c_{r,y_s}^* F_y + b_{r,y_s}^* F_{xy} \end{bmatrix} \dots \dots \dots (34)$$

The vector form returns again when K_G is multiplied by δ as

$$(\mathbf{K}_G \delta)_x = \sum_{r=i,j,m} \frac{1}{2} \left[(b_{r,x}^* F_x + c_{r,x}^* F_{xy}) \delta_{r_x} + (b_{r,y}^* F_x + c_{r,y}^* F_{xy}) \delta_{r_y} \right] \quad (35)$$

$$(c_{r,x}^* F_y + b_{r,x}^* F_{xy}) \delta_{r_x} + (c_{r,y}^* F_y + b_{r,y}^* F_{xy}) \delta_{r_y}$$

It is clearly possible to take the gradient of Eq. 25 by since there is no convenient form to put it in, no further derivatives will be indicated here.

CASE STUDIES

Following Ref. 3, again two applications of the above optimization procedure are presented here (Fig. 1). The first is simply a fixed ended plate (beam) whose lower right hand node is loaded vertically. In the second example, a hole which is allowed to move is added to the first example.

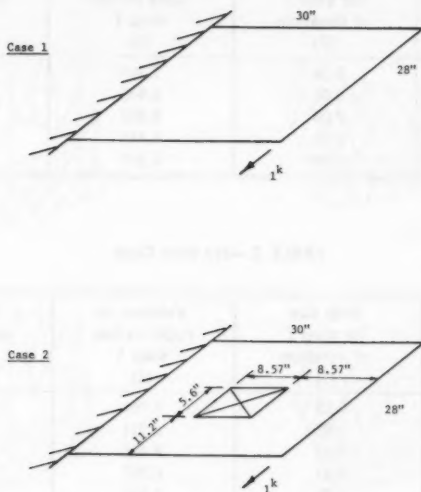


FIG. 1.—Dimensions for Examples

Several comments concerning numerical performance are in order. First of all, there is the common problem that the step size, which emerges from Newton's method, is sometimes too large. It is, however, a relatively simple matter to reduce the step size automatically when the new design does not have a reduced weight. A more difficult problem has to do with the aspect ratios of the finite elements. As can be seen from the figures at the end of this paper, the aspect ratio of some finite elements can degenerate quickly. The solution to this problem should be to lay out a new mesh when this degeneracy occurs. That has not been done here, and is left to future efforts. Tables 1 and 2 actually indicate a possible conjunction between problems of step size and aspect ratio degeneracy to the extent that step size difficulties increase with increasing iterations. One might expect this effect to disappear if relay layout is used at every iteration.

With regard to the shapes that have evolved under optimization (Fig. 2), it would be theoretically possible to construct a Michell truss to transmit the load efficiently to the supports (5). This truss would follow two orthogonal families of lines forming a Henky-Prandtl net. While this paper is concerned with finite element layout rather than truss layout, it should be noted the results bear considerable resemblance to a Henky net. It is possible that as the mesh is refined the Henky-Prandtl net will become more prominent.

TABLE 1.—Moving Hole Case

Iteration (1)	Step size for step 2 of iteration (2)	Volume, in cubic inches step 1 (3)	Volume, in cubic inches step 2 (4)
1	0.06	7.809	7.407
2	0.05	6.945	6.830
3	0.04	6.603	6.573
4	0.02	6.431	6.436
5	0.009	6.361	6.368

TABLE 2.—No Hole Case

Iteration (1)	Step size for step 2 of iteration (2)	Volume, in cubic inches step 1 (3)	Volume, in cubic inches step 2 (4)
1	0.08	7.764	7.334
2	0.05	6.761	6.667
3	0.02	6.463	6.425
4	0.01	6.383	6.380
5	0.01	6.336	6.339
6	0.01	6.294	6.298
7	0.01	6.260	6.264
8	0.005	6.229	6.231
9	0.001	6.215	6.215
10	0.001	6.211	6.211

A final comment on computer graphics is in order. Even for the case of fixed geometry, it is almost impossible to understand thickness distributions without some sort of three-dimensional graphic presentation. When node locations are also allowed to change, it becomes doubly difficult to understand and, thus, monitor design generated by an algorithm. It is then, in fact, almost impossible to deal properly with problems of this kind without on-line computer graphics displays. Fig. 2 attempts to convey something of the spirit of the computer graphics environment but space limitations make that difficult in the print media.

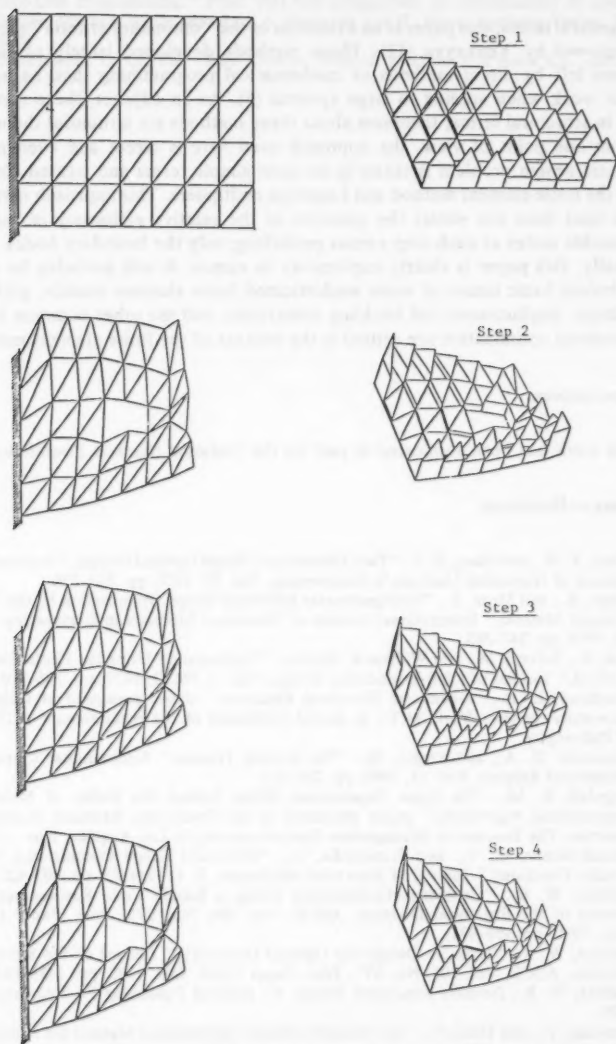


FIG. 2.—Computer Graphics Output: Shape Versus Thickness

CONCLUDING REMARKS

In general terms, this paper is an extension of the "optimality criteria" methods championed by Venkayya (12). These methods developed largely to fill the vacuum left by direct methods of mathematical programming that, as a rule, do not work when applied to large systems (6). As an adjunct, these methods work in structural terms; theorems about these methods are structural theorems.

From one point of view, the approach used here is direct and even naive. A plastic design problem is taken in its most simple terms and treated directly using the finite element method and Lagrange multipliers. This approach certainly raises (and does not settle) the question of the relative efficiency of moving all possible nodes at each step versus perturbing only the boundary nodes.

Finally, this paper is clearly exploratory in nature. It will probably be some time before basic issues of more sophisticated finite element models, grid size and shape, displacement and buckling constraints, and the other common issues of structural optimization are settled in the context of the finite element method.

ACKNOWLEDGMENT

This work has been supported in part by the National Science Foundation.

APPENDIX.—REFERENCES

1. Chun, Y. W., and Haug, E. J., "Two-Dimensional Shape Optimal Design," *International Journal of Numerical Methods in Engineering*, Vol. 13, 1978, pp. 311-336.
2. Dems, K., and Mroz, Z., "Multiparameter Structural Shape Optimization by the Finite Element Method," *International Journal of Numerical Methods in Engineering*, Vol. 13, 1978, pp. 247-263.
3. Fok, E., Teferra, M., and William R. Spillers, "Optimization Using the Finite Element Method," *Journal of Civil Engineering Design*, Vol. 1, No. 3, 1979, pp. 305-310.
4. Friedland, L. R., "Geometric Structural Behavior," thesis presented at Columbia University, in New York, N.Y., in partial fulfillment of the requirements of Doctor of Philosophy.
5. Hegemier, G. A., and Prager, W., "On Michell Trusses," *International Journal of Mechanical Science*, Vol. 11, 1969, pp. 209-215.
6. Ragsdell, K. M., "On Some Experiments While Delimit the Utility of Nonlinear Programming Algorithms," paper presented at the Operations Research Society of America, The Institute of Management Science meeting in Los Angeles, Nov., 1978.
7. Ramakrishnan, C. V., and Francavilla, A., "Structural Shape Optimization Using Penalty Functions," *Journal of Structural Mechanics*, 3, 4, 1974-75, pp. 403-422.
8. Spillers, W. R., "Geometric Optimization Using a Simple Code Representation," *Journal of the Structural Division, ASCE*, Vol. 106, No. ST5, Proc. Paper 15396, May, 1980, pp. 959-971.
9. Spillers, W. R., "Iterative Design for Optimal Geometry," *Journal of the Structural Division, ASCE*, Vol. 101, No. ST7, Proc. Paper 11439, July, 1975, pp. 1435-1442.
10. Spillers, W. R., *Iterative Structural Design*, N. Holland Publishing Co., Amsterdam, 1975.
11. Umetani, Y., and Hirai, S., "An Adaptive Shape Optimization Method for Structural Material," Proc. 1975, Joint Japanese Society of Mechanical Engineers-American Society of Mechanical Engineers Applied Mechanics Western Conference, pp. 359-365.
12. Venkayya, V. B., "Structural Optimization: A Review and Some Recommendations," *International Journal of the Numerical Methods in Engineering*, Vol. 13, 1978, pp. 203-228.

13. Zavelani, A., Maier, G., Binda, L., "Shape Optimization of Plastic Structures by Zero-One Programming," Proc. IUTAM Symposium on *Optimization in Structural Design*, Warsaw, 1973, edited by A. Sawczuk and Z. Mroz, Springer-Verlag, Berlin, 1975.
14. Zienkiewicz, O. C., *The Finite Element Method*, McGraw Hill Book Co., Inc., New York, N.Y., 1977.

TECHNICAL NOTES

TECHNICAL NOTES

Note.—Discussion open until March 1, 1982. To extend the closing date one month, a written request must be filed with the Manager of Technical and Professional Publications, ASCE. This paper is part of the Journal of the Structural Division, Proceedings of the American Society of Civil Engineers, ©ASCE, Vol. 107, No. ST10, October, 1981.

TECHNICAL NOTES

To provide a place within ASCE for publication of technical ideas that have not advanced, as yet, to the point where they warrant publication as a Proceedings paper in a *Journal*, the publication of Technical Notes was authorized by the Board of Direction on October 16-18, 1967, under the following guidelines:

1. An original manuscript and two copies are to be submitted to the Manager of Technical and Professional Publications, ASCE, 345 East 47th Street, New York, N.Y., 10017, along with a request by the author that it be considered as a Technical Note.
2. The two copies will be sent to an appropriate Technical Division or Council for review.
3. If the Division or Council approves the contribution for publication, it shall be returned to Society Headquarters with appropriate comments.
4. The technical publications staff will prepare the material for use in the earliest possible issue of the *Journal*, after proper coordination with the author.
5. Each Technical Note is not to exceed 4 pages in the *Journal*. As an approximation, each full manuscript page of text, tables, or figures is the equivalent of one-half a *Journal* page.
6. The Technical Notes will be grouped in a special section of each *Journal*.
7. Information retrieval abstracts and key words will be unnecessary for Technical Notes.
8. The final date on which a Discussion should reach the Society is given as a footnote with each Technical Note.
9. Technical Notes will not be included in *Transactions*.
10. Technical Notes will be included in ASCE's annual and cumulative subject and author indexes.

The manuscripts for Technical Notes must meet the following requirements:

1. Titles must have a length not exceeding 50 characters and spaces.
2. The author's full name, Society membership grade, and a footnote reference stating present employment must appear on the first page of the manuscript. Authors need not be Society members.
3. The manuscript is to be submitted as an original copy (with two duplicates) that is typed double-spaced on one side of 8-1/2-in. (220-mm) by 11-in. (280-mm) white bond paper.
4. All mathematics must be typewritten and special symbols must be properly identified. The letter symbols used must be defined where they first appear, in figures or text, and arranged alphabetically in an Appendix.—Notation.
5. Standard definitions and symbols must be used. Reference must be made to the lists published by the American National Standards Institute and to the *Authors' Guide to the Publications of ASCE*.
6. Tables must be typed double-spaced (an original ribbon copy and two duplicate copies) on one side of 8-1/2-in. (220-mm) by 11-in. (280-mm) paper. An explanation of each table must appear in the text.
7. Figures must be drawn in black ink on one side of 8-1/2-in. (220-mm) by 11-in. (280-mm) paper. Because figures will be reproduced with a width of between 3 in. (76 mm) to 4-1/2 in. (110 mm), the lettering must be large enough to be legible at this width. Photographs must be submitted as glossy prints. Explanations and descriptions must be made within the text for each figure.
8. References cited in text must be typed at the end of the Technical Note in alphabetical order in an Appendix.—References.
9. Dual units, i.e., U.S. Customary followed by SI (International System) units in parentheses, should be used throughout the paper.

DETERMINATE TENSEGRIC SHELLS

By Oren Vilnay¹

INTRODUCTION

A tensegric shell consists of a net of cables and bars connected at both of their ends to the cable net nodes, no bar is connected to the other bars. Because of the lack of a continuous supporting rigid element the tensegric shell is loose and does not have a definite shape before erection. The shell is stabilized to the required shape by prestressing. Prestressing of the tensegric shell can be achieved by proper lengthening of some bars or by proper shortening of some cables. The prestressing gives the shell its shape and introduces tension in the cables and compression in the bars. When the shell is in its prestressed space no bar touches the other bars. By disconnecting some bars or cables the shell is disassembled and can be transferred to another place for re-erection. A model of a tensegric shell has been presented already (2).

Tensegric shells were developed from tensegric bodies (1), fundamentally the tensegric shells are similar to the well known one skin pneumatic shells. In the case of a pneumatic shell the nonpermeable envelope of the shell is stabilized and the shell gets its proper shape when it is prestressed by pressurized air, whereas in the tensegric shell the cable net, which is related to the pneumatic shell envelope, is stabilized and the shell gets its proper shape when it is prestressed by lengthening the properly arranged bars connected to the net nodes. The advantage of the tensegric shell is that no special envelope and no constant pumping is required and there are no problems considering openings as in the case of pneumatic shells.

In this work the behavior of a determinate tensegric shell when it is prestressed and under external load is studied and the shell properties are considered.

FIXING AND FITTING NET TO DETERMINATE TENSEGRIC SHELL

At the first stage of designing a tensegric shell the nature of the tensegric net to be used in the structure must be fixed. Various nets and possible arrangements of bars suitable for tensegric shells were described earlier (2). Of particular interest are the regular tensegric shells in which at each node the same number of cables are joined to the bar. In regular determinate tensegric shells, where the number of bars, cables, and the reactions along the shell

¹Lect., Dept. of Civ. and Struct. Engrg., University College, Cardiff, United Kingdom.

Note.—Discussion open until March 1, 1982. To extend the closing date one month, a written request must be filed with the Manager of Technical and Professional Publications, ASCE. Manuscript was submitted for review for possible publication on January 15, 1981. This paper is part of the Journal of the Structural Division, Proceedings of the American Society of Civil Engineers, ©ASCE, Vol. 107, No. ST10, October, 1981. ISSN 0044-8001/81/0010-2029/\$01.00.

edge is equal to three times the number of nodes, there are five cables joined to the bar at each node. An example of a net to be used in determinate tensegric shells is shown in Fig. 1.

After the nature of the net has been fixed it must be fitted to the geometry of the specific shell under design and the length of the different bars and cables must be found appropriately. In Fig. 2 the tensegric net shown in Fig. 1 is fitted into a spherical determinate tensegric shell. This is the initial geometrical configuration of the tensegric shell. Because the shell has no continuous rigid supporting elements, constructing a tensegric shell with bars and cables of the length analyzed from the initial geometry leads to a loose structure without a definite shape which is of no use. In order to stabilize the structure and to give it a definite shape the structure must be prestressed.

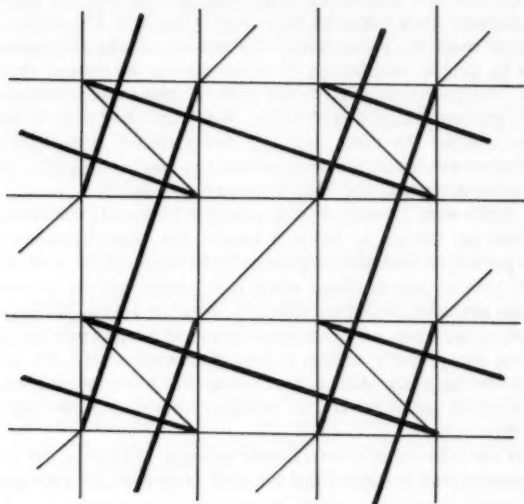


FIG. 1.—Net and Bars Arrangement in Case of Determinate Tensegric Shell

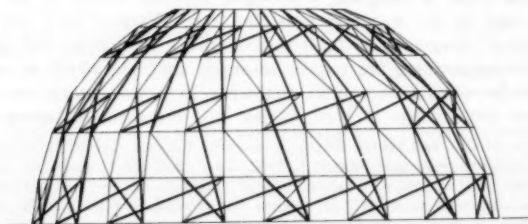


FIG. 2.—Spherical Determinate Tensegric Shell

BEHAVIOR OF DETERMINATE TENSEGRIC SHELL UNDER PRESTRESSING

The prestressing can be done by lengthening some of the bars or by shortening some of the cables. The prestressing changes the geometry of the tensegric shell from the initial geometry to the prestressed geometry and introduces inner forces to the cables and bars of the structure. Only tensegric shells in which prestressing induces tensile forces in the cables and compression in the bars are suitable. A tensegric shell achieves a stable geometry when equilibrium between the inner forces in the cables and bars and the reactions along the shell edges due to the prestressing at all the nodes is established. The inner forces at every node of the shell should satisfy equilibrium of forces in the x , y , and z directions, three equilibrium equations per node. Writing all these equilibrium equations from all the shell nodes in a matrix form yield to:

$$\bar{\mathbf{A}} \cdot \bar{\mathbf{P}} = 0 \quad (1)$$

in which $\bar{\mathbf{P}}$ = the vector of the inner forces in the cables and bars of the tensegric shell and the reactions along the shell edges; and $\bar{\mathbf{A}}$ = the matrix related to the geometrical configuration of the prestressed tensegric shell. It is convenient to assume that during the prestressing the geometry of the tensegric shell is changed from the initial geometry to the prestressed geometry. A node that was located at x_i , y_i , and z_i when the tensegric shell has its initial geometry has a displacement of u_i , v_i , and w_i , respectively, when it takes the prestressed configuration. Matrix $\bar{\mathbf{A}}$ is a function of x_i , y_i , z_i , u_i , v_i , and w_i of all the shell nodes. Eq. 1 has nontrivial solutions only if the rank of $\bar{\mathbf{A}}$ is less than the number of unknowns, in the case of a determinate tensegric shell $\bar{\mathbf{A}}$ is a determinant and this condition implies that:

$$\det \bar{\mathbf{A}} = 0 \quad (2)$$

In the case where the nodal displacements are small, matrix $\bar{\mathbf{A}}$ can be written in the form of:

$$\bar{\mathbf{A}} = \bar{\mathbf{A}}^0 + \bar{\mathbf{A}}' \quad (3)$$

in which $\bar{\mathbf{A}}^0$ = the matrix considering the initial geometry of the tensegric shell and it is a function of x_i , y_i , and z_i of the shell nodes only; $\bar{\mathbf{A}}'$ = the linear matrix of the nodal displacements u_i , v_i , and w_i . Considering Eq. 3 and ignoring second order terms Eq. 2 takes the following form:

$$\det \bar{\mathbf{A}}^0 + \sum_i \sum_j C_{ij}^0 a_{ij} = 0 \quad (4)$$

in which C_{ij}^0 = the co-factor i, j in determinant $\bar{\mathbf{A}}^0$; and a_{ij} = the element i, j of $\bar{\mathbf{A}}'$ matrix. Eq. 4 indicates a linear relationship between the nodal displacements, u_i , v_i , and w_i . The displacements of the shell nodes during the prestressing are restricted by the fact that the length of some cables and bars is not changed during the prestressing. If the length of a member k connecting nodes i and j is not changed during the prestressing; the displacement of nodes i and j , in the case of small nodal displacements have to satisfy Eq. 5:

$$(x_i - x_j)(u_i - u_j) + (y_i - y_j)(v_i - v_j) + (z_i - z_j)(w_i - w_j) = 0 \quad (5)$$

It seems most convenient to impose some restrictions on the distortion of

the initial geometry of the tensegric shell due to prestressing, one way is by seeking for a minimum general distortion which implies that:

$$\sum_i (u_i^2 + v_i^2 + w_i^2) = \text{Min} \quad (6)$$

the summation in Eq. 6 is on all the moveable shell nodes.

Eqs. 4 and 5 indicate the dependence between the nodal displacements. By considering the linear Eqs. 5 and 6, Eq. 6 yields to an appropriate set of linear equations from which the independent nodal displacements due to the prestressing can be found.

BEHAVIOR OF DETERMINATE TENSEGRIC SHELLS UNDER EXTERNAL LOADS

The forces, \bar{F} , induced in the bars and cables of the shell by an external load, \bar{L} , applied on it can be found by using Eq. 7:

$$\bar{A} \bar{F} = \bar{L} \quad (7)$$

in which \bar{A} = a matrice related to the geometry of the prestressed shell. Because of the fact that the geometry of the tensegric shell was achieved by prestressing, only a few loading cases are related to a consistent set of the linear equations given by Eq. 7. In the general loading case this set of the linear equations is not consistent; a fact which indicates that the tensegric shell cannot sustain the external loads having the geometry achieved by the prestressing. In these loading cases the geometry of the shell changes until equilibrium is established in all the nodes which implies that:

$$\bar{B} \bar{F} = \bar{L} \quad (8)$$

in which \bar{B} = the matrice related to the new geometry of the tensegric shell. It is assumed that during the change in the geometry of the shell a node, i , located at x_i , y_i , and z_i in the shell prestressed geometry has been moved by u_i , v_i , and w_i . In the case of a small nodal displacement the inner forces, f_k , in member k connecting nodes i and j is given by Eq. 9:

$$f_k = p_k + f'_k; \quad f'_k = \frac{2E_k A_k}{\ell_k^0} [(x_i - x_j)(u_i - u_j) + (y_i - y_j)(v_i - v_j) + (z_i - z_j)(w_i - w_j)] \quad (9)$$

in which p_k = the inner prestressing force; E_k and A_k = the elasticity and cross-section; and ℓ_k^0 = the length of member k in the prestressed geometry. The load vector can be written as:

$$\bar{F} = \bar{P} + \bar{F}' \quad (10)$$

In the case of a small nodal displacement \bar{B} takes the form of:

$$\bar{B} = \bar{A} + \bar{B}' \quad (11)$$

in which \bar{B}' = a linear function of the nodal displacements.

Considering Eqs. 10 and 11 and ignoring second order effects Eq. 8 takes the form of:

$$\bar{A} \bar{F}' + \bar{B}' \bar{P} = \bar{L} \quad \dots \quad (12)$$

which is a set of linear equations of the nodal displacements of the tensegric shell under the given load.

The prestressing is to the extent that proper tensile forces are left in the cables under the expected external loads.

REVIEW

The method of proper arrangement of the bars and cables in the case of a determinate tensegric shell were described. It was shown that to stabilize the shell prestressing is required.

The condition for a stable tensegric shell was formulated and the method of analysing the shape and the inner forces of the prestressed tensegric shell was presented.

It was shown that most types of external loads when applied on the determinate tensegric shell will cause a considerable geometrical distortion of the shell. The method of analyzing these distortions is considered in the work.

APPENDIX.—REFERENCES

1. Emmerich, D. G., "Morphology et Structures," *l'Architecture d'Aujourd'hui*, Vol. 160, Paris, France, 1972, pp. 20-24.
2. Vilnay, O., "Structures made of infinite regular tensegric nets," *IASS Bulletin No. 63*, Vol. XVIII-1, Apr., 1977, pp. 51-57.

DISCUSSIONS

Discussions may be submitted on any Proceedings paper or technical note published in any *Journal* or on any paper presented at any Specialty Conference or other meeting, the *Proceedings* of which have been published by ASCE. Discussion of a paper/technical note is open to anyone who has significant comments or questions regarding the content of the paper/technical note. Discussions are accepted for a period of 4 months following the date of publication of a paper/technical note and they should be sent to the Manager of Technical and Professional Publications, ASCE, 345 East 47th Street, New York, N.Y. 10017. The discussion period may be extended by a written request from a discussor.

The original and three copies of the Discussion should be submitted on 8-1/2-in. (220-mm) by 11-in. (280-mm) white bond paper, typed double-spaced with wide margins. The length of a Discussion is restricted to two *Journal* pages (about four typewritten double-spaced pages of manuscript including figures and tables); the editors will delete matter extraneous to the subject under discussion. If a Discussion is over two pages long it will be returned for shortening. All Discussions will be reviewed by the editors and the Division's or Council's Publications Committees. In some cases, Discussions will be returned to discussors for rewriting, or they may be encouraged to submit a paper or technical note rather than a Discussion.

Standards for Discussions are the same as those for Proceedings Papers. A Discussion is subject to rejection if it contains matter readily found elsewhere, advocates special interests, is carelessly prepared, controverts established fact, is purely speculative, introduces personalities, or is foreign to the purposes of the Society. All Discussions should be written in the third person, and the discussor should use the term "the writer" when referring to himself. The author of the original paper/technical note is referred to as "the author."

Discussions have a specific format. The title of the original paper/technical note appears at the top of the first page with a superscript that corresponds to a footnote indicating the month, year, author(s), and number of the original paper/technical note. The discussor's full name should be indicated below the title (see Discussions herein as an example) together with his ASCE membership grade (if applicable).

The discussor's title, company affiliation, and business address should appear on the first page of the manuscript, along with the *Proceedings* paper number of the original paper/technical note, the date and name of the *Journal* in which it appeared, and the original author's name.

Note that the discussor's identification footnote should follow consecutively from the original paper/technical note. If the paper/technical note under discussion contained footnote numbers 1 and 2, the first Discussion would begin with footnote 3, and subsequent Discussions would continue in sequence.

Figures supplied by the discussor should be designated by letters, starting with A. This also applies separately to tables and references. In referring to a figure, table, or reference that appeared in the original paper/technical note use the same number used in the original.

It is suggested that potential discussors request a copy of the *ASCE Authors' Guide to the Publications of ASCE* for more detailed information on preparation and submission of manuscripts.

VERTICAL VIBRATION ANALYSIS OF SUSPENSION BRIDGES^a

Discussion by Hassan I. A. Hegab²

The author presented an analytical investigation, supported by field measurements, on the free vertical vibration of suspension bridges. The first statement of the paper talks about the First Tacoma Suspension Bridge which failed, in 1940, by the first antisymmetric torsional mode of vibration. Actually, the great majority of authors solve the suspension bridge as a plane structure loaded symmetrically about its longitudinal center line. However, a few authors (12,13,14) solve the suspension bridge as a three-dimensional structure considering the torsional stiffness of the deck and making allowance for asymmetric loadings.

Although the torsional stiffness of the bridge deck is taken into consideration in his analysis (Eq. 11), the author did not try to offer any analytical or even experimental results of torsional vibration, as if the structure is a plane structure with no torsional stiffness. In other words, the author did not make use of the torsional stiffness of the bridge and his numerical example does not show its value. Rather, the author presented a separate paper (3) for free torsional vibrations.

The writer has the following comments:

1. Eq. 1 may be written in a simpler form as follows

$$Y(x) = 4 \left(\frac{f}{l} \right) \left[x - \frac{x^2}{l} \right] \dots \dots \dots (70)$$

in which (f/l) is the sag-span ratio of the cable.

However, W_c defined by the author should be the "average" dead weight of the cable per unit span length (and not per unit cable length) since the cable profile is parabolic under dead load.

2. In his sixth assumption (on p. 2054) the author states that the suspenders "are assumed to remain vertical during the vibration," while the example [Fig. 1(a)] shows some inclination.

3. The integral of Eq. 4 is given by Timoshenko (15) as

$$\int_0^l \left(\frac{ds}{dx} \right)^3 dx = l \left\{ \frac{1}{4} \left[\frac{5}{2} + 16 \left(\frac{f}{l} \right)^2 \right] \left[1 + 16 \left(\frac{f}{l} \right)^2 \right]^{1/2} + \frac{3}{32} \log_e \left[4 \left(\frac{f}{l} \right) + \left\{ 1 + 16 \left(\frac{f}{l} \right)^2 \right\}^{1/2} \right] \right\} \dots \dots \dots (71)$$

while it is given by the writer (13) in a much simpler form as

^aOctober, 1980, by Ahmed M. Abdel-Ghaffar (Proc. Paper 15759).

²Lect., Faculty of Engrg., Ain Shams Univ., Abbasia, Cairo, Egypt.

$$\int_0^l \left(\frac{ds}{dx} \right)^3 dx = l \left[1 + 8 \left(\frac{f}{l} \right)^2 \right] \dots \dots \dots (72)$$

in which $(ds/dx) = \sec \phi$ (and not $\cos \phi$ as stated by the author on p. 2054). Also the integral of Eq. 6 is given by the writer as

$$\int_0^l \left(\frac{ds}{dx} \right)^2 dx = l \left[1 + \frac{16}{3} \left(\frac{f}{l} \right)^2 \right] \dots \dots \dots (73)$$

4. Eq. (11) may alternatively be written as

$$V_{sv}(t) = \frac{1}{2} \int_0^l EI \left(\frac{d^2 v}{dx^2} \right)^2 dx + \frac{1}{2} \int_0^l G \mu \cdot \left[\frac{d}{dx} \left(\frac{dv}{dx} \right) \right]^2 dx \dots \dots \dots (74)$$

in which $d^2 v/dx^2$ = curvature of the bridge deck = M/EI ; $d/dx (dv/dx)$ = twist of the bridge deck.

APPENDIX.—REFERENCES

12. Fukuda, T., "Multispan Suspension Bridges Under Torsional Loading," *Proc. Japan Society of Civil Engineers*, No. 242, Tokyo, Japan, Oct., 1975.
13. Hegab, H. I. A., "Statics and Dynamics of Suspension Bridges with Notes on Suspension Cables and Nets," thesis presented to the University of Tasmania, at Hobart, Australia, in 1977, in partial fulfillment of the requirements for the degree of Doctor of Philosophy.
14. Sih, N., "Torsion Analysis for Suspension Bridges," *Journal of the Structural Division*, ASCE, Vol. 83, No. ST6, Proc. Paper 1431, Nov., 1957, 1431-1-1431-81.
15. Timoshenko, S., "The Stiffness of Suspension Bridges," *Transactions, ASCE*, Vol. 94, Paper No. 1732, 1930, pp. 377-391.

EFFECTS OF FIRE ON REINFORCED CONCRETE MEMBERS^a

Discussion by I. D. Bennetts³ and I. R. Thomas⁴

This paper has raised a number of important considerations with regard to the prediction of the behavior of concrete structures in fire. The authors have ably presented the advantages of analytical methods of estimating fire resistance over the use of traditional fire resistance tests.

The various approaches which have been used to estimate the fire resistance of concrete members are summarized in Table 2 and have been numbered from one to ten in the Table. Approach 1 is the standard fire test. Approaches 2,

^aNovember, 1980, by B. Ellingwood and J. R. Shavers (Proc. Paper 15802).

³Research Officer, The Broken Hill Proprietary Co., Ltd., Melbourne Research Labs., 245-273 Wellington Rd., Clayton, Victoria 3168, Australia.

⁴Sr. Research Officer, The Broken Hill Proprietary Co., Ltd., Melbourne Research Labs., 245-273 Wellington Rd., Clayton, Victoria 3168, Australia.

3, and 4 are semianalytical methods based on experimentally determined temperature distributions. Approaches 9 and 10 are analytical methods which attempt to predict the behavior of the member in the standard fire test. The remaining approaches (5-8) are analytical methods which describe the behavior of a member in real fire conditions. To do this they combine prediction of the fire environment with the response of the member in that environment. These methods thus require information on the fire compartment (e.g., fire load, ventilation, emissivity, etc.).

The modelling of the structural response ranges from simple flexural strength approaches (2-5, and 10) to the use of full constitutive relationships for steel and concrete (Approach 8).

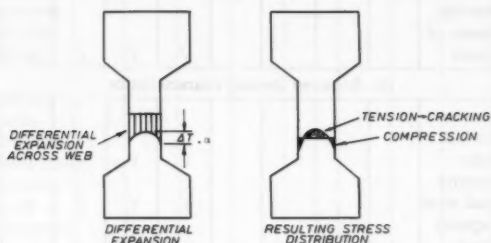


FIG. 13.—Differential Thermal Expansion across the Webs of Concrete Beams

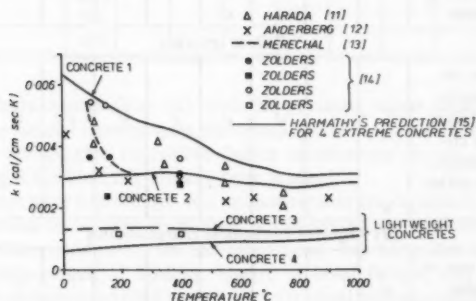


FIG. 14.—Variable Thermal Conductivity for Normal Weight Concrete

We believe that the authors are correct in suggesting that care should be exercised in using some of the simpler design methods, as it is possible that premature compression failure may occur due to the influence of elevated temperatures on the concrete compression zone. Other problems which could negate the validity of some of these simpler methods are those of spalling, interaction of shear and bending, (25), bond failure (27), and longitudinal splitting along the beam web. This latter problem has been noted by European workers (19) and is thought to be due to the differential thermal expansion across the

TABLE 2.—Approaches to Assessment of Structural Performance in Fire

Factors relevant to assessment of stability (1)	Approach Number									
	1 (2)	2 (3)	3 (4)	4 (5)	5 (6)	6 (7)	7 (8)	8 (9)	9 (10)	10 (11)
(a) Required thermal environments										
Standard time temperature curve in standard furnace environment	✓	✓	✓	✓					✓	✓
Fire load and ventilation requirements of fire compartment					✓	✓	✓	✓		
(b) Required thermal characteristics										
Heat transfer characteristics (radiation and convection)					✓	✓	✓	✓	✓	✓
Thermal conductivity of concrete and steel					✓	✓	✓	✓	✓	✓
Specific heat capacity of concrete (and steel)					✓	✓	✓	✓	✓	✓
Experimentally determined isotherms as function of time		✓	✓	✓						
(c) Failure criterion										
Member failure criterion—failure to satisfy equilibrium			✓	✓	✓	✓	✓	✓	✓	✓
Member failure criterion—maximum deflection or deflection rate	✓									
(d) Required mechanical characteristics										
Fire resistance test of full size member	✓									
Critical temperature of steel (based on previous assessments using 8 and 9)		✓								
Reinforcement:										
Influence of temperature on proof or ultimate stress			✓	✓	✓	✓	✓	✓	✓	✓
Influence of temperature on stress-strain relationship (instantaneous)						✓	✓	✓	✓	

TABLE 2.—Continued

(1)	(2)	(3)	(4)	(5)	(6)	(7)	(8)	(9)	(10)	(11)
Thermal expansion characteristics						✓	✓	✓	✓	
Thermal creep behavior							✓	✓	✓	
Concrete:										
Influence of temperature on concrete crushing strength				✓	✓	✓	✓	✓	✓	✓
Influence of temperature on concrete stress-strain relationship (instantaneous)						✓	✓	✓	✓	
Thermal expansion characteristics						✓	✓	✓	✓	
Use of full constitutive equations taking into account stress history, time and temperature								✓		
References illustrating approach	Standard fire test	(24)	(20)	(21)	(16)			(17)	(6)	(28)

webs of concrete beams (Fig. 13) with the resulting stress field causing the cracking. If the simpler flexural strength approaches are to be used then safeguards must exist to ensure that alternative failure mechanisms do not occur. Some progress along these lines has already been made.

As the authors have pointed out, fire resistance tests are expensive. In addition, it is only practical to test the simplest of structures as it is difficult to simulate the real boundary conditions. On the other hand, full scale fire tests indicate the level of importance of spalling, shear, or bond failure, and furthermore such tests do not require detailed knowledge of thermal or heat transfer properties.

Although there are limitations and problems with the standard fire test, it seems to the writers, that there are also difficulties with the use of analytical methods, particularly the more sophisticated methods. The calculation of temperatures throughout the member cross section requires the use of reliable thermal properties. It is well known that it is difficult to determine experimentally the heat capacity of concrete. The thermal conductivity for normal weight concrete is variable (Fig. 14) and appears to be not only a function of concrete type but also testing technique (17). If the concrete under consideration is prone to spall, or if the concrete cover tends to crack and fall away as the member deflects, then a theoretical heat flow analysis will underestimate the temperatures within the cross section.

Some of the difficulties mentioned above for heat flow analysis of concrete members can be overcome by "calibrating" the theoretical model (Approaches 9 and 10) against the results of fire tests (Approach 1). Thus, one can choose thermal properties for the concrete which seem to result in good correlation between experimentally and theoretically determined temperatures. It is difficult to see, however, a means of checking the results obtained using Approaches 5-8.

A problem with the use of analytical techniques to predict temperatures within a member is the availability of sufficient data to properly model the heat transfer across the boundary of the member. This depends on both convection and radiation and the writers question the accuracy with which the temperature dependent parameters such as the resulting emissivity and the heat transfer coefficient can be specified.

The use of the most sophisticated structural analysis technique (Approach 8) relies on empirically based constitutive relationships for both steel and concrete (18). The determination of such relationships for concrete involves a very large experimental programme and the writers question the applicability of these constitutive relationships to other concretes. Approaches 5-10 assume that perfect bond exists between concrete and steel and do not predict the member shear-moment or shear strength. For some structures therefore, care must be exercised in using these methods to predict fire resistance.

The engineering goal must be to predict the response of structures in the real fire environment. This combines prediction of the thermal environment, prediction of the thermal response of the structure to that environment, and prediction of the structural behavior. This is the intention of methods 5-8. The writers would appreciate the authors comments on how methods 5-8 can be validated with regard to both the thermal and structural response in the real fire situation. Does sufficient data exist to allow this to be achieved?

APPENDIX.—REFERENCES

16. Anderberg, Y., "Analytical Fire Engineering Design of Reinforced Concrete Structures Based on Real Fire Characteristics," Proceedings of the Eighth Congress of the Federation Internationale de la Pre Contrainte, Apr. 30-May 5, 1978, pp. 112-123.
17. Anderberg, Y., "Fire-Exposed Hyperstatic Concrete Structures—An Experimental and Theoretical Study," *Bulletin 55*, Lund Institute of Technology, Lund, Sweden, 1976.
18. Anderberg, Y., and Thelandersson, S., "Stress and Deformation Characteristics of Concrete at High Temperatures," *Bulletin 54*, Division of Structural Mechanics and Concrete Construction, Lund Institute of Technology, Sweden, 1976.
19. Boon, J., "Fire Resistance of Prestressed Concrete Beams," *Heron*, Vol. 21, No. 1, 1976.
20. "Design for Fire Resistance of Precast Prestressed Concrete," Report of PCI Fire Committee, 1977.
21. "Design and Detailing of Concrete Structures for Fire Resistance," Interim Guidance by a Joint Committee of the Institution of Structural Engineers and the Concrete Society, The Institution of Structural Engineers, Apr., 1978.
22. Harada, T., Takeda, J., Yamane, S., and Furumura, F., "Strength Elasticity and Thermal Properties of Concrete subjected to Elevated Temperatures," Concrete for Nuclear Reactors, *ACI Special Publication SP34*, paper 21, 1972, pp. 377-401.
23. Harmathy, T. Z., "Thermal Properties of Concrete at Elevated Temperatures," *Journal of Materials*, JMLSA, Vol. 5, No. 1, Mar., 1970, pp. 47-74.
24. Kordina, K., Ehm, H., et al., "Experimentelle untersuchungen ueber erwaermungsvor-

- gaenge," *Deutscher Ausschuss für Stahlbeton*, No. 230, Germany, 1975, pp. 1-42.
25. Krampf, L., "Investigations on the Shear Behaviour of Reinforced Concrete Beams Exposed to Fire," Reprint from *Forschungsbeiträge für die Baupraxis*, (Ed. J. Eibel), 1979.
 26. Merechal, J. C., "Thermal Conductivity and Thermal Expansion Coefficients of Concrete as a Function of Temperature and Humidity," *ACI Special Publication SP34*, paper 49, 1972, pp. 1047-1057.
 27. Morley, P. D., and Royles, R., "The Influence of High Temperature on the Bond in Reinforced Concrete," *Fire Safety Journal*, 2(1979/1980), pp. 243-255.
 28. Salse, E., and Lin, T. D., "Structural Fire Resistance of Concrete," *Journal of the Structural Division*, ASCE, Vol. 102, No. ST1, Proc. Paper 11835, Jan., 1976, pp. 51-63.
 29. Zolders, N. G., "Thermal Properties of Concrete under Sustained Elevated Temperatures," *ACI Special Publication SP25*, Temperature and Concrete, 1971, pp. 1-31.

SPACE TRUSS STUDIES WITH FORCE LIMITING DEVICES^a

Discussion by E. A. Smith,³ M. ASCE

The authors present some interesting experimental results that can increase our knowledge about space truss behavior and give some insights into the difficulties and potentialities of Force Limiting Devices. This writer has also been studying space truss behavior and has a number of comments and questions regarding the authors' work.

This writer agrees with the authors' observations about the effect of brittle-type post-buckling characteristics of transition length struts on the behavior of the total system, which can also be of brittle-type. Lack of fit will prestress the members, some favorably, and advance or delay the achievement of the member peak load, the buckling load, thus causing the premature initiation of failure of the total system. However the authors' results seemed to indicate that even accounting for lack of fit, none of the monitored members achieved the buckling loads obtained in the member tests. Kahn and Hanson have presented results (15) on tests of mild steel transition length struts that also fail to reach the predicted peak loads.

This writer believes that one reason for this phenomenon is the sensitivity of the peak load of the member to slight variations in the pre- and post-buckling behavior. Rosen and Schmit have shown (16) that the effective axial stiffness of a sinusoidally pre-bent member is given by

$$k = \frac{\left(\frac{AE}{L} \right)}{\left[1 + \frac{1}{4} \left(\frac{e_0}{r} \right)^2 \frac{(2 - \rho)}{(1 - \rho)^2} \right]} \dots \dots \dots (1)$$

^aNovember, 1980, by A. Hanoar and L. C. Schmidt (Proc. Paper 15808).

³Asst. Prof., Civ. Engrg. Dept., Univ. of Connecticut, Storrs, Conn. 06268.

in which AE/L = the axial stiffness of a perfect member; e_0 = the maximum initial eccentricity; r = the radius of gyration; and ρ = the ratio of the applied load to the buckling load.

L. C. Schmidt has derived a similar expression for eccentrically loaded members. The stiffness begins to decrease rapidly when ρ is greater than about 0.8. If inelasticity occurs, then the effective buckling load decreases causing an additional increase in ρ and decrease in stiffness. The effective axial stiffness therefore is quite sensitive to the effect of the initial eccentricities as the peak load is approached. Because of the steepness of the post-buckling response curve, the peak load at the intersection of the pre and post buckling responses can decrease considerably for small changes in the initial eccentricity. Higginbotham and Hanson have showed (14) that it is possible to considerably reduce the percent deviation of the maximum compressive load from the analytical solution of a member by accounting for initial curvatures.

Although the authors' stiffening of the joints would reduce the effect of jackknifing, it would not eliminate initial eccentricities that can lead to the above described imperfection sensitivity. In addition, it should be noted that the stiffening of joints did not appear to allow unbuckled members to attenuate buckling of adjacent members. For example, in the final test, #10, members 9, 1, 10, and 3 all failed at the same external load although only 9 and 10 were rigidly connected to lower stressed members.

While the authors' claim to have tested a "statically determinate" subassembly, without the assumption of symmetry, the assemblage is clearly both externally and internally indeterminate. If the reaction points are unequally stiff, or if initial slack existed in the supports, prestress will occur. How did the authors support the structure to ensure that all the reactions were equal and thus not contributing to prestress and do they have any initial force measurements for the statically determinate subassemblages? Such data would be helpful to interpreting the "determinate" and indeterminate assemblages.

APPENDIX.—REFERENCES

14. Higginbotham, A. B., and Hanson, R. D., "Axial Hysteretic Behavior of Steel Members," *Journal of the Structural Division*, ASCE, Vol. 102, No. ST7, Proc. Paper 12245, July, 1976, pp. 1365-1381.
15. Kahn, L. F., and Hanson, R. D., "Inelastic Cycles of Axially Loaded Steel Members," *Journal of the Structural Division*, ASCE, Vol. 102, No. ST5, Proc. Paper 12111, May, 1976, pp. 947-959.
16. Rosen, A., and Schmit, L. A., "Design Oriented Analysis of Imperfect Truss Structures—Part 1," *International Journal for Numerical Methods in Engineering*, Vol. 14, No. 9, 1979, pp. 1309-1321.

COLUMN BASE PLATES WITH AXIAL LOADS AND MOMENTS^a

Discussion by Grover H. Bays,³ M. ASCE

The authors are to be congratulated for this very fine study and contribution to the understanding of the effects of axial and undirectional bending moments on the concrete, base plates, and properly designed anchor bolts; using two stress grades of steel bolts of various diameters, and various degrees of eccentricity.

Due to the type of "through-bolt" anchor, of course, the effect of an end-anchorage failure could not be produced. Do the authors know at approximately what percent of bolt working loads the bond break-down occurred? Perhaps less credence should be given to anchor bolt bond allowance.

Two directional (or diagonal) bending was not included. Are the two *preferred* methods of analysis practical or indeed safe approaches for this problem?

Did the authors consider the possible benefit, e.g., greater base fixity, that would occur from use of thicker base plates? The writer believes that the plate deformations, then, would not be too inconsistent with the "strain compatibility approach," (section at bottom of base plate remaining plane after bending). An analysis of the 13 test conditions show that (in theory) the edge pressure on the concrete will never be greater than $0.56 f'_c$, which is well within the permissible $0.7 f'_c$ of A.I.S.C. Specifications, when using strain compatibility. While it is generally true that failure load, based on anchor bolt achieving its full working tension, is decreased about 63% (see author's conclusion number 3) however, for test specimens 3 and 4 values of P_{ws} increased to 13.9 kips and 10.7 kips, or 20% and 87% increments respectively (1 kip = 4.45 kN) when compared to values in Table 3, column 3.

Perhaps an additional measure to provide greater base fixity of columns would be to keep anchor bolts shorter while providing end-anchorage of bolt to carry full bolt tension.

Cannot strain compatibility be considered consistent within the stress range of working loads, as opposed to failure loads?

The authors' method of measuring concrete bearing area after the test seems infallible. However, as they indicate, the use of reinforcement in the pedestal should further reduce the chance of concrete failures.

Finally, does the large concrete stress of specimen 4, Table 6, represent a "break-down" of the ultimate strength method for that range of small anchor bolt size and large eccentricity?

The writer looks forward to the possibilities of more rigid guidelines to column base design, but would also plead for a further look at the practicality of the strain compatibility concept in such areas as maximum base fixity and biaxial bending.

^aNovember, 1980, by John T. DeWolf and Edward F. Sarisley (Proc. Paper 15823).

³Design Engr., Lehigh Structural Steel Co., Allentown, Pa.

How can we achieve a designer's "honeymoon" relationship between A.I.S.C. and A.C.I. at the base plate supports of steel frames? It would appear from these studies and tests that this has not yet occurred.

EFFECT OF OPENINGS ON LATERAL BUCKLING OF BEAMS^a

Discussion by Narayanan Subramanian³

The writer would like to appreciate the authors for writing an interesting paper, which provides information about the lateral buckling of beams with openings. However, the writer would like to make the following observations.

1. The authors suggest the use of the formula suggested by Timoshenko for predicting the lateral torsional buckling load of the cantilever beam, after making allowances for the openings. This formula, Eq. 1, is applicable only in the elastic range, i.e., the formula is applicable only if the quantity t^2/hL is very small (5). The authors have chosen the beams, such that the value of t^2/hL ranges between 7.6×10^{-4} and 1×10^{-3} . But in practice, the value of t^2/hL may be greater than those considered by the authors and thus the buckling in the inelastic range should be considered.

2. The Eq. 1 should be read as

$$P_0 = \frac{\gamma}{L^2} \sqrt{GJEI_z} \quad \text{and not as} \quad P_0 = \gamma \sqrt{\frac{GJEI_z}{L^2}} \dots \dots \dots (5)$$

3. Usually it is necessary to consider lateral buckling only in the case of a very narrow rectangular cross section in which t/h = a small quantity. (The authors have considered beams having t/h values ranging from 0.06–0.08). Theoretically buckling may occur also in the case where t/h is not very small but where the length L is very large. In this case a large deflection in the plane of the web will be produced before lateral buckling occurs, and this deflection should be considered in the derivation of the differential equations of equilibrium. It has been shown that in these cases the constant value of $\gamma = 4.013$ can not be used (5). This constant will then depend on the ratio b/h . Dinnik and Federhofer have shown that for values of b/h equal to 1/10, 1/5 and 1/3, the value of γ will be equal to 4.085, 4.324, and 5.030, respectively (5).

4. The formula given in Eq. 1 is applicable only when the load, P , is applied at the centroid of the cross section. It has been shown that the loads applied at the level of the top flange at points free to twist represent a particularly

^aDecember 1980, by Alexander Coull and Maria C. Alvarez (Proc. Paper 15874).

³Alexander von Humboldt Fellow, Fachgebiet Stahlbau, Tech. Univ. of Berlin, Berlin, West Germany.

severe condition for cantilevers (6). It will be useful to consider this case also since in many practical cases, the loads will be applied at the top flange.

APPENDIX.—REFERENCE

6. Nethercot, D. A., "The Effective Lengths of Cantilevers Governed by Lateral Buckling," *The Structural Engineer*, Vol. 51, No. 5, May, 1973, pp. 161-168.

WIND-INDUCED LOCK-IN EXCITATION OF TALL STRUCTURES^a

Discussion by A. Kareem,³ M. ASCE

The authors have presented an interesting and useful procedure for determining the behavior of a tall structure subject to wind-induced lock-in excitation. The writer has obtained some of the results outlined by the authors, e.g., an increase in the reduced velocity results in a change in the nature of the crosswind excitation. At lower velocities the forcing function exhibits randomness; however, as the reduced velocity is increased, it tends to become closer to harmonic plus a random noise. Furthermore, studies conducted by the writer have indicated that there is an apparent decrease in the net damping, as the reduced velocity is increased. It would be interesting to learn if the authors tried to quantify any change in the net damping in their study.

The authors have arranged the equation of motion such that all the motion dependent terms are placed on the right hand side of the equation. This has resulted in different spectral curves as the reduced velocity is increased (Fig. 4). In Eq. 2, if appropriate adjustments for the change in the net damping value of the system at various reduced velocities are made, all the curves in Fig. 4 may collapse on one curve. A simplified expression for the amplitude dependent aerodynamic damping, as a function of reduced velocity, can be derived from the experimental data. An extension of forced vibration theory would permit prediction of response amplitudes, by introducing amplitude dependent aerodynamic damping, even when the motion induced effects are dominant. A similar approach has been reported in Refs. 22 and 23.

The model proposed by the authors is essentially based on a forced vibration theory. The uniqueness of the forcing function is not necessarily insured, since it is obtained by an inverse approach. An accurate assessment of the system properties is foremost for the success of this technique. It would be very beneficial for the readers to know whether the model was free to oscillate in the two principal axes of motion or the alongwind direction was restricted. Experiments conducted by the writer have indicated that the behavior of a model is quite

^aJanuary, 1980, by Kenny C. S. Kwok and William H. Melbourne (Proc. Paper 15976).

³Asst. Prof. of Civ. Engrg., Cullen College of Engrg., Univ. of Houston, Houston, Tex. 77004.

different in these configurations. Furthermore, the results have suggested that the redistribution of energy, imparted to the structure by the wind-structure interaction, from one principal axes to another has the tendency to limit the response amplitude, thereby, imparting indirect damping to the system. This behavior is more pronounced for a structure with equal natural frequencies in the two principal directions.

Authors have briefly commented on Reynolds number dependence of the flow around smooth cylinders. The question of Reynolds number similitude is important for practical design purposes. The force coefficients are highly dependent upon Reynolds number, aspect ratio, surface roughness, turbulence intensity and shear in the approach flow. A wide variation of forces can be measured on apparently identical cylinders in different test facilities. One of the major difficulties is the simulation of high Reynolds number flow around wind tunnel models of circular crosssection. Augmenting the model surface with discrete or homogeneous, or both, roughness elements may contribute towards simulation of the features of high Reynolds number flow. In this manner, a wake may be developed artificially, at subcritical Reynolds numbers, which is similar to the one naturally produced at the fullscale Reynolds number. A literature survey indicates that when cylinder oscillates, the flow field is different from that of a stationary cylinder and may have less dependence on the Reynolds number. In this manner small scale models of cylindrical structures could be employed to reproduce the dynamic behavior; nevertheless, the steady drag forces would be dependent on the Reynolds number. The authors have provided a good basic procedure, using small scale models, which can be further expanded to account for an appropriate Reynolds number simulation. The aforementioned simulation technique may allow a validation, or improvement of the valuable procedure outlined by the authors.

APPENDIX.—REFERENCE

23. Kareem, A., "Wind Excited Motion of Buildings," thesis presented to Colorado State University, at Fort Collins, Colo., in 1978, in partial fulfillment of the requirements for the degree of Doctor of Philosophy.

LOAD DISTRIBUTION AND DOUBLE SKIN WALL^a

Discussion by Theodore Stathopoulos,² M. ASCE

The author refers to the significance of the wind load distribution for the design of double skin wall panel constructions. He emphasizes the lack of relevant research information and indicates the large discrepancy between designs based

^aFebruary, 1981, by Raymond M. L. Ting (Proc. Paper 16055).

²Asst. Prof. of Engrg., Centre for Building Studies, Concordia Univ., 1455 de Maisonneuve Blvd. W., Montreal, Quebec, Canada H3G 1M8.

on commonly made assumptions with respect to the percentage of wind load acting on each component of the double skin wall system.

A significant parameter for the wind loads to be reasonably estimated is the permeability of both facia and liner components of the wall structure. The statement in the paper that "the liner construction is reasonably airtight, while the facia construction is not airtight" gives perhaps a preliminary indication but is not enough. Also under question is the assumption of static wind loading; the natural wind is always unsteady.

Based on his own measurements of both external and internal pressures acting on low-rise building (3), the writer has found that wind pressures on external wall surfaces are almost independent of the wall porosity whereas the internal pressures acting on the inside surface of the wall depend drastically on the wall porosity. This is true of mean and fluctuating components of both external and internal pressures. The implication is that the total wind load [(external pressure - internal pressure) \times area] acting on the wall is a function of the permeability of structure and the wall openings.

In the case of the double skin wall the situation is somewhat different because of the small internal volume of the spacing between facia and liner but in principle the problem remains the same. Pressure or suction on each side of the facia has to be found for the calculation of the design wind load.

Finally it is worth mentioning that the problem of wind load distribution on tiled roofs has been examined (4,5) and the reduction of wind pressures acting on permeable roof cladding in the presence of impermeable backing has been shown.

APPENDIX.—REFERENCES

3. Stathopoulos, T., Surry, D., and Davenport, A. G., "Internal Pressure Characteristics of Low-Rise Buildings Due to Wind Action," presented at the July 8-14, 1979, Fifth International Conference on Wind Engineering, held at Fort Collins, Colo.
4. Hazelwood, R. A., "Principles of Wind Loading on Tiled Roofs and their Application in the British Standard BS5534," *Journal of Wind Engineering and Industrial Aerodynamics*, Vol. 6, 1980, pp. 113-124.
5. Kramer, C., Gerhardt, H. J., and Kuster, H. W., "On the Wind Load Mechanism of Roofing Elements," presented at the June 14-16, 1978, 3rd Colloquium on Industrial Aerodynamics, held at Aachen, West Germany.

RESPONSE OF RC SHEAR WALL UNDER GROUND MOTIONS^a

Discussion by Medhi Saïdi,⁴ A. M. ASCE

The authors should be commended for studying a real structure, at least in the laboratory environment, to evaluate their timely analytical model. The writer would like to draw attention to the basic assumptions made in the analysis and the procedure used to evaluate the calculated responses.

The authors took into account several characteristics of reinforced concrete to model the structure "realistically." However, two important factors which generally reduce the "apparent stiffness" of reinforced concrete systems were not considered. One of these factors is stiffness degradation effects observed in cyclic testing of concrete specimens. Experimental studies have shown that concrete specimens loaded past the compressive strength exhibit reduction in stiffness upon unloading and reloading (Ref. 32). Exclusion of this factor in the analysis [Fig. 1(a)] results in an average structural stiffness larger than the actual stiffness of the structure.

The other important effect not included in the analysis is slippage of reinforcement caused by partial loss of bond. Deformations caused by bond slip usually constitute a significant portion of the total deformation. Ngo and Scordelis developed a linkage element to simulate bond slip in their finite element study of reinforced concrete beams (Ref. 30). Similar to stiffness degradation of concrete, bond slippage results in softening of the structure.

The fact that the model was "stiffer" than the actual test structure can be well observed in Table 2. The calculated maximum displacements are smaller than those measured, while the predicted base shear is larger than the measured value. Perhaps more detailed explanation would be possible if the measured response histories were reported in the paper.

The writer realizes that the inclusion of stiffness degradation and bond slip effects further complicates the analysis. However, these effects need to be taken into account either explicitly or implicitly, if a detailed complex analysis, whatever its use, is to be successful. To obtain only estimates of response, simpler models such as the Q-Model may be used (Ref. 31). In this model, bond slip is taken into account implicitly, while stiffness degradation is accounted for in the hysteresis model.

The response of the shear wall was found using the Q-Model. The properties of the equivalent "single-degree" oscillator are listed in Table 3. The assumed deflected shape is the same with the fundamental mode shape of the wall with cracked moment of inertia used for the first story. The primary force-displacement curve was calculated based on a static analysis of the wall subjected to lateral loads proportional with the height, applied at floor levels. The "yield" point

^aFebruary, 1981, by Awadh B. Agrawal, Leslie G. Jaeger, and Aftab A. Mufti (Proc. Paper 16061).

⁴Asst. Prof. of Civ. Engrg., Univ. of Nevada, Reno, Nev. 89557.

represents the load and displacement corresponding to the yielding of the wall at the base. The post-yielding branch was defined based on the loads causing a maximum strain of 0.003 in concrete. This strain was used only to define the slope, and not to limit forces.

TABLE 3.—Properties of SDOF Oscillator

Parameter (1)	Magnitude (2)
Equivalent weight	5.29 kip
Equivalent height	44.1 in.
Assumed deflected shape normalized with respect to top displacement:	
Top level	1.
Second level	0.57
First level	0.19
Top-level displacement at the "yield" point	0.17 in.
Base moment at the "yield" point	143 kip-in.
Slope of "post yielding" branch of the primary curve	95 kip-in./in.

Note: 1 in. = 25.4 mm; 1 kip = 4.45 kN; 1 kip-in. = 113.0 N·m.

TABLE 4.—Maximum Measured and Calculated Responses

Response (1)	Q-model (2)	Measured (3)	Author's best fit (4)
Double-amplitude displacement, in inches			
Top level	1.21	1.15	0.96
Second level	0.69	0.70	0.59
First level	0.23	0.30	0.24
Base shear, in kips	4.42	4.00	5.37
Base moment, in kips-inch	195	163	188

Note: 1 in. = 25.4 mm; 1 kip = 4.45 kN; 1 kip-in. = 113.0 N·m.

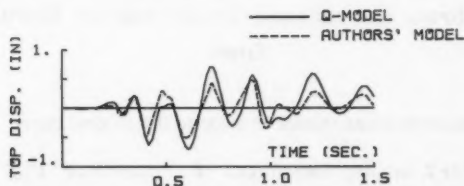


FIG. 10.—Top Level Response of Shear Wall

The base acceleration and the measured top-level displacement response were obtained from a crude digitization of the waveforms presented in Figs. 6 and 7. Although high-frequency accelerations could not be digitized accurately, they

were considered insignificant because their contribution to the response was expected to be small.

Fig. 10 represents the top-level response of the shear wall based on the Q-Model and the authors' model. It can be seen that the waveforms from both models were generally similar. With respect to the maximum responses (Table 4), the results from the Q-Model were either closer to the experimental data or approximately the same with the authors' results, even though the Q-Model is considerably simpler than the authors' model.

To evaluate the "usefulness" of the finite element model, the authors present the calculated responses for 1.5 sec and refer to measured response histories presented in Ref. 14 without reciting them. In addition, the calculated crack pattern for the first simulated earthquake is compared with the observed crack pattern after the third simulated earthquake. The writer believes that, to evaluate a complex nonlinear model, duration of the analysis should be sufficiently long to include both small-amplitude and large-amplitude responses, because some of the assumed characteristics of the model may influence these responses differently. With respect to crack patterns, it is inappropriate to compare the theoretical result for the first earthquake run with the experimental result for the third run, because cracks are generally progressive from one motion to the next.

APPENDIX.—REFERENCES

30. Ngo, D., and A. C. Scordelis, "Finite Element Analysis of Reinforced Concrete Beams," *ACI Journal*, Vol. 64, No. 3, Mar., 1967, pp. 152-163.
31. Saiidi, M., and M. A. Sozen, "Simple and Complex Models for Nonlinear Seismic Response of Reinforced Concrete Structures," Civil Engineering Studies, SRS 465, University of Illinois, Urbana, Ill., Aug., 1979.
32. Sinha, B. P., K. H., Gerstle, and L. G. Utlin, "Stress-Strain Relationships for Concrete Under Cyclic Loading," *ACI Journal*, Vol. 61, No. 2, Jan., 1964, pp. 195-211.

WIND SPEED DISTRIBUTIONS AND RELIABILITY ESTIMATES^a

Errata

The following corrections should be made to the original paper:

Page 1005, Table 2, heading: Should read " V_{Qn} " instead of " V_{Qn}^a "

Page 1005, Table 2, heading: Should read " $V_r = 0.10$ " instead of " $V_r = 1.10$ "

Page 1005, Table 2, column "Distribution," lines 1 and 5: Should read "Rayleigh" instead of "Rayleigh type I"

Page 1005, Table 2, column "Distribution," lines 3 and 7: Should read "Type I" instead of being blank

^aMay, 1981, by Emil Simiu, James J. Shaver, and James J. Filliben (Proc. Paper 16223).

7
0
7
7
6
1
0
3
1

